Master's thesis

NTNU
Norwegian University of Science and Technology
Faculty of Information Technology and Electrical Engineering
Department of Marine Technology

Vilde Hugdal Mathisen

Modelling of Ringing Loads on Offshore Wind Turbine Monopiles

Master's thesis in Marine Technology
Supervisor: Trygve Kristiansen
June 2020

NTNU
Kunnskap for en bedre verden

Vilde Hugdal Mathisen

Modelling of Ringing Loads on Offshore Wind Turbine Monopiles

Master's thesis in Marine Technology
Supervisor: Trygve Kristiansen
June 2020

Norwegian University of Science and Technology
Faculty of Information Technology and Electrical Engineering
Department of Marine Technology

NTNU
Norwegian University of
Science and Technology

Summary

Ringing is a phenomenon that can cause a threat to the structural integrity of offshore wind turbine monopiles. It is characterized by sudden transient oscillation at a wave frequency significantly lower than the eigenfrequency of the structure, induced by higher harmonic wave loads. Bottom fixed offshore wind turbine monopiles are located at finite water depth, and are more likely to experience ringing as waves in finite water are significantly nonlinear compared to waves in deep water. With a natural period of 3-5 seconds, the natural frequency can coincide with 2ω, 3ω and 4ω components of incoming waves. The FNV theory by Faltinsen, Newman and Vinje (1995) was developed to model nonlinear wave loads, but Kristiansen and Faltinsen (2017) found that the third harmonic wave load on a bottom mounted circular cylinder is overpredicted by existing FNV theory for long and steep waves. In order to determine if three dimensional effects not accounted for in present analytical expressions can explain the discrepancies, a 3D CFD-FNV load model has been developed in this thesis.

The 3D CFD-FNV load model combines two dimensional CFD simulations by the use of strip theory and existing terms in FNV theory, with the addition of a slender body term accounting for three dimensional effects in the total horizontal wave loads on the monopile. Two dimensional CFD simulations used in the load model were performed using OpenFOAM, and convergence studies of the numerical model indicated that the model was unable to accurately model flows with $KC > 6$. Comparison of the results from the 3D CFD-FNV load model showed that the three dimensional term did not significantly affect the total horizontal force amplitude. Investigation of the added term did however show that the third harmonic of the three dimensional force is out of phase with the third harmonic of the viscous force from two dimensional CFD simulations, indicating that three dimensional effects do in fact reduce the total horizontal force. The contribution to the third load harmonic from the three dimensional force was largest for steep and long waves, in the range where analytical expressions overpredict the third harmonic force. The amplitude of the three dimensional force is this range was 5-6% of the total horizontal force amplitude, which substantiates the idea that three dimensional effects are the reason for discrepancies between theoretical and experimental results for the third harmonic load on monopiles.

The results obtained in this thesis do however show that the added slender body terms in the 3D CFD-FNV load model do not alone account for the discrepancies in the third harmonic load predictions. Recommendations for further work include a study of other three dimensional effects, for instance vortex shedding in the yz-plane. Experiments show a local rear run-up that is believed to be caused by a high pressure zone from vortex shedding, and higher harmonic load contributions from this may explain the discrepancies in the predicted third harmonic load.

Preface

This thesis concludes my Master of Science in Marine Technology, with specialization in Marine Hydrodynamics. The thesis is written in the spring semester of 2020 at the Department of Marine Technology at the Norwegian University of Technology and Science in Trondheim.

I would like to thank my supervisor professor Trygve Kristiansen, whose great knowledge and enthusiasm for marine hydrodynamics have been an invaluable resource during this project. I would also like to express my gratitude to PhD candidate Prateek Gupta and postdoc. Mia Abrahamsen-Prsic for sharing their expertise in OpenFOAM and oscillating flows when I first started navigating my way through this field of study. My mom and brother deserve acknowledgements as well, for supporting me throughout long days at the home office. Finally, I would like to thank my friends at office A2.019. Even though we were not able to finish physically together due to the coronavirus situation, I thank you for all the laughs and (sometimes a bit too long) pauses during my final year at Tyholt.

Table of Contents

Nomenclature

α	Axial contraction factor
ϵ	Perturbation parameter
λ	Wave length
∇	Vector differential operator
ν	Kinematic viscosity
ω	Angular frequency
ϕ	Velocity potential
ϕ_ψ	Third order diffraction potential
ϕ_I	Incident wave potential
ϕ_S	Linear diffraction potential
ρ	Density of water
θ	Phase angle
ζ	Free surfave elevation
ζ_1	First order free surface elevation

ζ_a	Wave amplitude
C_D	Drag coefficient
C_M	Inertia coefficient
c_w	Wave celerity
g	Gravity constant
g_r	Uniform grading expansion of grid cells in radial direction
H_1	Linear wave height
k	Wave number
KC_1	Maximum linear KC number
KC_5	Maximum fifth order KC number
N_c	Number of rid cells surrounding cylinder surface
N_r	Number of rid cells in radial direction
p^{CFD}	2D CFD pressure component
p^w	3D pressure component
r_d	Pressure at far field circular control surface
U	Velocity field
u_θ	Velocity component in angular direction
U_m	Flow amplitude
u_r	Velocity component in radial direction
A	Motion amplitude
a	Cylinder radius
CFL	Courant-Friedrich-Lewy number

D	Cylinder diameter
H	Wave height
h	Water depth
KC	Keuleagan-Carpenter number
L	Domain length
p	Pressure
Re	Reynolds number
T	Flow period
u	Velocity component in x-direction
Ur	Ursell number
v	Velocity component in y-direction
w	Velocity component in x-direction

Chapter 1

Introduction

This chapter presents the motivation for studying ringing loads on offshore wind turbine monopiles, and a background of the problem. A scope of the thesis and an overview of the report structure is provided.

1.1 Motivation

Humans have affected the Earth's climate system at an unsustainable rate through landscape transformations, use of natural resources and waste generation since the pre-industrial period in the 18th century (Hoekstra and Wiedmann, 2014). Intergovernmental Panel on Climate Change (IPCC) states that human made global warming is causing alterations in the current climate system. Among these changes are increased temperatures and more heatwaves on land and in the ocean, and there is evidence that the global climate change relative to the pre-industrial period has impacted both ecosystems and human systems (Hoegh-Guldberg et al., 2018). As a result of the climate change discussion, the Paris Agreement (UNFCCC, 2015) was signed at the United Nations Framework Convention on Climate Change (UNFCCC) in December 2015 in Paris. The Paris Agreement is a global agreement made in order to ensure that the nations of the world commit to confine climate change through national determined contributions. The agreement states that the *”[...] parties share a long-term vision on the importance of fully realizing technology development and transfer in order to improve resilience to climate change and to reduce greenhouse gas emissions”* (UNFCCC, 2015, p.14). It is recognized by the parties that there is need for a significant reduction of global emissions, and the objective of the agreement is to keep the global temperature rise in the 21st century below 2°C.

A part of the response is to find replacements for fossil fuel generation with low carbon energy production, such as solar and wind power. The International Renewables Agency (IRENA) states that wind and solar power will lead the way for a global transformation of the electricity sector. According to IRENA (2019b), over 90% of the carbon dioxide emissions reductions related to energy necessary to achieve the 2°C target can be reached through accelerated deployment of renewables, along with electrification and increased energy efficiency. IRENA (2019a) predicts that onshore and offshore wind power combined will generate more than 35% of the total electriy needs by 2050. Hence, scaling up wind energy investments is key in order to meet the targets set in the Paris Agreement.

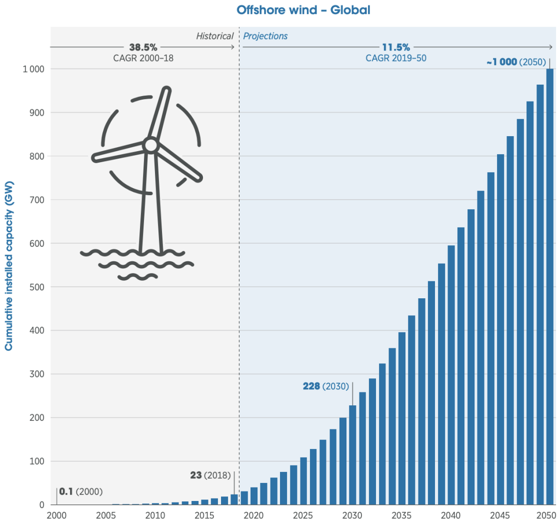

Figure 1.1: Offshore wind power deployment based on historical values from IRENA’s renewable capacity statistics (IRENA, 2019c) and future predictions based on IRENA’s analysis (IRENA, 2019a). *Figure retrieved from IRENA (2019a).*

The predicted offshore wind deployment over the next decades are presented in Figure 1.1, demonstrating that the total installed offshore wind capacity will increase significantly over the next decades. IRENA (2019b) predicts that the total installed offshore wind capacity in 2050 will be near 1 TW, which is 40 times the 2018 capacity at 23 GW.

The use of offshore wind enables countries to harness higher wind resources in densely populated coastal areas. The visual and environmental impact of the turbines are far less offshore as opposed to onshore wind farms, in addition to no size limit due to transport by rail or road. Offshore wind is considered to be one of the emerging renewables technology, gaining momentum through policy and financial incentives over the last two to three years (IRENA, 2019a). With the expansion of the offshore wind market, it is increasingly important to understand the marine environmental effects on the wind turbines.

Offshore wind farms are more expensive than their onshore counterparts, with 50% higher investment per MW (Morthorst and Kitzing, 2016). This is a result of larger structures and more complicated installations, along with higher cost for foundations, construction and grid connection. The costs related to the foundations and support structure can however be reduced with optimized design, along with cheaper production and faster installations offshore (Kallehave1 et al., 2015). Some typical foundations concepts for bottom fixed offshore wind turbines (OWTs) are shown in Figure 1.2.

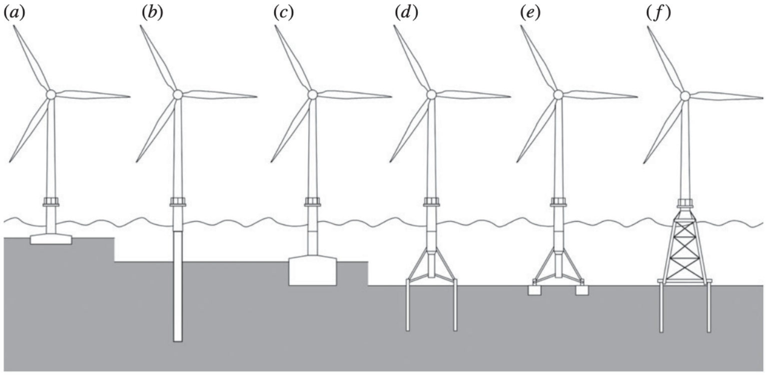

Figure 1.2: Typical foundation concepts for bottom fixed OWTs. (a) Gravity based foundation, (b) monopile foundation, (c) caisson foundation, (d) multipile foundation, (e) multi caisson foundation and (f) jacket foundation. *Figure retrieved from Kallehave1 et al. (2015).*

The monopile foundation (b) in Figure 1.2 is the most popular support structure as of present day, and represented 70% of all newly installed foundations in 2019 (WindEurope, 2019). A monopile foundation is a circular cylinder structure that is driven into the seabed, extending over the mean sea level.

1.2 Background

The average distance to shore for offshore wind farms in Europe in 2019 was 59 km at an average water depth at 33 m (WindEurope, 2019). Bottom fixed OWT monopiles are mounted in finite water depth, and designing offshore structures at finite water depth brings along challenges. Waves in finite water depth, especially in storm conditions, are significantly nonlinear compared to waves in deep water (Dean and Dalrymple, 1991). Nonlinear waves pose a threat to the structural integrity of the monopile as it can lead to a phenomena called $ringing$. Ringing is a sudden transient oscillation leading to large structural deflections of the structure, that are induced by excitation of the natural period from higher harmonic wave loads. Due to the increased nonlinearity of waves in finite water compared to waves in deep water, bottom fixed OWT monopiles at more likely to experience ringing than for for instance oil and gas platforms located in deeper water. Since the capacity of the installed OWTs have increased over the last years, the size of the OWTs monopiles have increased as well. Larger body dimensions lead to a higher eigenfreqeuncy, which has a higher likelyhood of coinciding with 3ω and 4ω components of incoming waves (Suja-Thauvin et al., 2014). This means that today's OWT monopiles are more exposed to ringing both due to their finite water depth location and increased structural size.

The structural costs of OWTs can be reduced by better design and reduction of excessive material. The ability to accurately predict higher order wave loads on OWT monopiles in an efficient manner can possibly reduce uncertainties regarding the structural integrity, and avoid building unnecessary oversized monopiles to reduce the risk of ringing in extreme sea states. A precise load model that can predict higher harmonic loads on monopiles can potentially make the design process of OWT monopiles more flexible, and reduce material costs of future offshore wind farms.

Faltinsen, Newman and Vinje (1995) provided an analytical expression for nonlinear wave loads on circular cylinders in deep water, using a perturbation approach of the wave number and the wave slope. The theory is denoted as FNV theory in this thesis. Kristiansen and Faltinsen (2017) generalized the theory to finite water depth, by replacing the infinite water limit and applying wave kinematics for finite water. Experimental results show that the first and second harmonic of the wave load are well described by the FNV theory, but the third load harmonics are only accurately described for small to medium steep waves (Kristiansen and Faltinsen, 2017). Up to a distinct limiting wave steepness, the theory overpredicts the third harmonic of the wave loads, with the discrepancy increasing for increasing wave steepness. The reason for the observed discrepancies have been attempted found, by for instance involving two dimensional viscous effects (Sæter, 2019). This did however not explain the discrepancies. During model tests by Kristiansen and Faltinsen (2017), a local rear run-up and upwelling of the free surface on the monopile has been observed. It is therefore of interest to study the three dimensional effects of the flow, and determine if the higher harmonic components of an added slender body term is able to disclose the gap between theory and experiments.

1.3 Scope

The scope of this thesis is to examine three dimensional effects of higher harmonic wave loads on OWT monopiles in severe wave conditions. The main focus will be on the addition of a slender body term in FNV theory, and the development of a combined 3D CFD-FNV model that includes a three dimensional term. Two dimensional CFD simulations in OpenFOAM are to be used for simulation of viscous forces on the cylinder by the use of strip theory, along with existing FNV theory. The third harmonic of the horizontal force will be examined closer, in order to determine if three dimensional effects can explain the discrepancies between present experimental results and theoretical predictions.

1.4 Report structure

This thesis will first present a theoretical background of the topic. An overview of regular wave theory including both linear and Stokes waves is given in chapter 2, along with methods for computing forces on vertical cylindrical structures. The focus will be on Stokes perurbation theory up to fifth order and FNV theory for nonlinear wave loads. Following in chapter 3 is an introduction to CFD and relevant software, and a description of the numerical model used for two dimensional flow simulations. The chapter includes convergence studies of the model along with a discussion of the observed flow regimes from the tests. Chapter 4 describes the concept of the combined 3D CFD-FNV load model along with the input parameters used to obtain relevant results. Next, chapter 5 presents the results from this project, by comparing numerical results with present experimental and theoretical data. The third harmonic load and the effects of the added three dimensional term is investigated, along with recommendations for further work. Concluding remarks are given in chapter 6.

Chapter 2

Theory

This chapter provides a theoretical background of the thesis topic. First, basic assumptions of fluid flow and the boundary value problem is introduced as a basis for completeness in the derivation of higher order wave theory. Linear and Stokes wave theory is presented, with focus on Stokes fifth order wave theory as it will be used to compute the input to the new 3D CFD-FNV load model. Methods for calculating wave forces on cylindrical structures are further given, including Morison's equation and FNV theory. The ringing phenomena and its complications on OWT monopiles are considered.

2.1 Regular wave theory

2.1.1 Potential flow

Sea loads can be investigated using potential theory, by considering sea water as a potential flow. A potential flow as denoted by Faltinsen (1990) is an *incompressible* and *inviscid* fluid with *irrotational* fluid motion. Incompressible is a fluid property used to describe a fluid with constant density throughout its motions, indicating that the volume of the fluid is constant. An inviscid fluid has zero viscosity, meaning there are no viscous forces caused by internal friction in the fluid. An irrotational flow has zero vorticity, implying that the particles in the flow are not rotating.

A potential scalar function ϕ exists for potential flows. ϕ describes the fluid velocity field as a gradient of itself. The velocity vector $\mathbf{U} = (u, v, w)$ at time t at point $\mathbf{x} = (x, y, z)$ can then be written as a function of ϕ,

$$\mathbf{U} = \nabla\phi \equiv \mathbf{i}\frac{\partial\phi}{\partial x} + \mathbf{j}\frac{\partial\phi}{\partial y} + \mathbf{k}\frac{\partial\phi}{\partial z} \tag{2.1}$$

$\mathbf{i}$, $\mathbf{j}$ and $\mathbf{k}$ are the unit vectors in x-, y- and z-direction respectively. The density of an incompressible fluid is constant, which means that the fluid has a material derivative of zero. This implies that the divergence of the fluid velocity is

$$\nabla \cdot \mathbf{U} = 0 \tag{2.2}$$

The vorticity vector $\boldsymbol{\omega}$ for an irrotational fluid is also zero,

$$\boldsymbol{\omega} = \nabla \times \mathbf{U} = 0 \tag{2.3}$$

It follows from Equation (2.2) and Equation (2.3) that the velocity potential ϕ satisfies the Laplace equation,

$$\nabla^2\phi = \frac{\partial^2\phi}{\partial x^2} + \frac{\partial^2\phi}{\partial y^2} + \frac{\partial^2\phi}{\partial z^2} = 0 \tag{2.4}$$

This way, the three unknown velocity components u, v and w are converted into only one unknown function ϕ. It is important to note that Equation (2.4) is only applicable in regions where it is reasonable to assume an irrotational flow. The velocity potential ϕ of the flow is found by solving the Laplace equation, and applying a set of relevant boundary conditions on the fluid. A solution to the Laplace equation for ϕ can then be used to determine all three components in the velocity field $\mathbf{U}$ everywhere in the flow using the relations in Equation (2.1). The solution is valid also for unsteady flows, since time is not a variable in the incompressible continuity equation. As a result, an unsteady flow field will at any time step adjust to satisfy the Laplace equation for the current boundary conditions at that time step.

2.1.2 The boundary value problem

The boundary value problem is a set of differential equations constrained by boundary conditions. This is applied to problems in hydrodynamics by assigning boundary conditions to fluid domains, usually involving a marine structure. The boundary value problem for a fixed body in a moving fluid is illustrated in Figure 2.1. The problem in the figure demonstrates a fluid domain with boundaries consisting of a fixed, marine structure as a solid body, the free surface, the seabed, an inlet and an outlet. This problem is considered in the following of Section 2.1.2.

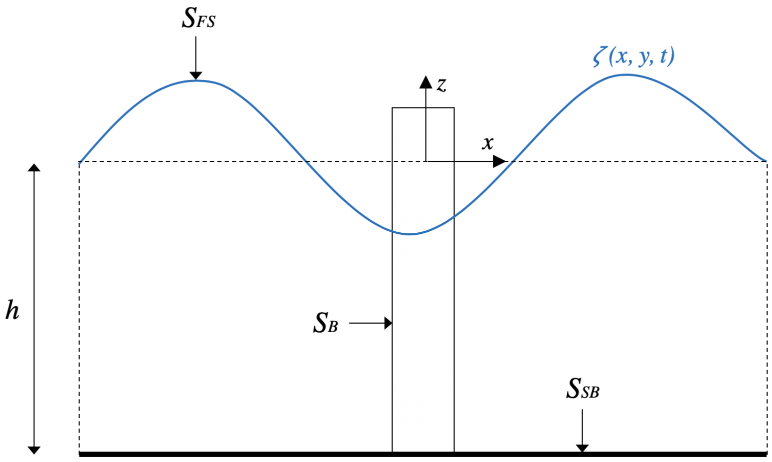

Figure 2.1: Illustration of the boundary value problem for a fixed body in a moving fluid. S_{SB} is the seabed, S_B is the solid body and S_{FS} if the free surface.

The Laplace equation in Equation (2.4) is the governing equation for the fluid domain in Figure 2.1. In order to obtain a unique solution to the Laplace equation for the problem, boundary conditions for the velocity potential ϕ are assigned to the boundaries of the domain. The two types of boundary conditions imposed on the fluid are known as the kinematic and dynamic free surface conditions.

S_{BS} is the seabed surface in the fluid domain. The seabed is assumed to be impermeable, with no flow across or along the surface. This means that the flow can not enter or leave the seabed, and has zero horizontal and vertical velocity at this surface. This is also denoted as the no slip condition. Since the differentiation along the normal to the seabed is positive in z-direction, the kinematic boundary condition at the bottom is formulated as

$$\frac{\partial \phi}{\partial z} = 0 \qquad \text{on } z = -h \tag{2.5}$$

The impermeability condition also applies to the fixed body in the fluid. The surface of the body is denoted as S_B, and the kinematic boundary conditions on the body is

$$\frac{\partial \phi}{\partial n} = \mathbf{U} \cdot \mathbf{n} = 0 \qquad \text{on } S_B \tag{2.6}$$

where **U** is the velocity of the body and **n** the normal vector of the body pointing out into the surrounding fluid. Since the body considered in this problem is fixed, **U** is zero.

At the free surface S_{FS} of the fluid domain, both the free surface elevation ζ and the velocity potential ϕ are unknown. This means that both the kinematic and dynamic boundary conditions need to be applied to the free surface. The kinematic boundary condition requires that all fluid particles located on the free surface remain on the free surface. Given that the location of a fluid particle is at position z and the free surface is defined as $\zeta(x, y, t)$,

$$z - \zeta(x, y, t) = 0 \tag{2.7}$$

The substantial derivative of Equation (2.7) gives the following expression for kinematic boundary condition on the free surface,

$$\frac{\partial}{\partial t}(z - \zeta(x, y, t)) + \nabla \phi \cdot \nabla (z - \zeta(x, y, t)) = 0 \tag{2.8}$$

$$\frac{\partial \zeta}{\partial t} + \frac{\partial \phi}{\partial x}\frac{\partial \zeta}{\partial x} + \frac{\partial \phi}{\partial y}\frac{\partial \zeta}{\partial y} - \frac{\partial \phi}{\partial z} = 0 \qquad \text{on} \quad z = \zeta(x, y, t) \tag{2.9}$$

The dynamic boundary condition on the free surface states that the atmospheric pressure is equal to the fluid pressure. This means that there is no pressure change across the free surface. The condition is formulated from Bernoulli's equation with uniform pressure,

$$g\zeta + \frac{\partial \phi}{\partial t} + \frac{1}{2}\left[\left(\frac{\partial \phi}{\partial x}\right)^2 + \left(\frac{\partial \phi}{\partial y}\right)^2 + \left(\frac{\partial \phi}{\partial z}\right)^2\right] = 0 \qquad \text{on} \quad z = \zeta(x, y, t) \tag{2.10}$$

The inlet and outlet boundary conditions are dependent on the specification of the fluid problem. In addition, the far field condition implies that waves generated by interaction between the fluid and the body die out far away from the body. By imposing these boundary conditions on the fluid domain, the boundary value problem can be solved.

2.1.3 Linear wave theory

Linear wave theory is based on the assumptions of a horizontal seabed and an infinite free surface in horizontal direction. The theory is also known as Airy theory and applies to propagating waves. Linear theory involves a linearization of the nonlinear free surface boundary conditions, which in many cases still provides sufficient information. By linearizing the problem the velocity potential ϕ becomes proportional to the wave amplitude ζ_a, which is valid by assuming that ζ_a is small relative to the characteristic wave length and body dimensions. The terms are linearized by the use of a Taylor expansion of the boundary conditions in Equation (2.9) and Equation (2.10) from the free surface $z = \zeta(x, y, z)$ to the mean free surface at $z = 0$, and keeping the linear terms in the expression for the wave amplitude. This gives the following kinematic and dynamic boundary conditions respectively:

$$\frac{\partial \zeta}{\partial t} = \frac{\partial \phi}{\partial z} \qquad \text{on} \quad z = 0 \tag{2.11}$$

$$g\zeta + \frac{\partial \phi}{\partial t} = 0 \qquad \text{on} \quad z = 0 \tag{2.12}$$

The velocity potential ϕ is obtained from solving the boundary value problem. With ϕ known, the free surface elevation ζ can be found by combining Equation (2.11) and Equation (2.12).

$$\frac{\partial^2 \phi}{\partial t^2} + g\frac{\partial \phi}{\partial z} = 0 \qquad \text{on} \quad z = 0 \tag{2.13}$$

Linearization of the nonlinear free surface boundary conditions is a great simplification of the problem. Linear wave theory can however be insufficient when it comes to describing the wave induced motion and loads on large volume structures. For structures such as bottom fixed vertical cylinders, nonlinear wave theory is needed in order to accurately describe the wave-structure interaction.

2.1.4 Stokes wave theory

An accurate theoretical description of wave characteristic is essential in our understanding of wave forces on marine structures. Linear wave theory is limited to waves of very small amplitudes, and is inaccurate for waves with finite amplitudes (Skjelbreia and Hendrickson, 1960). A wave theory for finite amplitude waves of an inviscid and irrotational flow was first derived by Stokes (1847). The waves incorporated in the theory are nonlinear and periodic two dimensional surface waves propagating without change of form, and are referred to as Stokes waves. These are modelled using an expansion approach with the use of trigonometric series, by assuming that the boundary value problem in Section 2.1.2 can be described by a perturbation series. The solution is expressed as a power series of a small perturbation parameter ϵ, that is of the same order at the nondimensional wave steepness $k\zeta_1$. ζ_1 is the free surface elevation to the first order and k is the wave number. The wave number k is the number of radians per wave length, defined as

$$k = \frac{2\pi}{\lambda} \tag{2.14}$$

ϵ quantifies the margin of error of the solution, which is the discrepancy between the approximated and exact solution to the problem. ϵ is assumed to be very small, i.e. $\epsilon << 1$. The accuracy of the solution obtained by the perturbation approach is thus dependent on the number of terms in each series. The expressions for the velocity potential ϕ and free surface elevation ζ are given as power expansions with increasing order of ϵ.

$$\phi = \widetilde{\phi_1}\varepsilon + \widetilde{\phi_2}\varepsilon^2 + \widetilde{\phi_3}\varepsilon^3 + ... \tag{2.15}$$

$$\zeta = \widetilde{\zeta_1}\varepsilon + \widetilde{\zeta_2}\varepsilon^2 + \widetilde{\zeta_3}\varepsilon^3 + ... \tag{2.16}$$

$\widetilde{\phi_n}$ and $\widetilde{\zeta_n}$ denote the terms proportional to ε^n. A collection of terms proportional to ε^n will thus yield a nth order solution of the boundary value problem. A linear solution is obtained by collecting the terms independent of ε, while collecting terms up to $n = 3$ gives a solution of third order and so on.

The accuracy of the solutions for ϕ and ζ increases as the order increases. The expressions do however become increasingly more computationally demanding for higher order waves, as the coefficients in Equation (2.15) and Equation (2.16) become progressively more complicated as more terms are added to the series. It should be noted that Stokes perturbation approach remains an approximation, and there is yet no closed form evidence that the series converge to exact solution. Still, comparisons of theoretical predictions and measured quantities shows that by Stokes higher order wave theory is in close agreement with experimental results (Patel, 1989).

2.1.5 Stokes fifth order wave theory

By expanding the Stokes perturbation series up to five terms, the solution will extend to waves of higher steepness than the ones covered by linear wave theory. Coefficients in series up to fifth order are however complex and require tedious calculations. In order to provide a solution for fifth order Stokes waves that was accessible to industrial engineers, Skjelbreia and Hendrickson (1960) provided a method of computing the value of the coefficients as a function of the water depth to wave length ratio h/λ.

The following of this section is an overview of the considerations made in the derivations by Skjelbreia and Hendrickson (1960). It should be noted that this section contains two deviations from the original paper, in order to maintain consistency in this thesis. The first is that the coordinate system is defined on the mean free surface according to Figure 2.1, instead of on the seabed. The second is the use of the constant γ instead of λ in the derivations, as this thesis discusses λ as the wave length. In order to avoid confusion, γ is used as a replacement as done by Patel (1989).

Skjelbreia and Hendrickson (1960) considered oscillatory, non-viscous waves at constant depth that extend in infinite direction perpendicular to the direction of propagation. Given that the Laplace equation and relevant boundary conditions are satisfied, the relations in Equation (2.1) can be used to determine the velocity components u and v from the velocity potential ϕ. The phase angle θ for oscillatory waves is given by

$$\theta = \frac{2\pi}{\lambda}(x - c_w t) = k(x - c_w t) \tag{2.17}$$

where c_w is the wave celerity. By applying this definition combined with the relation between the velocity potential and velocity components in Equation (2.1), the kinematic and dynamic free surface conditions can be expressed respectively as

$$\frac{\partial w}{\partial x} = \frac{-w}{c_w - u} \tag{2.18}$$

$$(c_w - u)^2 + w^2 = c_w^2 - 2g(K + \zeta) \tag{2.19}$$

where K in Equation (2.19) is a constant. The problem can then be solved for fifth order Stokes waves by finding a solution to Laplace equation that also satisfies the boundary condition on the seabed in Equation (2.5) along with Equation (2.18) and Equation (2.19).

Skjelbreia and Hendrickson (1960) provided a series form for the velocity potential ϕ that meet these specifications. The expression for ϕ is given here in the same compressed matter as Fimland (2018),

$$\phi = \frac{c_w}{k} \sum_{n=1}^{5} D_n \cosh(nk(h + z)) \sin(n\theta) \tag{2.20}$$

The surface profile ζ that satisfies the symmetry requirements is assumed to be

$$\zeta = \frac{1}{k}\sum_{n=1}^{5} E_n \cosh(n\theta) \tag{2.21}$$

Fimland (2018) introduced the coefficients E_n and D_n for simplification of the expressions for ϕ and ζ from the original paper.

Table 2.1: Definition for coefficients D_n of E_n.

n	D_n	E_n
1	$\gamma A_{11} + \gamma^3 A_{13} + \gamma^5 A_{15}$	γ
2	$\gamma^2 A_{22} + \gamma^4 A_{24}$	$\gamma^2 B_{22} + \gamma^4 B_{24}$
3	$\gamma^3 A_{33} + \gamma^5 A_{35}$	$\gamma^3 B_{33} + \gamma^5 B_{35}$
4	$\gamma^4 A_{44}$	$\gamma^4 B_{44}$
5	$\gamma^5 A_{55}$	$\gamma^5 B_{55}$

The coefficients A_{ij} and B_{ij} in Table 2.1 make up the algebraic complexity of the expressions for ϕ and ζ. These coefficients along with C_{ij} are given in the original paper by Skjelbreia and Hendrickson (1960). It should be noted that the original expression for C_2 includes a term with $+2592$, but Fenton (1985) found that this should be replaced by -2592.

The wave celerity c_w describes the propagation velocity of the wave crest or trough, and is expressed as

$$c_w = \frac{\sqrt{C_0^2(1 + \gamma^2 C_1 + \gamma^4 C_2)}}{k} \tag{2.22}$$

and the constant K used in Equation (2.19) is given by

$$K = \frac{\gamma^2 C_3 + \gamma^4 C_4}{k} \tag{2.23}$$

Skjelbreia and Hendrickson (1960) assume the wave height H, water depth h and wave period T to be known values. The unknowns to be found in the problem are the wave length λ and the coefficient γ in the expression for A_{ij} and B_{ij}. The problem is solved by rearranging Equation (2.21), which combined with Equation (2.22) form a set of two nonlinear equations with unknowns λ and γ:

$$\frac{\pi H}{h} = \frac{\lambda}{h}(\gamma + \gamma^3 B_{33} + \gamma^5 (B_{35} + B_{55}) \tag{2.24}$$

$$\frac{h}{\lambda_0} = \frac{h}{\lambda}(1 + \gamma^2 C_1 + \gamma^4 C_2) \tag{2.25}$$

λ_0 in Equation (2.25) is given by

$$\lambda_0 = \frac{gT^2}{2\pi} \tag{2.26}$$

By solving Equation (2.24) and Equation (2.25) for λ and γ, the velocity potential ϕ can be found. The relation in Equation (2.1) can then be used to determine the particle velocities in the horizontal and vertical direction,

$$u = c_w \sum_{n=1}^{5} nD_n \cosh(nk(h+z))\cos(n\theta) \tag{2.27}$$

$$w = c_w \sum_{n=1}^{5} nD_n \sinh(nk(h+z))\cos(n\theta) \tag{2.28}$$

The time derivatives of Equation (2.27) and Equation (2.28) yield the particle acceleration in horizontal direction. The horizontal and vertical velocity gradient of u are also determined. These are the wave kinematics used to compute wave forces on cylindrical structures in FNV theory.

$$a_1 = \frac{\partial u}{\partial t} = c_w \omega \sum_{n=1}^{5} n^2 D_n \sinh(nk(h+z))\cos(n\theta) \tag{2.29}$$

$$\frac{\partial u}{\partial x} = -c_w k \sum_{n=1}^{5} n^2 D_n \sinh(nk(h+z))\cos(n\theta) \tag{2.30}$$

$$\frac{\partial u}{\partial z} = c_w k \sum_{n=1}^{5} n^2 D_n \sinh(nk(h+z))\cos(n\theta) \tag{2.31}$$

A comparison of fifth order Stokes wave and a linear sine wave is illustrated in Figure 2.2.

It can be seen that fifth order Stokes waves inherit sharper and taller crests, and flatter and lower troughs. The water particle orbits have a steady down wave drift components, instead of circular or elliptical orbits.

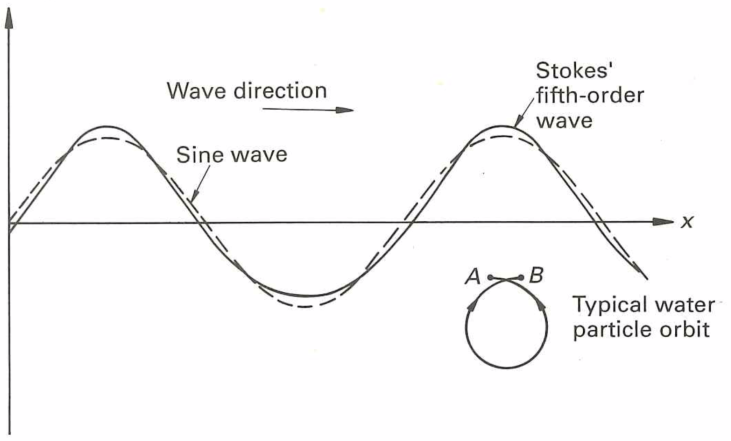

Figure 2.2: Properties of gravity waves, where A and B are start and end of the cycle for a water particle orbit. *Figure retrieved from Patel (1989).*

The procedure presented in the section has been widely implemented in the offshore industry. By taking only three input parameters H, T and h, the method gives an output for velocities, accelerations and pressures at given coordinates.

2.1.6 Limitations of Stokes wave theory

Stokes fifth order wave theory is considered unreliable for $\frac{h}{\lambda} < \frac{1}{8}$ (Patel, 1989). At these wave conditions the contribution from the fifth and higher order terms in the perturbation series are considered substantial, and reduce the numerical convergence of the solution.

Hedges (1995) proposed regions of validity of analytical wave theories, including Stokes wave theory. The approximate limits for analytical wave theories were allocated according to the Ursell number Ur. Ur was defined by Ursell (1953) and describes the nonlinar behaviour of long waves as the ratio between the wave height H and wave length λ to the water depth h.

$$U_r = \frac{H\lambda^2}{h^3} \tag{2.32}$$

The limitations for Stokes was theory as proposed by Hedges (1995) is illustrated in Figure 2.3 below.

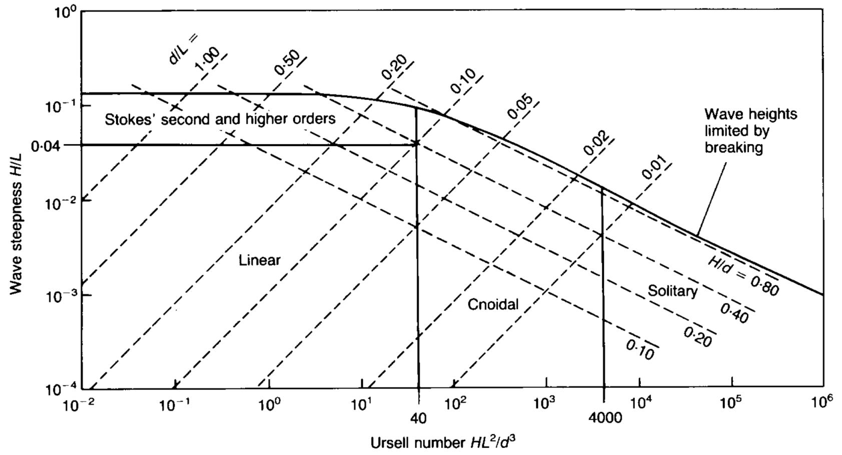

Figure 2.3: Approximate regions of validity of analytical wave theories as a function of Ur. *Figure retrieved from Hedges (1995).*

Figure 2.3 shows that the upper limit for Stokes's second and higher order wave theory is at $Ur = 40$, indicating that the application of Stokes fifth order wave theory should be limited to wave conditions with $H\lambda/h^3 > 40$.

2.2 Wave forces on vertical cylindrical structures

2.2.1 Morison's equation

Morison's equation (Morison et al., 1950) is widely used in ocean engineering to analyse hydrodynamics loads on a vertical cylindrical structures. The equation gives the the sectional horizontal force on a strip of a cylinder from unbroken surface waves, and is the sum of two force components:

1. Drag force proportional to the square of the velocity.
2. Inertia force proportional to the horizontal accelerative force exerted by the water mass displaced by the cylinder.

Morison's equation for the horizontal force a strip section dz of a cylinder is given by

$$dF_x = dF_I + dF_D = \Big(\frac{\rho\pi}{4} D^2 C_M a_1 + \frac{1}{2}\rho D C_D u|u|\Big) dz \tag{2.33}$$

where the force is positive in the wave propagation direction. ρ denotes the water mass density and D the cylinder diameter. u and a_1 are the horizontal velocity and acceleration of the water particles in the middle of strip dz. C_D and C_M are non-dimensional coefficients of drag and inertia respectively, that are empirically determined. Sarpkaya (1976) found that C_D and C_M both depend on the Keuleagen-Carpenter number KC and the Reynolds number Re. KC and Re are defined accordingly to Equation (2.34) and Equation (2.35).

$$KC = \frac{U_m T}{D} \tag{2.34}$$

$$Re = \frac{U_m D}{\nu} \tag{2.35}$$

U_m is the amplitude of the incoming flow, T is the flow period and ν is the kinematic viscosity of the fluid flow. The KC number number is used to describe the circular motion of the flow particles relative to the body dimensions, in this case the cylinder diameter D. The Reynolds number Re is the ratio of inertial to viscous forces on the body, and is used to classify flows as laminar or turbulent.

Sarpkaya (1976) performed experiments of vertical cylinders in harmonic oscillating flow with zero mean velocity, and found that C_D and C_M for smooth cylinders are functions of KC and Re, especially for $Re > 20000$. His findings also indicate that the relationship between the coefficients are not unique, and depends on the specific KC value as seen in Figure 2.4.

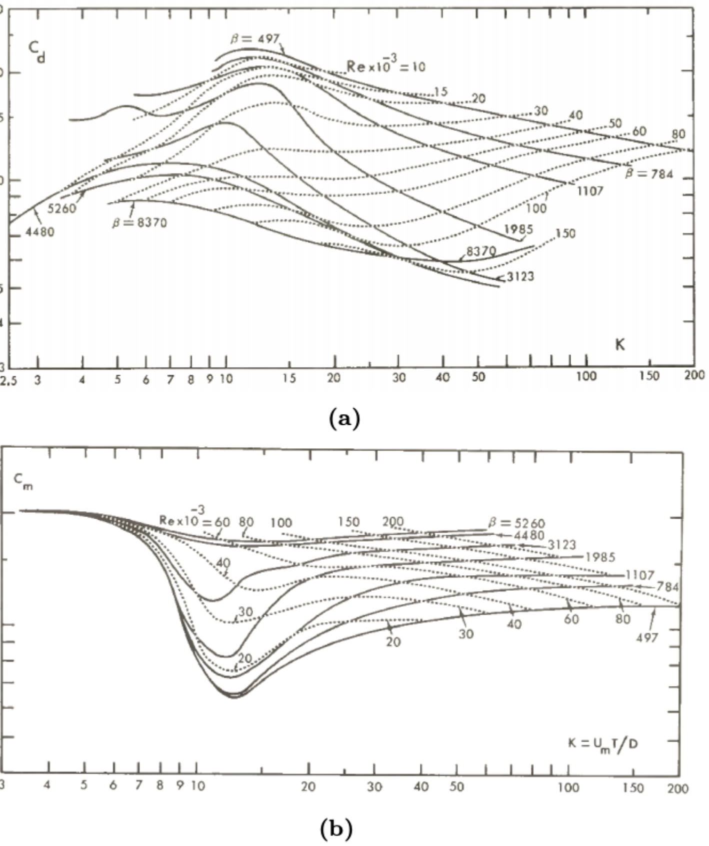

Figure 2.4: Drag coefficient C_D (a) and inertia coefficient C_M (b) coefficients dependence on Re and KC for a smooth circular cylinder from experimental results by Sarpkaya (1976). *Figure retrieved from Sarpkaya (1976).*

Morison's equation requires relatively low computational costs and its simplicity has made it widely used among engineers to determine horizontal force on cylinders in oscillatory flows.

2.2.2 Ringing

The ringing phenomenon was first acknowledged during the design phase of the first ever Tension Leg Platform (TLP). When performing model tests of the Hutton TLP located at the UK continental shelf, sudden bursts of resonance were observed during rough sea states with only a few occurring events (Natvig and Teigen, 1993). The phenomenon was characterized as a nonlinear motion with rapid build-up and a slow decay. The ringing impact attracted attention after the Hutton TLP project, as it could not be described by existing theory.

The causes of ringing are not yet clearly known. It is defined as large structural oscillation of the structure at natural frequencies significantly higher than the present wave frequencies, and occurs in extreme sea states with steep waves. Figure 2.5 shows a ringing event on a four column TLP, whereas the upper curve represents the incident wave and the lower curve the measured tension. Excitation of resonant response is evident at approximately 30 seconds as the incident wave suddenly build up to a high amplitude relative to the current sea state.

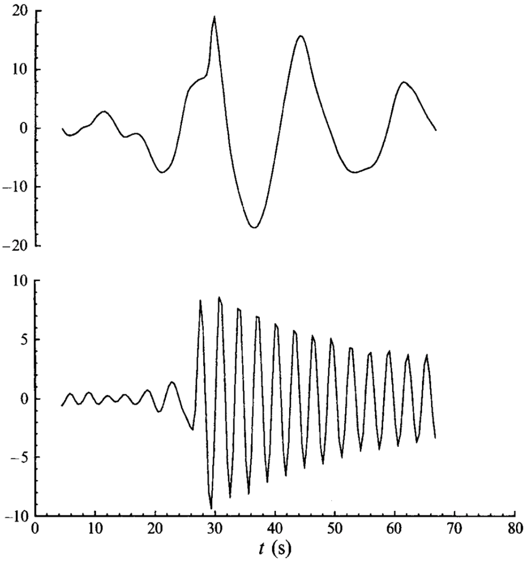

Figure 2.5: Experimental data of ringing on a TLP with four columns. The upper plot shows the incoming wave, and the bottom plot is the measured tension at the structural eigenfrequency. Data from Jefferys and Rainey (1994). *Figure retrieved from Faltinsen et al. (1995).*

Resonance is a threat to the structural integrity of offshore structures, and can lead to significant fatigue damage. This is why it if important to understand and predict how nonlinear wave loads can lead to ringing. The phenomenon is not explained by traditional diffraction theories, nor Morison's equation.

The lowest natural period for an OWT monopile is typically 3-5 seconds (Grue et al., 1994). This means that the natural frequency of the monopile can coincide with 2ω, 3ω and 4ω components of incoming waves. Nonlinear wave loads are higher in intermediate water depths than in deep water, which means that offshore structures such as bottom fixed OWT monopiles are more exposed to ringing than ones in deep water. Waves in finite water are additionally more nonlinear than waves in deep water (Dean and Dalrymple, 1991). This is root to the motivation for development of an efficient and accurate prediction of ringing in finite water.

Natvig and Teigen (1993) note that there are strong indications that certain effects are of importance when modelling ringing loads. Wave forces need to account for column interaction and possible upwelling effects. Variable submergence of the column during wave passage will lead to variable added mass, and needs to be accounted for. Though viscous drag to the free surface is considered to be insignificant, it should not be neglected. Finally, ringing is believed to be caused mainly by waves with a steep front or steep back. Such waves are generated in model tests in basins, but it is not evident if open ocean waves are quite as steep as the generated waves.

2.2.3 FNV theory

As mentioned, ringing is not explained by traditional wave theory. Observations from experiments suggest that ringing events occur for sea states with steep waves and a wave height H of similar magnitude to the cross-sectional dimension of the structure. In order to describe these nonlinear wave loads on a cylindrical structure, Faltinsen, Newman and Vinje (1995) developed an extended diffraction wave theory for wave loads up to third order. The theory is denoted as FNV theory in this thesis.

The cylinder radius a is considered the most relevant scale in the diffraction analysis. For offshore platforms in extreme sea states the wave length λ is significantly larger than a, which legitimizes the long wavelength approximation. Though the incoming waves are of long wave length, the wave amplitude ζ_a is comparable to the body dimensions. Since ringing appeared to occur for structures with dimensions of same magnitude as the wave height magnitude, Faltinsen et al. (1995) found it necessary to reevaluate the perturbation analysis with the assumption that $\zeta_a/a = \mathcal{O}(1)$. The assumptions made in order to develop the FNV theory are:

- The linear incident wave slope $k\zeta_a$ and the nondimensional cylinder radius ka are of the same order, i.e. $k\zeta = \mathcal{O}(\varepsilon)$ and $ka = \mathcal{O}(\varepsilon)$.
- The long wavelength approximation is valid, which means that he wave amplitude ζ_a and cylinder radius a is small relative to wave length λ, i.e. $k\zeta_a \ll 1$ and $ka \ll 1$.

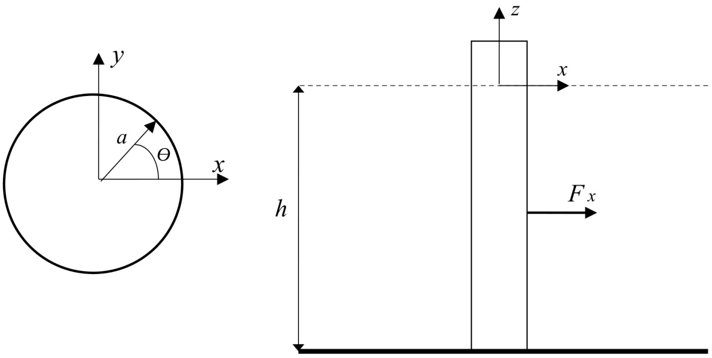

Figure 2.6: Cartesian and cylindrical coordinate system of cross-section of the cylinder in the xy-plane and the vertical cylinder in the zx-plane.

The method in the original paper is derived for infinite water depths and regular incident Stokes waves of third order. It is based on potential theory, and neglects flow separation. As a result of the long wavelength approximation, far field wave generation from the cylinder can be neglected. As the wave slope $k\zeta_a$ is very small, no wave breaking occurs. A coordinate system as shown in Figure 2.6 is considered, with $z = 0$ at the undisturbed free surface and the fluid domain at $z < 0$. The x-axis is positive in the direction of the incident wave propagation.

The total velocity potential ϕ is expressed as

$$\phi = \phi_I + \phi_S + \phi_\psi \tag{2.36}$$

where $\phi_D = \phi_I + \phi_S$ make up the diffraction potential that satisfies Laplace equation up to the incident free surface, including the incident wave potential ϕ_I and the linear diffraction potential ϕ_S. ϕ_ψ is the third order diffraction potential, satisfying the three dimensional Laplace equation and approximating the free surface conditions up to third order. The problem is further divided into a linear and nonlinar analysis.

The linear diffraction problem includes the linear diffraction potential $\phi_D = \phi_I + \phi_S$. When solving this problem, the domain is divided into two complementary sub-domains including the inner and outer domain. In the inner domain $r = \mathcal{O}(a)$ where a is of order 1, and h of order $1/\varepsilon$. In the outer domain $r = \mathcal{O}(\lambda)$. The velocity field is considered close to constant along the vertical cylinder axis in z-direction, and the vertical derivative is therefore of much small magnitude than the horizontal derivatives in x- and y-direction.

$$\frac{\partial \phi}{\partial z} \ll \frac{\partial \phi}{\partial x}, \frac{\partial \phi}{\partial y} \tag{2.37}$$

This means that $\frac{\partial \phi}{\partial z}$ can be considered negligible in the linear diffraction problem. Consequently, Laplace equation is reduced to two dimensions,

$$\frac{\partial^2 \phi}{\partial x^2} + \frac{\partial^2 \phi}{\partial y^2} = 0 \tag{2.38}$$

ϕ_D can then be expressed as a two dimensional potential $\phi_D = \phi_D(x, y)$, and only needs to satisfy Laplace equation in the horizontal plane. By Taylor expansion of ϕ_D around $x = 0, y = 0$ to first order in x-direction, the solution for the near field of the cylinder is expressed by

$$\phi_D = \phi_I + \frac{\partial \phi_I}{\partial x}\Big|_{x=0,y=0}(x+\phi_{11}) + \frac{\partial^2 \phi_I}{\partial x^2}\Big|_{x=0,y=0}(\frac{1}{2}x^2+\phi_{12}) + f(z,t) + \mathcal{O}(\varepsilon^4) \quad (2.39)$$

$$\phi_D = \phi_I + u(x=0,y=0)(x+\phi_{11}) + \frac{\partial u}{\partial x}\Big|_{x=0,y=0}(\frac{1}{2}x^2+\phi_{21}) + f(z,t) + \mathcal{O}(\varepsilon^4) \quad (2.40)$$

The terms in Equation (2.39) and Equation (2.40) are of order $\phi_{11} = \mathcal{O}(\varepsilon)$, $\phi_{11} = \mathcal{O}(\varepsilon^2)$ and $f(z,t) = \mathcal{O}(\varepsilon^3)$. $f(z,t)$ is the hydrodynamic interaction potential and is the slender body term in the expression for ϕ_D. $f(z,t)$ does not contribute to the horizontal force of order lower than $\mathcal{O}(\varepsilon^6)$, as shown by Faltinsen (1999). ϕ_{11} and ϕ_{12} only need to satisfy the two dimensioanl Laplace equation in Equation (2.38), and can be determined using the impermeability boundary condition on the cylinder.

$$\frac{\partial(x+\phi_{11})}{\partial r}\Big|_{r=a} = \frac{\partial(\frac{1}{2}x^2+\phi_{12})}{\partial r}\Big|_{r=a} = 0 \quad (2.41)$$

The force on the cylinder due to ϕ_D is found by integration of the pressure along the cylinder surface,

$$F'(z,t) = -\int_0^{2\pi} p\, n_1\, d\theta = -\int_0^{2\pi} p\, cos\theta\, d\theta \quad (2.42)$$

where n_1 is the normal vector pointing into the flow, accounting for the surge component. The pressure p acting on the cylinder in Equation (2.42) is found from the Bernoulli equation as follows,

$$\frac{1}{\rho}p = -\frac{\partial \phi_D}{\partial t} - \frac{1}{2}\Big(\frac{\partial \phi_D}{\partial r}\Big)^2 - \frac{1}{2a^2}\Big(\frac{\partial \phi_D}{\partial \theta}\Big)^2 - \frac{1}{2}\Big(\frac{\partial \phi_D}{\partial z}\Big)^2 \quad (2.43)$$

Combined this gives an expression for the distributed force from ϕ_D:

$$F'(z,t) = \rho\pi a^2\Big(\frac{\partial u}{\partial t} + u\frac{\partial u}{\partial x} + w\frac{\partial u}{\partial z}\Big) + a_{11}\Big(\frac{\partial u}{\partial t} + w\frac{\partial u}{\partial z}\Big) \quad (2.44)$$

The nonlinear scattering potential ϕ_ψ was introduced by Faltinsen (1999), as the linear diffraction potential ϕ_S does not satisfy the inhomogenous boundary conditions. The third order scattering potential ϕ_ψ is therefore implemented in the nonlinear analysis of the problem in FNV theory, in order to satisfy the three dimensional Laplace equation in addition to the inhomogenous boundary condition. The free surface boundary condition is then

$$\frac{\partial^2 \phi_\psi}{\partial t^2} + g\frac{\partial \phi_\psi}{\partial z} = -2\nabla\phi \cdot \nabla\phi_t - \frac{1}{2}\nabla\phi \cdot \nabla(\nabla\phi)^2 \qquad on \quad z = \zeta \tag{2.45}$$

ϕ_ψ varies rapidly in vertical direction. This means that the vertical gradient of the potential $\partial\phi_\psi/\partial z$ is much larger than the second time derivative $\partial^2\phi_\psi/\partial t^2$. $\partial^2\phi_\psi/\partial t^2$ on the left side of Equation (2.45) is thus assumed to one order lower. Since ϕ_ψ varies vertically, the free surface condition is not imposed on the mean water level at $z = 0$, but at the linear incident free surface elevation $z = \zeta_{I1}$. One of the main assumptions in the development of the FNV theory is that the wave slope ka is very small, so the free surface condition in the inner region of the fluid problem can be limited to satisfy the horizontal plane $z = \zeta_{I1}$ located at $x = 0, y = 0$.

By solving the boundary value problem with the above prerequisites, an expression for the force acting on the cylinder from the third order diffraction potential ϕ_ψ is obtained. The force is denoted by F^ψ, and is considered at $x = 0, y = 0$.

$$F^\psi = \rho\pi a^2 \frac{4}{g} u^2 \frac{\partial u}{\partial t}\bigg|_{x=0,y=0} \tag{2.46}$$

The total horizontal force F_x on the cylinder is the sum of the force contributions from the linear diffraction potential ϕ_D and the third order diffraction potential ϕ_ψ. The force is computed by integrating the distributed force $F'(z,t)$ in Equation (2.42) from the seabed to the incident free surface, and adding F^ψ in Equation (2.46).

$$F_x = \int_{-\infty}^{\zeta} F'(z,t)dz + F^\psi \tag{2.47}$$

The integration in Equation (2.47) is divided into three separate intervals. Faltinsen (1999) defined one interval from infinite deep water to the mean water level ($-\infty \leq z \leq 0$), one from the mean free surface to the linear incident free surface ($0 \leq z \leq \zeta_{I1}$) and one from the linear incident free surface to the local wave elevation of third order ($\zeta_{I1} \leq z \leq \zeta$). The local wave elevation is $\zeta = \zeta_{I1} + \zeta_{I2}$, including both incident waves and local diffraction. By redefining F_x according to these three intervals, the total horizontal force is

$$F_x = \int_{-\infty}^{0} F'(z,t)dz + \int_{0}^{\zeta_1} F'(z,t)dz + \int_{\zeta_1}^{\zeta} F'(z,t)dz + F^{\psi} \tag{2.48}$$

2.2.4 Generalized FNV theory

The original FNV theory by Faltinsen et al. (1995) was derived for infinite deep water, and Kristiansen and Faltinsen (2017) generalized the theory to finite water depth. The theory was generalized by replacing the infinite water limit $z = -\infty$ with a finite water depth of $z = -h$ and applying wave kinematics for finite water depth. The expressions for the total horizontal force from Equation (2.48) at finite water is consequently

$$F_x = \int_{-h}^{\zeta_t} F'(z,t)dz + F^{\psi} \tag{2.49}$$

$$F_x = \int_{-h}^{0} F'(z,t)dz + \int_{0}^{\zeta_1} F'(z,t)dz + \int_{\zeta_1}^{\zeta} F'(z,t)dz + F^{\psi} \tag{2.50}$$

The application of the generalized FNV theory was evaluated by Kristiansen and Faltinsen (2017) through systematic experiments in the medium sized wave tank at the Marine Technology Centre at NTNU. The measured force from the experiments and the theoretical prediction from the generalized FNV theory were bandpass filtered into the five first load harmonics, and the main focus was to study the third harmonic of the horizontal wave loads. Comparison of the results showed good compliance for conditions of small wave steepness, but the theoretical third harmonic load was found to be overpredicted for severe wave conditions. Above the limit of a distinct wave steepness, the FNV theory overpredicts the third harmonic load. The discrepancies between experimental and theoretical results increases as the wave steepness increases, as seen in Figure 2.7 from the original paper by Kristiansen and Faltinsen (2017).

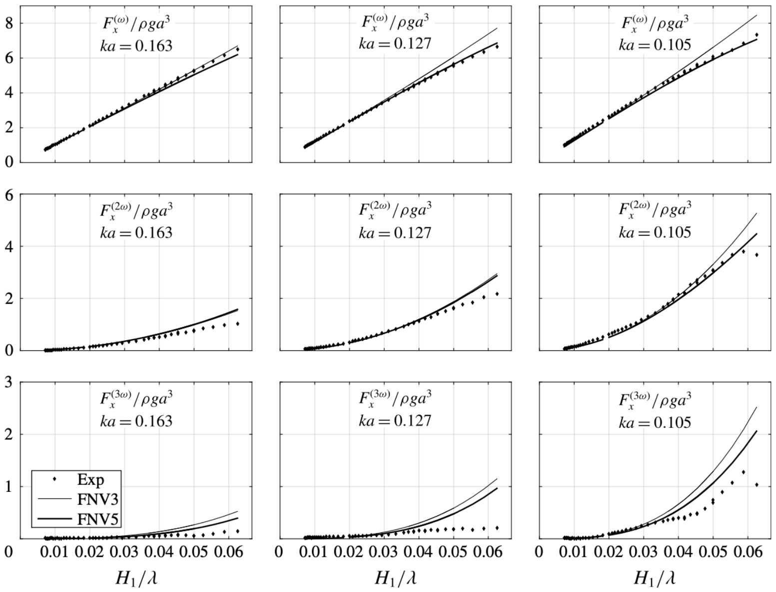

Figure 2.7: Amplitude of the first three harmonics of the horizontal force due to regular waves at water depth $h/a = 7.83$ versus wave steepness for nondimensional wave numbers $ka = 0.163$, $ka = 0.127$ and $ka = 0.105$. *Figure retrieved from Kristiansen and Faltinsen (2017).*

Kristiansen and Faltinsen (2017) stated that the local KC number along the cylinder axis indicates that flow separation occurs in the wave conditions where the discrepancies are present. The addition of a drag term and KC-dependent added mass coefficients did however not explain the discrepancies for the third harmonic load. During the experiments, a local rear run-up was observed. The run-up was found be to due to a locally high pressure at the rear of the cylinder, caused by vortex shedding from flow separation. This resulted in a local steep wave propagating in the opposite direction of the propagating waves, and the load associated with the run-up was believed to be be cause of the discrepancies in the third harmonic load. Sæter (2019) derived a combined CFD-FNV load model in order to replicate viscous effects in the flow that are not accounted for in inviscid FNV theory. The load estimations from the CFD-FNV load model did however not comply better with experimental results, and two dimensional viscous effects were not able to explain the observed discrepancies in the third harmonic loads.

Chapter 3

Numerical model

This chapter introduces the numerical model that is used for two dimensional CFD simulations of the flow in the 3D CFD-FNV load model. An introduction to CFD and OpenFOAM is first given. Next is a description of the grid structure of the numerical model, along with imposed boundary and initial conditions used to model the flow. Convergence studies of the numerical model are performed in order to assess the quality of the mesh. Finally, a study of the flow regimes around the monopile is presented.

3.1 Computational Fluid Dynamics

Computational Fluid Dynamics (CFD) is use of numerical analysis to solve fluid flow problems. CFD research is based on solving the key governing equations that describe the physics of fluid dynamic, namely the continuity equations, Navier Stokes equations and energy equations (Yen et al., 2017). The numerical approach in CFD is to approximate the solution to these equations by replacing complex Partial Differational Equations (PDEs) with algebraic equations that are easier solve. In order to attain a definite solution, the fluid flow domain needs to be constrained by boundary conditions providing the relations between the velocity, pressure, temperature and density in the flow.

CFD solvers are continually improving and are becoming more available through commercial CFD software. Computational power has increased rapidly in the last decades, allowing for more complex and detailed flow analysis with the use of CFD. The use of CFD to model wave loads on offshore structures has been practiced for some time, but there are few studies of simulation of higher order loads from nonlinear waves. Liu et al. (2001) performed CFD analysis of higher harmonic wave loads on a surface piercing cylinder, using a mixed Eulerian-Langrangian boundary element model. The numerical results agreed remarkably well with experimental data, and Liu et al. (2001) concluded that this provided evidence that ringing excitations are a direct result of nonlinear wave diffraction. Paulsen et al. (2014) investigated steep regular water waves on a vertical cylinder using a two-phase incompressible Navier Stokes solver, whereas numerical analysis of the secondary load cycle showed good agreement between the numerical approximations and FNV theory for the third harmonic force. Paulsen et al. (2014) also observed that the third harmonic forces agreed well by Morison's formulation at deep water, but is overestimated by Morison at intermediate depths.

CFD simulations in general require far less resources than physical experiments involving offshore marine structures. However, complex test conditions require high computational costs, leading to time consuming simulations. CFD simulations as design tool is not commonly used in the offshore industry as it it considered too impractical as of present day.

3.2 OpenFOAM

OpenFOAM (Open Field Operation and Manipulation) was used for two dimensional CFD simulations in the combined 3D CFD-FNV load model in this thesis. OpenFOAM is a free and open source CFD software created for the GNU/Linux operating system, initally released in 2004. The motivation behind developing OpenFOAM was to design a powerful and adaptable simulation toolbox, and C++ was used as a programming language due to its modular and object oriented features (Russel and Cohn, 2012). As an open source software the user has the rights to change and distribute the source code, and the OpenFOAM syntax makes it suited for customization of numerical solvers and post-processing utilities.

Russel and Cohn (2012) list advantages and disadvantages to OpenFOAM. Some of the advantages include friendly syntax for PDEs, the unstructured grid capabilities, the range of applications and models readily available, along with the continuous commercial support by developers and the zero license costs. The disadvantages are the lack of integrated graphical interface, and insufficient Programmer's guide and lack of updated documentation making it harder for new users.

OpenFOAM was used in this thesis due to its flexibility and wide range of flow modelling options, including both mesh generation of the numerical domain and simulation of oscillating flow for both regular and higher order Stokes waves.

3.3 Grid structure

Viscous effects in the new combined 3D CFD-FNV load model are accounted for by two dimensional CFD simulations. The numerical model of the flow around an OWT monopile is developed as a square, two dimensional flow domain around a cylinder, and the topology of the model is assembled as a grid structure.

The mesh generation utility *blockMesh* in OpenFOAM was used to develop the grid structure. The topology is created by discretizing the domain into three dimensional hexahedral blocks, where the geometry of the blocks is defined by the location of eight vertices in each corner of the block. This grid structure is classified as a structured grid. The advantages of a structured grid to an unstructured grid is that there are fewer cells generated that are easier to numerate with indices, leading to a simplified solving procedure (Çengel and Cimbala, 2006). Structured grids are unfit to model complex geometries, but for the present case with a circular cylinder a structured grid geometry was deemed sufficient.

The grid is generated from the directory file *blockMeshDict* in the OpenFOAM case folder. Changes to the grid can be performed directly into *blockMeshDict* and updated. In order to build an appropriate domain for the numerical model, all vertices for the blocks and curved edges need to be defined. This was done by creating a parametric model in MATLAB and writing the data to the *blockMeshDict* file in the correct syntax. The use of a parametric model in MATLAB made it possible to easily adjust geometrical parameters and grid refinement, which was essential to streamline further convergence studies.

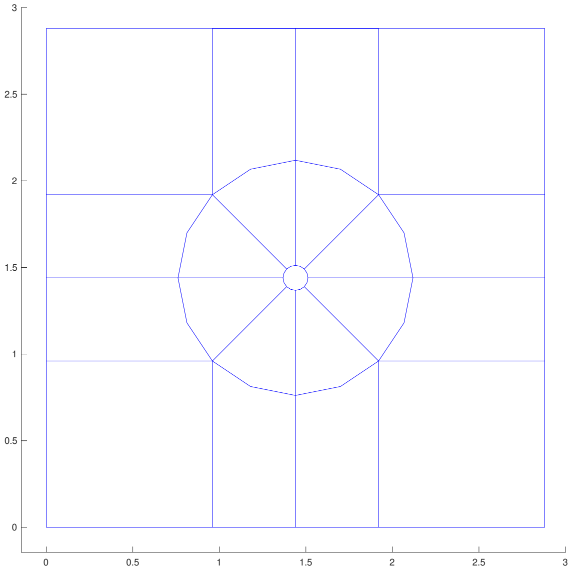

Figure 3.1: Discretization of two dimensional computational domain for a circular cylinder with diameter $D = 0.144$ and domain size $L \times L = 20D \times 20D$.

Figure 3.1 shows the discretization of the domain. OpenFOAM operates in three dimensions, so in order to simulate a two dimensional flow the domain is one cell thick in z-direction. This way, the flow cannot move in z-direction. The geometrical dimension in z-direction was set equal to the cylinder diameter D. The subdomain surrounding the cylinder was modelled in a circular manner in order to manage the grid resolution and grading in this area with regards to vortex shedding around the cylinder. Since the flow to be studied is oscillatory and shedding will occur both in front and back the cylinder, the cylinder was placed with equal distance to the inlet and the outlet. The outer area of the domain consists of blocks perpendicular to the boundaries, in order to avoid significantly skewed cells where the flow arrives and exits the domain. Figure 3.2 shows the meshed grid structure in the OpenFOAM visualization tool ParaView.

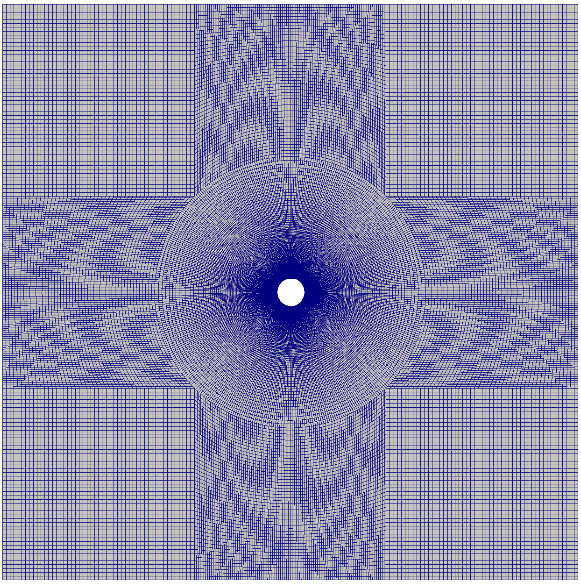

Figure 3.2: Mesh of two dimensional computational domain in ParaView with $D = 0.144$ and domain size $L \times L = 20D \times 20D$.

3.4 Boundary conditions

The boundaries for the domain are defined in the *blockMeshDict* file in the OpenFOAM case folder according to Figure 3.3. The inlet and outlet are set as *patch*, which in OpenFOAM is defined as a general boundary. Since the case is two dimensional, the front and back of the domain is set to *empty* to ensure that there is no flow in z-direction. Because the fluid problem is considered as an infinite fluid, top and bottom of the numerical model are imposed by the *symmetryPlane* condition which represents symmetry in the planar patches. The cylinder surface is set as *wall*, and treated as a fixed, no-slip wall.

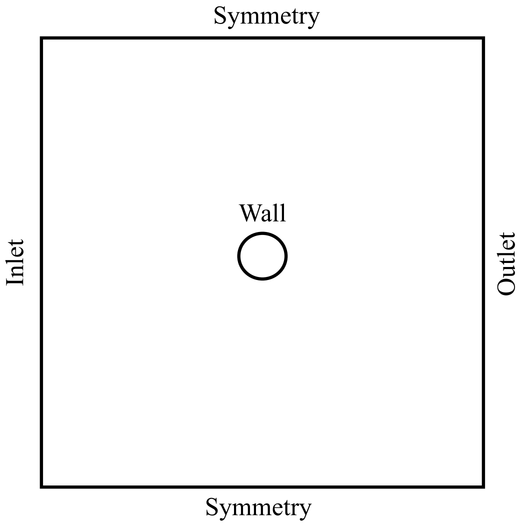

Figure 3.3: Two dimensional domain with specified boundary conditions.

3.5 Initial conditions

Initial conditions need to be set in order to initiate the flow. This is done by specifying the velocity and pressure in the U and p file respectively in the 0 folder in the OpenFOAM case folder. Table 3.1 summarizes the initial conditions given for the domain.

Boundary	U	p
Inlet	pressureNormalInletOutletVelocity	uniformFixedValue
Outlet	pressureNormalInletOutletVelocity	uniformFixedValue
Top	symmetryPlane	symmetryPlane
Bottom	symmetryPlane	symmetryPlane
cylinder	fixedValue	zeroGradient
Front and back	empty	empty

Table 3.1: Initial conditions on boundaries in the two dimensional domain domain in U and p file in 0 folder.

Since the flow is oscillatory, the same conditions apply for the inlet and the outlet. The boundary conditions on the inlet and outlet are imposed in order to simulate a pressure driven flow. The initial pressure condition at the inlet and outlet is set to $uniformFixedValue$, which applies a time dependent value on the surface through a $uniformValue$. The values were read using $tableFile$, whereas an inline list of time value pairs were imposed throughout the simulation cycle from a text file in the OpenFOAM case folder. The pressure at the inlet and outlet were provided from two separate text files $pin.txt$ and $pout.txt$, that were generated from an input MATLAB script. The pressure input values as a function of time were derived from the Navier-Stokes equation in x-direction, assuming a uniform flow,

$$\frac{\partial p}{\partial x} = -\rho \frac{\partial u}{\partial t} \tag{3.1}$$

By assuming anti-symmetry for at the inlet and outlet, the pressure at the boundaries can be found as a function of the horizontal acceleration and the length of the computational domain.

$$\int_{L/2}^{-L/2} \frac{\partial p}{\partial x} dx = -\rho \int_{L/2}^{-L/2} \frac{\partial u}{\partial t} dx = p(L/2) - p(-L/2) = -\rho L \frac{\partial u}{\partial t} \tag{3.2}$$

whereas anti-symmetry gives

$$p(L/2) = -p(-L/2) \tag{3.3}$$

which yields

$$p(L/2) = -\frac{1}{2} \rho L \frac{\partial u}{\partial t} \tag{3.4}$$

$$p(-L/2) = \frac{1}{2} \rho L \frac{\partial u}{\partial t} \tag{3.5}$$

$p(-L/2)$ denotes the initial pressure condition at the inlet and $p(L/2)$ the initial pressure condition at the outlet.

The velocity at the inlet and outlet were set to $pressureNormalInletOutletVelocity$ with a value of $uniform$ *(0 0 0)*. This is an initial condition applied to boundaries where the pressure is specified, which indicates a zero gradient condition for the outflow and a velocity obtained from the flux normal to the inlet for the inflow. By specifying a zero uniform value, the velocity at both the inlet and outlet are zero at $t = 0$.

The top and bottom of the domain are set to $symmetryPlane$ for velocity and pressure also here, enforcing a symmetry constraint. The velocity at the cylinder surface is prescribed fixed value $fixedValue$ of $uniform$ *(0 0 0)*, ensuring zero velocity in all directions. Pressure at the cylinder surface is $zeroGradient$. The velocity and pressure at the front and back are $empty$.

3.6 Transport properties

The transport properties of the flow are defined in the $constant$ folder in the OpenFOAM case folder. A Newtonian transport model is used, assuming a constant kinematic viscosity ν equal to $1e-06$. The turbulence properties are also defined in this folder, and the simulation type is set to laminar using no turbulence models.

3.7 Solver

The solver $pimpleFoam$ is used. $pimpleFoam$ is a transient solver used for incompressible, turbulent flows of Newtonian fluids. The solver applies the PIMPLE algorithm, which combines the Pressure Implicit with Splitting of Operators (PISO) and Semi-Implicit Method for Pressure Linked Equations (SIMPLE) algorithms.

The OpenFOAM simulations were performed using Ubuntu. The convergence studies were mainly performed remotely on the computer Euler at the Marine Technology Centre at NTNU through private user access in the terminal. The tests of the 3D CFD-FNV load model were performed on VirtualBox installed on a private computer connected to an external hard drive, due to the large size of the post processing data.

3.8 Convergence studies

Convergence studies of the mesh are performed in order to evaluate the quality of the numerical model. Convergence studies of the numerical model involved grid refinement in radial direction including varying number of grid cells and varying grading from the outer domain to the cylinder surface. Grid refinement along the cylinder surface was also evaluated. As the numerical model is to be used in tests with oscillating flow, the force coefficients C_D and C_M were used as parameters in the convergence studies. Considering Morison's equation for the horizontal force on a strip,

$$dF_x = \Big(\frac{\pi}{4}\rho D^2 C_M a_1 + \frac{1}{2}\rho D C_D u|u|\Big)dz \tag{3.6}$$

where he velocity u and acceleration a_1 are harmonically varying. This means that the force coefficients can be obtained by Fourier averaging (Mentzoni et al., 2018),

$$\int_0^{nT} F_x u dt = 0 + C_D \int_0^{nT} \frac{1}{2}\rho D u|u| u dt \tag{3.7}$$

$$\int_0^{nT} F_x a_1 dt = C_M \int_0^{nT} \rho \frac{\pi}{4} D^2 a_1 a_1 dt + 0 \tag{3.8}$$

The integration needs to be performed over an integer number n of period cycles. Further, we assume that the total horizontal force can be approximated by the horizontal viscous and pressure forces computed by OpenFOAM.

From Equation (3.7) and Equation (3.8), C_D and C_D are given by

$$C_D = \frac{\int_0^{nT} F_x a_1 dt}{\int_0^{nT} \frac{1}{2}\rho D u|u| u dt} \tag{3.9}$$

$$C_M = \frac{\int_0^{nT} F_x a_1 dt}{\int_0^{nT} \frac{\pi}{4}\rho D^2 a_1 a_1 dt} \tag{3.10}$$

The tests were run for KC numbers ranging from 2 to 16 for $Re = 70000$. To maintain constant Re for all KC numbers, the period was varied with the velocity amplitude. The tests were run over a total of 10 periods. The simulations were performed with an adjustable time step in order to increase the efficiency of the model. The adjustable time step settings were adjusted according to a maximum Courant-Friedrichs-Lewy (CFL) number (Courant et al., 1928) value of 0.5. The two dimensional CFL number is defined as

$$CFL = \frac{u\Delta t}{\Delta x} + \frac{v\Delta t}{\Delta y} \tag{3.11}$$

and is used as a criteria in explicit CFD schemes to ensure a stable numerical solution. Δt is the time step and Δx and Δy denote the grid size in horizontal and vertical direction respectively. By setting the CFL number to a maximum limit, one defines a limit for how far the flow can move within one time step. For $CFL < 1$, the flow cannot advance more than one grid cell per time step, and the numerical errors in the solutions are considered insignificant.

3.8.1 Grid refinement in radial direction

The effect of number of grid cells in radial direction N_r is shown in Figure 3.4. In order to evaluate N_r independently, the grading was set to 1. This means that the grid cells in the domain surrounding the cylinder are of equal length in radial direction. Number of grid cells along the cylinder surface are kept constant at $N_c = 400$. Four different cases with $N_r = 50$, $N_r = 100$, $N_r = 150$ and $N_r = 200$ are presented.

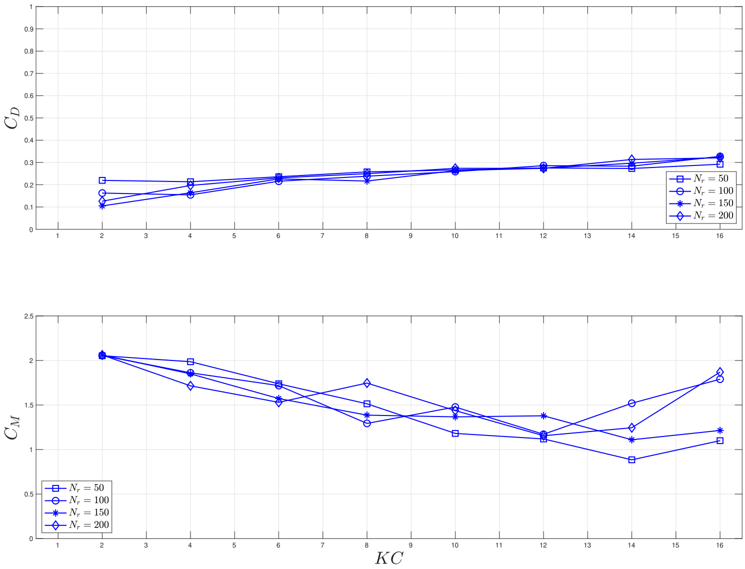

Figure 3.4: Drag coefficient C_D and added mass coefficient C_M for $N_r = 50$, $N_r = 100$, $N_r = 150$ and $N_r = 200$ with constant $N_c = 400$ and $g_r = 1$.

The plots in Figure 3.4 shows the dependence on N_r. The drag coefficient C_D increases linearly with the KC number. For low KC numbers at < 6, increased N_r gives lower C_D values, but there is no apparent trend correlating to N_r for higher KC numbers. C_M is approximately 2 at $KC = 2$ independent of N_r, and decays gradually to $KC = 10$. For $2 < KC < 8$ it appears that increased N_r results in a slightly lower C_M value. At $KC > 10$, C_M deviates clearly for all N_r values. There is no clear trend for increasing N_r, but it should be noted that the fluctuations appear to be bigger at finer mesh. At $N_r = 50$ for instance, the curve simply flattens out as KC increases. A possible explanation for this is the transition between the domain surrounding the cylinder and the outer domain. The transition between fine mesh from the domain around the cylinder to coarser mesh to the outer domain can cause discontinuations in the flow.

In order to assess the mesh quality, the the total number of grid cells along with maximum aspect ratio in the numerical model are plotted as a function of N_r in Figure 3.5.

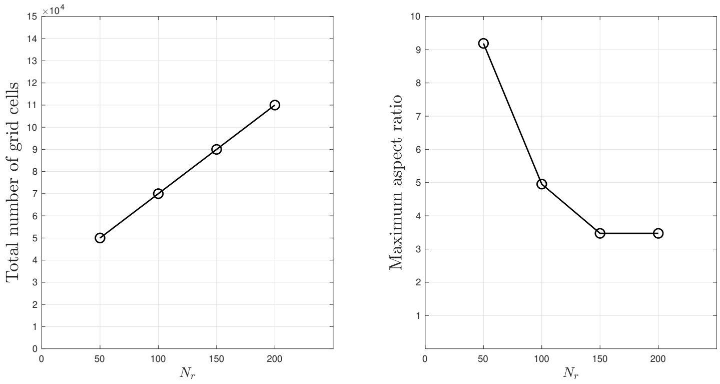

Figure 3.5: Total number of grid cells and maximum aspect ratio for mesh with $N_r = 50$, $N_r = 100$, $N_r = 150$ and $N_r = 200$ with constant $N_c = 400$ and $g_r = 1$.

Naturally, the total number of grid cells increase linearly with N_r. The aspect ratio denotes the ratio between the longest and shortest length of a grid cells, and should ideally be 1. This would however require a very fine mesh. As seen in Figure 3.5 the maximum aspect ratio decreases as N_r is increased, and appears to stabilize at 3-4 for the finest grid refinement in radial direction.

It is evident that C_D and C_M depend on how well the boundary layer is resolved. The velocity profile in the boundary layer is described by a velocity gradient $\partial u/\partial y$ normal to the cylinder surface. $\partial u/\partial y$ is used to compute the vorticity, and can if not modelled correctly in the boundary layer cause whirl separation of inaccurate manner in the boundary layer. Faltinsen (1990) provided a formula for the boundary layer thickness η,

$$\eta = 4.6\sqrt{\frac{2\nu}{\omega}} \tag{3.12}$$

which is the distance from the surface surface to where the local velocity is 99% of the free stream velocity. In order to evaluate the effect of grid cell resolution of the boundary layer, the number of grid cells in radial direction N_r was held constant at 100, while the grading of the blocks surrounding the cylinder was adjusted. The grading was modified using the cell expansion ratio $simpleGrading$, that specifies the uniform expansions of the grid cells in local directions. The results are shown in Figure 3.6.

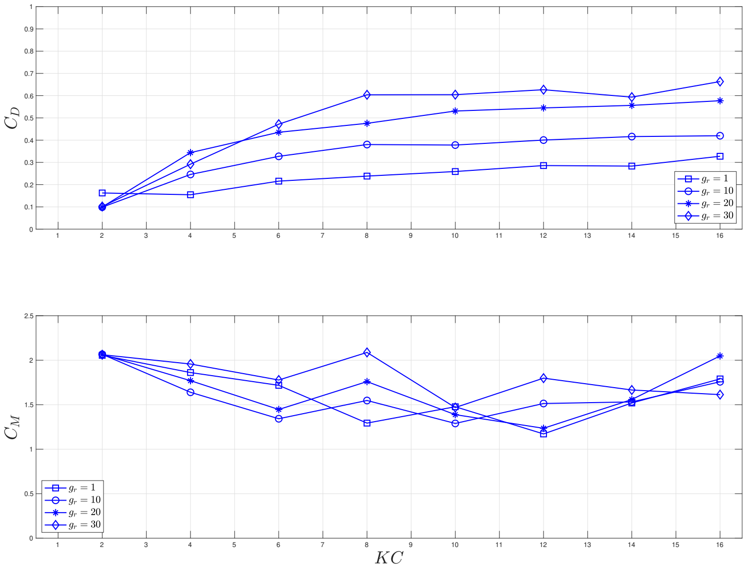

Figure 3.6: Drag coefficient C_D and added mass coefficient C_M for $g_r = 1$, $g_r = 10$, $g_r = 20$ and $g_r = 20$ with constant $N_r = 100$ and $N_c = 400$.

The grading of the inner domain clearly affects the computation of C_D and C_M. g_r denotes the uniform grading expansion of the grid cells in radial direction. The value for C_D is higher as the grading is increased from 1 to 30 from $KC > 4$, and develops with a higher gradient for $KC > 8$ as g_r is increased. The behaviour of C_D is similar for all gradings, increasing linearly up to $KC = 8$ and remaining relatively stable from $KC = 8$ to $KC = 16$. The computed value for C_D at $g_r = 30$ is twice as high as the value at $g_r = 1$ with no grading, but appears to stabilize at $g_r = 20$ and higher. The curves of C_M show that the computed values vary with g_r. Similar trends are observed as the KC number increases, with a decaying C_M for $KC < 6$, a slight increase and a dip at $KC = 12$ before increasing again. The irregularities for $g_r = 30$ at higher KC numbers are unexpected, as the curves were presumed to converge for higher values of g_r as the boundary layer got increasingly resolved. Why this occur is unclear, but such a high grading could make the cells at the cylinder surface very skewed as the width tangential to the cylinder surface of the cells are held constant during the grading test with $N_c = 400$. The plotted maximum aspect ratio in Figure 3.7 as a function of N_c does however suggest that the skewness of the cells are relatively unaffected as the grading is increased

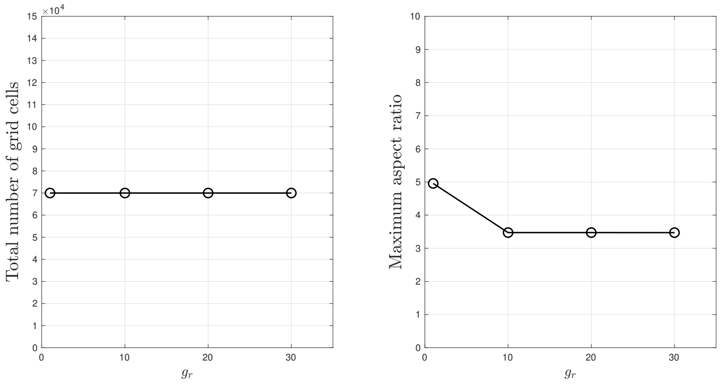

Figure 3.7: Total number of grid cells and maximum aspect ratio for mesh with $g_r = 1$, $g_r = 10$, $g_r = 20$ and $g_r = 20$ with constant $N_r = 100$ and $N_c = 400$.

Figure 3.7 shows that the maximum ratio is approximately 3.5 for when grading is applied. This is similar as for $N_r > 100$, meaning that increased grading is a good alternative to increased number of grid cells in radial direction in terms of aspect ratio of the grid cells.

The results from grid refinement in radial direction show that the mesh clearly influence the results. The aim of this convergence study is to identify a stable mesh that provides reasonable results. In terms of computational cost, a very fine mesh is undesirable. Based on the above results, the parameters in Table 3.2 are chosen for further tests.

N_r	g_r
100	20

Table 3.2: Conclusion grid refinement in radial direction.

3.8.2 Grid refinement along cylinder surface

The subdomain surrounding the cylinder consists of eight blocks, as seen in Figure 3.1. N_c denotes the total number of grid cells surrounding the cylinder surface, meaning that each block has a total og $\frac{N_c}{8}$ grid cells at the cylinder surface. Four cases with varying N_c are were run in order to assess the effect of N_c, and the results are given in Figure 3.8.

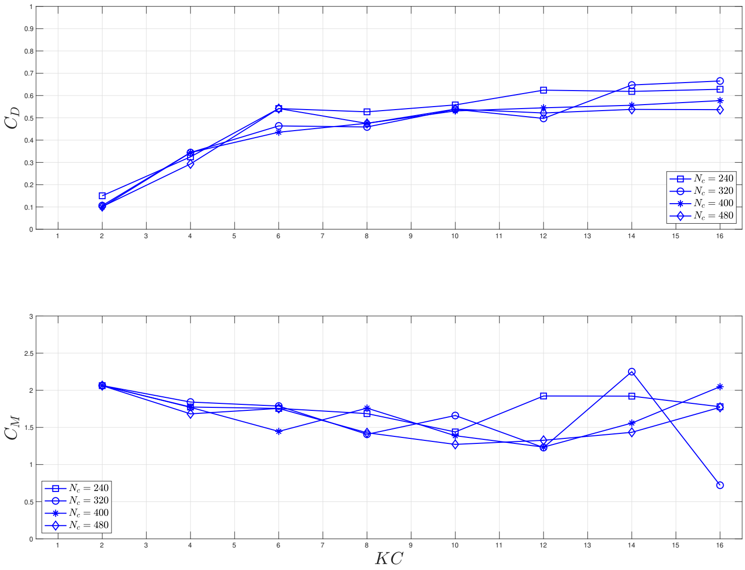

Figure 3.8: Drag coefficient C_D and added mass coefficient C_M for $N_c = 240$, $N_c = 320$, $N_c = 400$ and $N_c = 480$ with constant $N_r = 100$ and $g_r = 20$.

The results are relatively consistent for $KC < 6$, whereas C_D increases linearly up to $KC = 10$ before stabilizing. For some KC values it appears that a coarse mesh with $N_c = 240$ gives somewhat higher values of C_D than the finer meshes. The curves for C_M shows that a finer mesh with $N_c = 480$ gives a lower value than the coarser meshes at $KC > 6$, and coincides well with the curve for $N_c = 320$ for $KC \leq 8$ and $KC = 12$. As previously the results at higher KC numbers fluctuates seemingly randomly, but $N_c = 320$ and $N_c = 480$ show a relatively stable development at the flow conditions evaluated in this test.

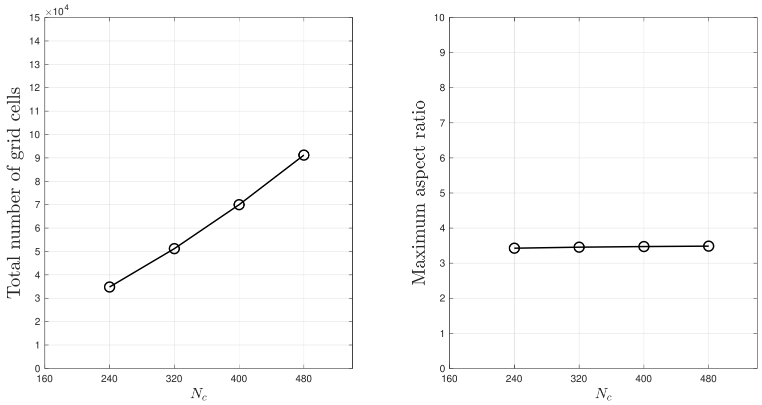

Figure 3.9: Total number of grid cells and maximum aspect ratio for mesh with $N_c = 240$, $N_c = 320$, $N_c = 400$ and $N_c = 480$ with constant $N_r = 100$ and $g_r = 20$.

Figure 3.9 shows how the total number of grid cells are increased with N_c. The maximum aspect ratio is unaffected by grid refinement along the cylinder surface.

N_c appears to affect the results at higher KC numbers. Due to the flucations at $N_c = 320$, the finest mesh with $N_c = 480$ is chosen for further studies. Table 3.3 summarizes the conclusions made from the convergence tests in this section.

N_r	g_r	N_c
100	20	480

Table 3.3: Conclusion grid refinement along cylinder surface.

3.8.3 Comparison with numerical and experimental results

The accuracy of the numerical model is evaluated by comparing the values for C_D and C_M to existing numerical and experimental results. Sæter (2019) and Fimland (2018) performed convergence studies of an oscillatory flow around a cylinder, and the optimum grid parameters from their respective studies are plotted in Figure 3.10 along with the results from the present numerical model. It should be noted that Fimland (2018) performed convergence studies at $Re = 10000$, while the convergence studies from the numerical model are performed at $Re = 70000$ in order to limit computational execution time.

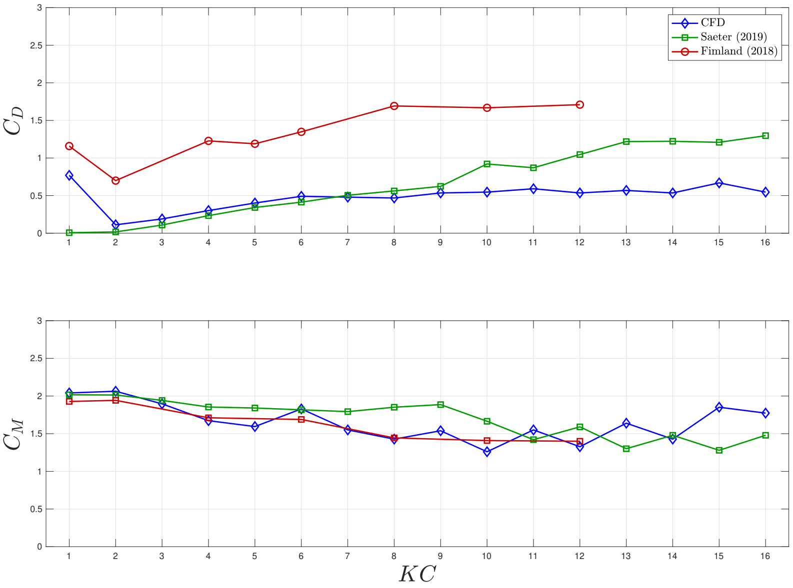

Figure 3.10: Comparison of results of drag coefficient C_D and added mass coefficient C_M from numerical simulations by Sæter (2019) (Re varying with KC) and Fimland (2018) ($Re = 10000$).

Figure 3.10 show that the results for C_D from the numerical model agree with the results from Sæter (2019) at $2 < KC < 9$. At higher KC values the computed values remain relatively stable at 0.5 while the results from Sæter (2019) continues to increase linearly up to almost twice the value at $KC = 16$. It should be noted that Sæter (2019) applied the $k - \omega$ turbulence model for wall treatment in his analysis, and found that the usage of a laminar model in his case provided a significantly lower C_D for $KC > 4$ stabilizing at $C_D \simeq 0.3 - 0.4$. The values for C_D from Fimland (2018) are higher than the numerical results, but behave in a similar trend with a dip at $KC = 2$ and stabilizing at $KC \simeq 8$.

The results for C_M seem to agree up to $KC = 6$. At KC values higher than 6 the values from the numerical model decreases in a similar matter as the results from Fimland (2018), whereas C_M from Sæter (2019) does not decrease until $KC > 9$.

There are discrepancies in the literature for KC-dependent C_M and C_D. Based on prior numerical and experimental results for oscillatory flows and discussions with supervisor, some trends were expected. These include a $C_M \leq 2$ for $KC \leq 5$, drop at $KC \simeq 6$ and a minimum at $KC = 10 - 12$. It is however observed that C_M drops already at $KC = 3$ an decreasing to $KC = 8 - 10$. At higher KC values higher than 8 the results fluctuate and an apparent minimum is not observed, but C_M does seem to increase as $KC > 12$. For C_D there was expected to be an approximate linearly increasing trend between $KC \simeq 2$ and $KC = 10 - 12$, before if flattens out and decreases somewhat. A linear trend for C_D is evident for $KC > 7$, but the curve flattens out earlier at $KC = 7 - 8$. There is not noticeable decrease at higher KC values.

In order to further assess the accuracy of the numerical model, values of C_D and C_M are plotted along with results by Sarpkaya (1976) at $Re = 20000$ and $Re = 40000$. The results are given below in Figure 3.11

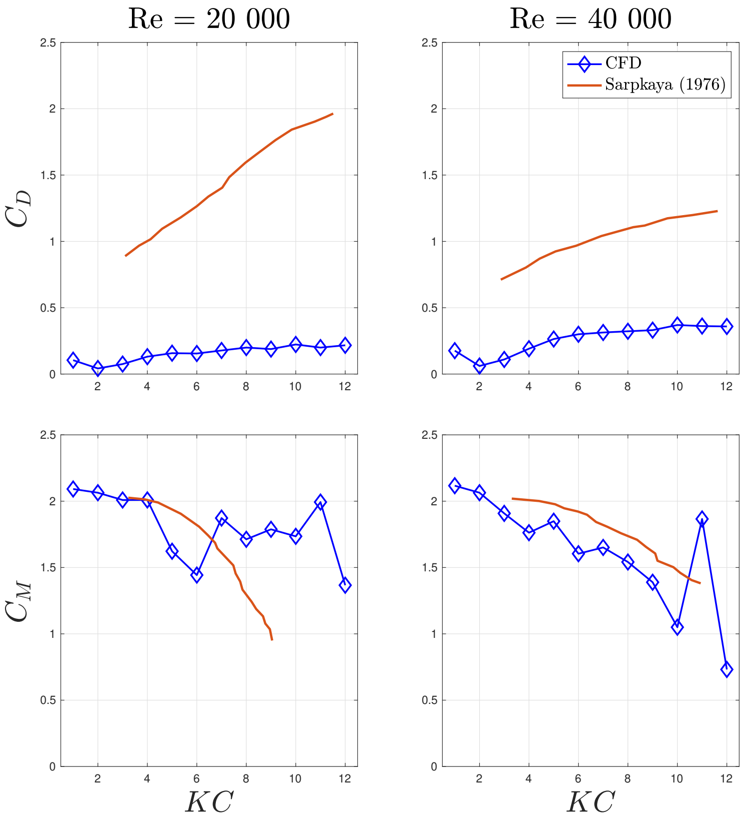

Figure 3.11: Comparison of results of drag coefficient C_D and added mass coefficient C_M from numerical simulations to experimental results by Sarpkaya (1976).

The numerical model significantly underestimates C_D. It appears that the model is unable to capture the skin friction drag contribution and provides a C_D under 0.5 for both $Re = 20000$ and $Re = 40000$. At $Re = 20000$ the model agrees for C_M up to $KC = 4$, where there is a sudden drop down to $KC = 8$ instead of a gradual decay as flow separates from the cylinder. For higher $KC > 8$ the C_M value suddenly increases before stabilizing. As observed in the convergence studies, the model is inconsistent for higher KC numbers, and the overprediction of the inertia force at low Re confirms this. The trend at $Re = 40000$ is similar to the results by Sarpkaya (1976) with a gradual decrease for increasing KC numbers as flow separates from the cylinder, though the values are seemingly underpredicted for $KC < 4$. At $KC = 11$ there is a sudden spike in C_M, whereas the value at $KC = 12$ follows the previously observed trend.

A comparison of the results from the numerical model in OpenFOAM with numerical and experimental results show that the numerical model is unreliable for higher KC numbers at low Re values. Though C_D is underpredicted according to empirical data from Sarpkaya (1976), the results show consistency with the numerical model by Sæter (2019) up to $KC \leq 9$. At $KC > 6$ the results appear to fluctuate randomly, which indicates that the model is not able to capture the inertia force at these levels. This can imply that the model has problems modelling flows with increased turbulence from vortex shedding, which can be explained by the use of a laminar simulation type. By applying turbulence modelling of the boundary layer around the cylinder surface this weakness could be improved, but due to time limitations this was not done in this thesis.

When simulating the wave forces around the cylinder the maximum KC number is assumed to approximately 10, so going forward it should be noted that the stability of the model at $KC > 6$ is uncertain.

3.9 Flow regimes

This section presents an overview of the flow regimes as a function of the KC number. The KC number as given by Equation (2.34) is a function of the maximum velocity U_m, the period of the oscillating flow T and the cylinder diameter D. The oscillatory flow considered up till now in the convergence studies is a sinusoidal flow with a velocity given by

$$U = U_m sin(\omega t) \tag{3.13}$$

with a maximum velocity of

$$U_m = A\omega = \frac{2\pi A}{T} \tag{3.14}$$

In order to maintain a constant Reynolds number Re at different KC values, the period T was adjusted accordingly. For a sinusoidal case the KC number can be rewritten as a function of the motion amplitude A.

$$KC = \frac{2\pi A}{D} \tag{3.15}$$

The right hand side of Equation (3.15) can be used to describe the physical meaning of the KC number. The numerator is proportional to the motion stroke $2A$ and the denominator D is the cylinder diameter which in this case is held constant. This means that at small KC number the orbital motion of the fluid particles is small relative to the diameter. For high KC numbers however, the fluid particles move large distances compared to the diameter.

Figure 3.12 shows the flow regime at $KC = 2$. There is no vortex shedding occurring behind or in front of the cylinder, and the flow behaves like a creeping flow where the inertial forces are small compared to the viscous forces.

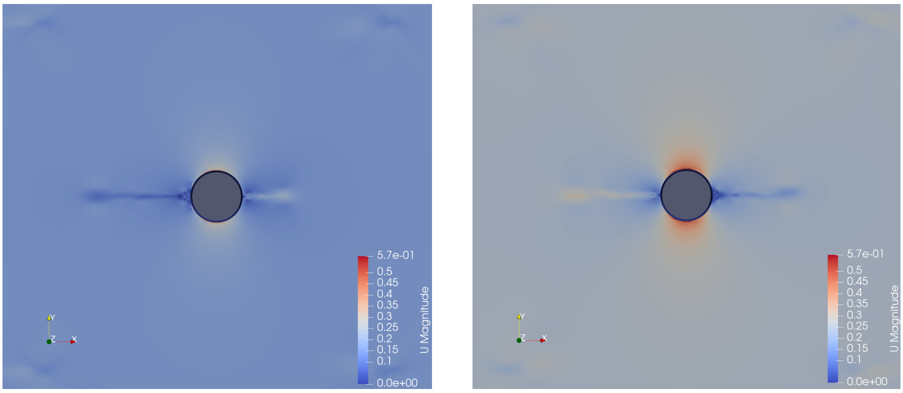

(a) Flow direction left.

(b) Flow direction right.

Figure 3.12: Flow regime for $KC = 2$ at $Re = 40000$.

Flow separation occurs as the KC number is increased to 4. The shedding around the cylinder first builds up as a pair of symmetric vortices as flow separates, as seen in Figure 3.13. As the flow builds up over a few periods, the vortices increase in size and move further away from the separation point. Eventually the symmetry between the attached vortices breaks down and a vortex shedding regime is established.

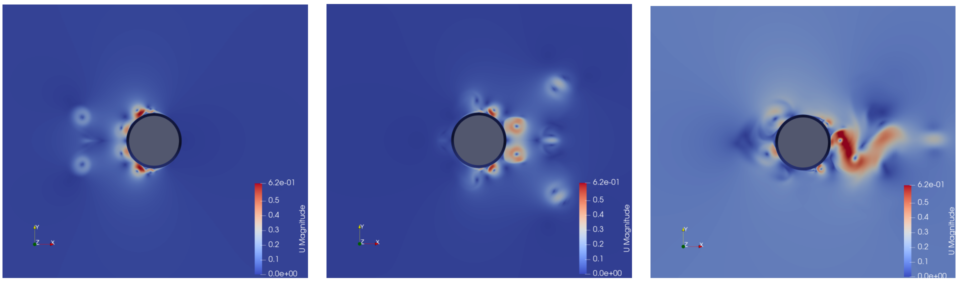

Figure 3.13: Build up of vortex shedding in flow regime for $KC = 4$ at $Re = 40000$.

The vortex shedding regime for $KC = 4$ is given in Figure 3.14. The vortex shedding in this regime occurs each half period of the oscillatory motion as the flow separates from the cylinder surface, and the vortices are pushed on the other side of the cylinder as the flow changes direction.

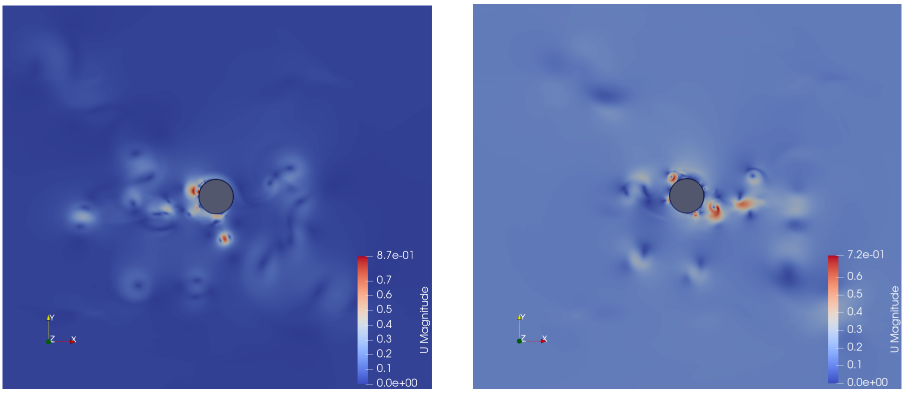

(a) Flow direction left.

(b) Flow direction right.

Figure 3.14: Flow regime for $KC = 4$ at $Re = 40000$.

It is clear that the water particles move further away from the cylinder as the KC number is increased. The flow regime for $KC = 6$ in Figure 3.15 shows that the vortices move larger distances both horizontally and vertically relative to the cylinder compared to $KC = 4$, creating a shedding regime over larger area of the flow.

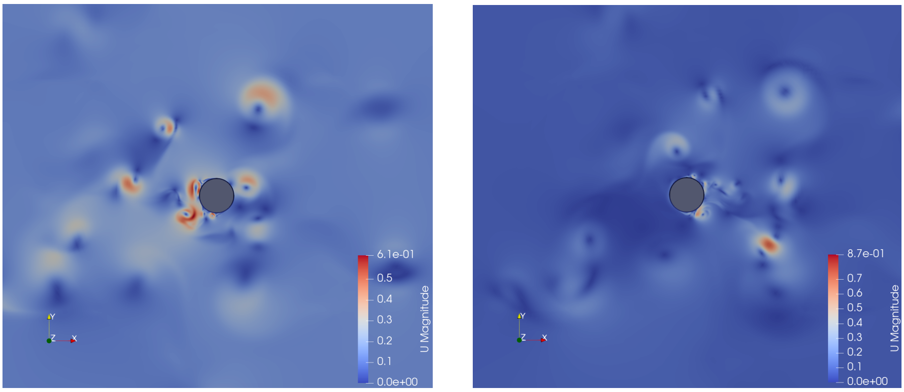

(a) Flow direction left.

(b) Flow direction right.

Figure 3.15: Flow regime for $KC = 6$ at $Re = 40000$.

As KC is increased to 8, the flow regime becomes less organized. Williamson (1985) found that for $7 < KC < 15$ the main vortices shed from the cylinder induce velocity, which creates a trail of vortices perpendicular to the horizontal flow direction. This is denoted as a transverse vortex street, and occurs as vortices are shedding on either the lower or upper side of the cylinder. Observations by Williamson (1985) indicated that the vortex street can changes sides relative to the cylinder. This phenomenon is however not clearly evident in the flow visualization in Figure 3.16. This could be due to the simulation time terminating at $10T$, and that a transverse vortex street had not yet formed at this point.

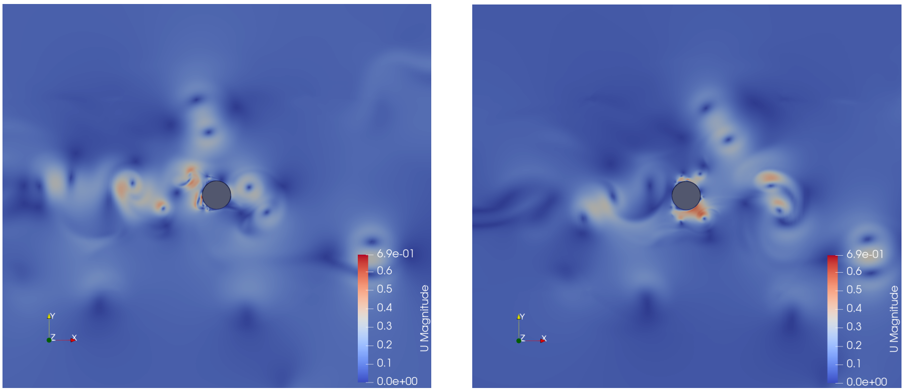

(a) Flow direction left.

(b) Flow direction right.

Figure 3.16: Flow regime for $KC = 8$ at $Re = 40000$.

The flow regime for $KC = 12$ is shown in Figure 3.17. Here the vortices behave in a similar observed trend, moving at larger distances horizontally and vertically from the cylinder. The snapshot of the flow regime for the right flow direction show that the vortex pairs upstream of the cylinder move towards the top left corner of the flow domain, and could indicate that a transverse vortex street has formed in this direction.

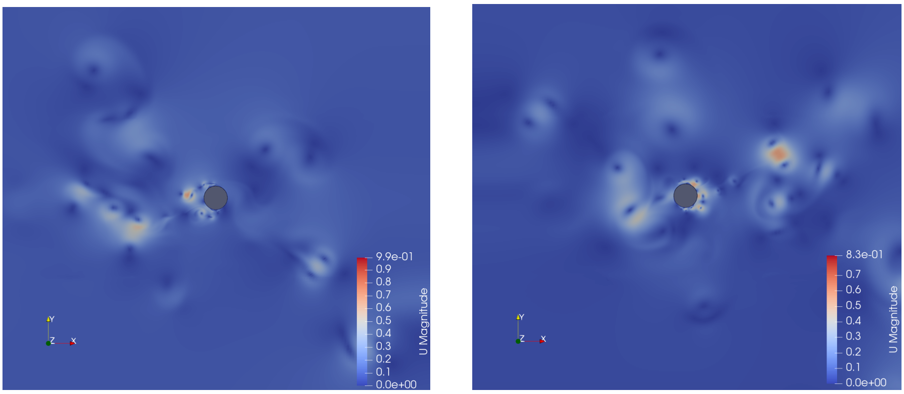

(a) Flow direction left.

(b) Flow direction right.

Figure 3.17: Flow regime for $KC = 10$ at $Re = 40000$.

Vortices shedding from the cylinder dissipate into the domain, which can indicate that the use of a laminar model prevents turbulence in the flow to soothe out the vortices further away from the cylinder. As KC is increased the vortices move in the changing flow direction, and the fluctuations in the results in this range could perhaps be explained by the influence of distant vortices.

Chapter 4

Method

This chapter introduces the combined 3D CFD-FNV load model, including derivation of the new three dimensional term and computation of wave forces on a discretized monopile. The implementation of Stokes fifth order waves as input is described, and the test conditions used to evaluate the 3D CFD-FNV load model are presented.

4.1 3D CFD-FNV load model

Slender body theory is used to approximate the solution to Stokes flow around bodies that are long compared to their cross-sectional dimensions. Existing FNV theory does not include slender body terms accounting for three dimensional effects, such as upwelling as observed in experiments by Kristiansen and Faltinsen (2017). This section is dedicated to a derivation of the 3D CFD-FNV load model that will be used to evaluate the effects of three dimensional slender body terms in nonlinear higher harmonic waves interacting with an OWT monopile. It it important to note that the load model is called 3D CFD-FNV due to the addition of a three dimensional term, and not due to three dimensional CFD simulations. The CFD simulations used in the combined load model are only performed for two dimensional flows.

In order to derive the 3D CFD-FNV load model for a monopile, we first consider the three dimensional Navier Stokes equations in x- and y-direction, neglecting the gravity term.

$$\frac{\partial u}{\partial t} + u\frac{\partial u}{\partial x} + v\frac{\partial u}{\partial y} + w\frac{\partial u}{\partial z} = -\frac{1}{\rho}\frac{\partial p}{\partial x} + \nu\nabla^2 U \tag{4.1}$$

$$\frac{\partial v}{\partial t} + u\frac{\partial v}{\partial x} + v\frac{\partial v}{\partial y} + w\frac{\partial v}{\partial z} = -\frac{1}{\rho}\frac{\partial p}{\partial y} + \nu\nabla^2 U \tag{4.2}$$

The vertical velocity w is assumed to be known from fifth order Stokes theory, and unaffected by the presence of the monopile. Furher, the pressure term p in Equation (4.1) and Equation (4.2) is divided into two components:

$$p = p^{CFD} + p^{w} \tag{4.3}$$

The component p^{CFD} is the contribution from two dimensional CFD simulations, and the component p^{w} accounts for the three dimensional effects. By implementing the new definition for the pressure term, Equation (4.1) can be split into two equations,

$$\frac{\partial u}{\partial t} + u\frac{\partial u}{\partial x} + v\frac{\partial u}{\partial y} = -\frac{1}{\rho}\frac{\partial p^{CFD}}{\partial x} + \nu\nabla^2 U \tag{4.4}$$

$$w\frac{\partial u}{\partial z} = -\frac{1}{\rho}\frac{\partial p^{w}}{\partial x} \tag{4.5}$$

The strip theory approach is applied to compute the wave forces on the monopile. Strip theory involves dividing a submerged structure into a finite number of strips, and determining the three dimensional force on the total structure by computing the two dimensional force on each strip and summing the force components over the length of the body. The Eulerian specification is used for discretization of the monopile into strips, as seen in Figure 4.1.

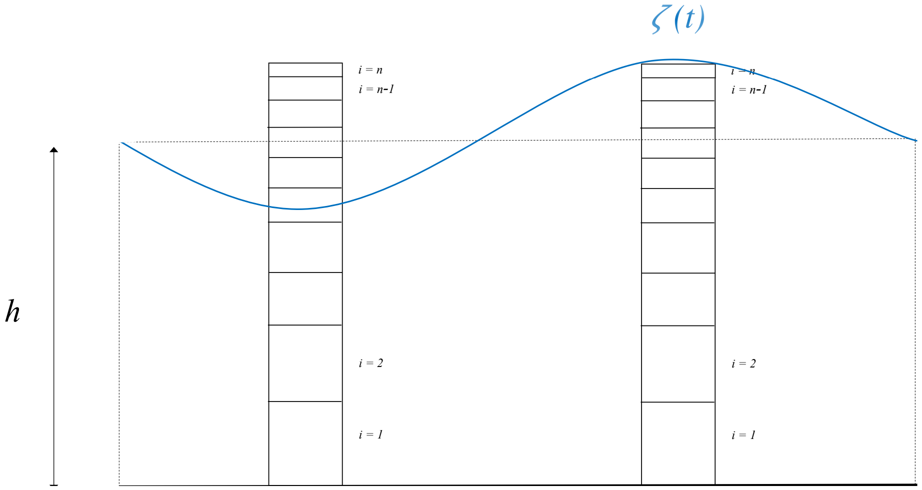

Figure 4.1: Eulerian discretization of monopile into n strips.

The monopile is discretized into n strips. The Eulerian specification involves strips with fixed thickness throughout the flow cycle, where the fluid properties are functions of space and time. The strips have varying thickness Δz_i, whereas the thickness gets smaller from the seabed and up to the mean free surface $z = 0$. This is done in order to reduce computational costs. The strips at the surface are thinner than the ones on the seabed, since the velocity gradient is significantly higher than near the seabed. The monopile radius a is assumed to be constant.

The monopile is discretized using a stretched mesh in z-direction, equivalent to the stretched mesh using by Fimland (2018).

$$\Delta z_i = \alpha^{i-1} \Delta z_1 \tag{4.6}$$

where α and Δz_1 is the strip on the bottom of the monopile touching the seabed. Δz_1 is defined as

$$\Delta z_1 = \alpha^{i-1} \Delta z_1 \tag{4.7}$$

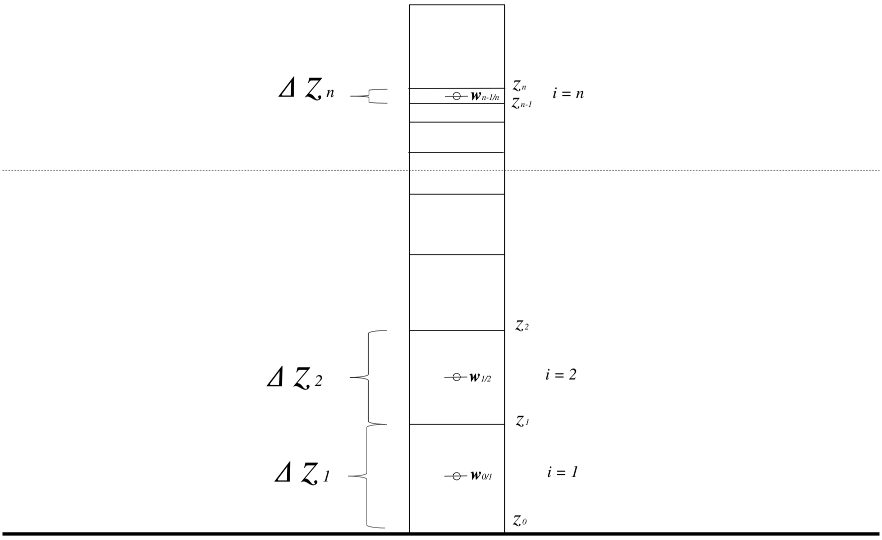

Figure 4.2: Notation for strip and plane numbering in discretization of monopile into n strips.

The two dimensional CFD pressure p^{CFD} on strip i is found with two dimensional CFD simulations of the strip in OpenFOAM at $z = z_{i-1}$ and $z = z_i$. The output from the two separate simulations provide the horizontal velocity $u(z_{i-1})$ and $u(z_i)$, along with the horizontal force $F^{CFD}(z_{i-1})$ and $F^{CFD}(z_i)$. The total two dimensional force in the middle of strip i is found by interpolating the force at z_i and z_{i-1} from the CFD simulations,

$$F_i^{CFD} = \frac{F^{CFD}(z_i) + F^{CFD}(z_{i-1})}{2} \tag{4.8}$$

$z_{i-1/i}$ is the vertical coordinate at the middle of strip i, according to Figure 4.2.

$$z_{i-1/i} = \frac{z_i + z_{i-1}}{2} \tag{4.9}$$

This means that z_0 is the bottom and z_1 the top of strip 1, and the middle of the strip is at $z_{0/1}$. Similarly, z_1, z_2 and $z_{1/2}$ account for strip 2 and so on.

Two dimensional CFD simulations are performed at xy-planes located at $z = z_0$, $z = z_1$,

..., $z = z_n$ to the top of strip n. At strip i with thickness Δi, the horizontal velocity tangential to the bottom and the top are $u(z_{i-1})$ and $u(z_i)$ from CFD simulations. $w_{i-1/i}$ is the vertical velocity in the middle of strip i, and is assumed to be known from fifth order Stokes wave theory. The left side of Equation (4.5) can then be approximated as

$$w\frac{\partial u}{\partial z}\bigg|_{z_{i-1/i}} \simeq w_{i-1/i}\frac{u_i + u_{i-1}}{\Delta z_i} \tag{4.10}$$

The pressure at the boundaries of the domain is assumed to be known from the two dimensional Bernoulli equation. The pressure acting on the monopile surface at $r = a$ is denoted $p(a)$, and is further referred to as p^w accounting for three dimensional effects. The pressure p^w on the monopile can be determined by integrating the pressure gradient from the monopile surface to domain boundaries, which yields

$$p^w(a, \theta, z_{i-1/i}) - \underbrace{p(r_d)}_{\text{known}} = \int_{r_d}^{a} \frac{\partial p^w}{\partial x} dl = -\rho \int_{r_d}^{a} w\frac{\partial u}{\partial z} dl \tag{4.11}$$

where $p(r_d)$ is the pressure at the radius r_d of the far field circular control surface. r_d is a distance from the monopile where the flow is not affected by the body. In the numerical model in OpenFOAM, this distance is defined as $r_d = r + L/2$ as seen in Figure 4.3.

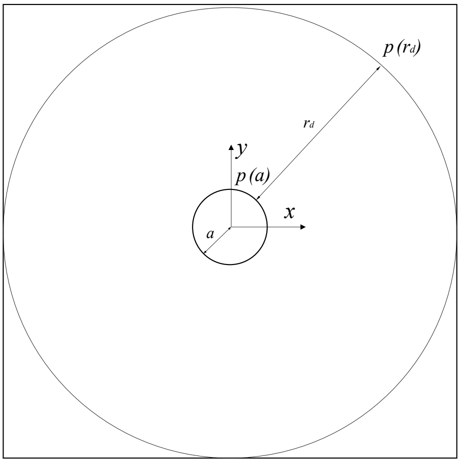

Figure 4.3: xy-plane of domain at $z = z_i$ with monopile radius a and far field circular control surface r_d.

$p(r_d)$ is determined from the potential flow solution for a dipole. The velocity components at r_d in radial and angular direction are defined according to Equation (4.12) and Equation (4.13).

$$u_r(r_d, \theta, z_{i-1/i}) = u(z_{i-1/i})\Big(1 - (\frac{a}{r_d})^2\Big)cos\theta \tag{4.12}$$

$$u_\theta(r_d, \theta, z_{i-1/i}) = -u(z_{i-1/i})\Big(1 - (\frac{a}{r_d})^2\Big)sin\theta \tag{4.13}$$

where a is the radius of the monopile and $u(z_{i-1/i})$ is the horizontal velocity in the middle of the strip, known from Stokes fifth order wave theory. The pressure at r_d can then be determined from the two dimensional Bernoulli equation as

$$p(r_d, \theta, z_{i-1/i}) = \frac{1}{2}\rho(u_\theta^2 + u_\theta^2) \tag{4.14}$$

With r_d held constant in the analysis, $p(r_d)$ in the xy-plane at $z_{i-1/i}$ is a function of θ. As of Equation (4.5), the above expression for p^w can be rewritten as follows,

$$\begin{aligned} p^w(r, \theta, z_{i-1/i}) &= p(r_d, \theta, z_{i-1/i}) - \rho \int_{r_d}^{a} w \frac{\partial u}{\partial z} dl \\ &\simeq p(r_d) - \rho \int_{r_d}^{a} w_{i-1/i} \frac{u_i + u_{i-1}}{\Delta z_i} dl \end{aligned} \tag{4.15}$$

In order to obtain the numerical values for u_i and u_{i-1} in OpenFOAM, the magnitude of the velocity is measured using the probe function. 100 probes along probelines evenly distributed radially at an angle θ around the cross-section from r to r_d are implemented in the two dimensional numerical model, as illustrated in Figure 4.4.

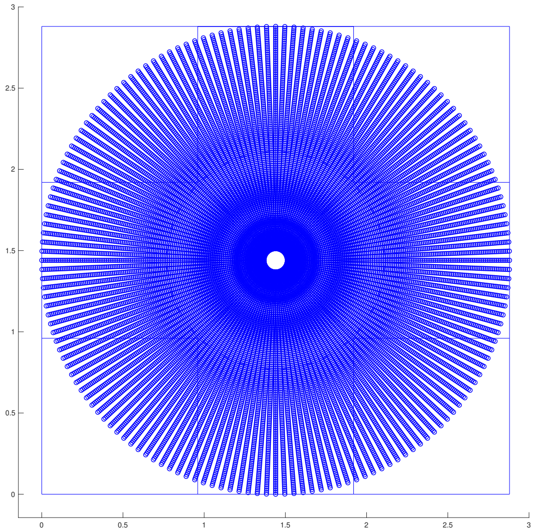

Figure 4.4: Probelines around the monopile from $r = a$ to $r = r_d$ at the monopile cross-section at plane $z = z_i$.

The integration in Equation (4.15) are performed in post processing by numerically integrating over the velocity at the 100 probes along the probelines at $(r, \theta_j, z_{i-1/i})$.

This provides the pressure p^w at $(r, \theta_j, z_{i-1/i})$ for strip i. In order to obtain the force component, the monopile circumference is discretized into elements with straight lines tangential to the surface with equal length Δs. The force component on each element at angle θ_j is then

$$F^w(r, \theta_j, z_{i-1/i}) = \Delta s \cdot p^w(r, \theta_j, z_{i-1/i}) \cdot \mathbf{n} \tag{4.16}$$

where **n** is the normal vector of the element surface into the surrounding flow. The total three dimensional force contribution is then found by summing the force on all the elements around the monopile:

$$F_i^w = \sum_{j=1}^{k} \Delta s \cdot p^w(r, \theta_j, z_{i-1/i}) \tag{4.17}$$

The total force including both the two and three dimensional force components for on strip i is determined by multiplying with the strip thickness Δz_i. Due to the Eulerian discretization scheme, the submergence of the strips will vary with the incident free surface ζ as a function of time. This means that the strips above the surface will not contribute to the horizontal force. To account for this, the computed force components at strip i are set to zero when the center of the strip if submerged, i.e. $F_i^{CFD} + F_i^w = 0$ if $z_{i-1/i} > \zeta$ as illustrated in Figure 4.5 below.

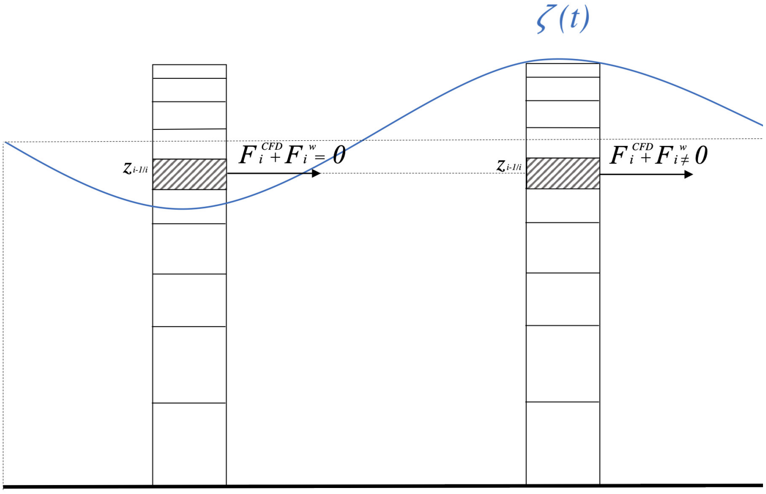

Figure 4.5: Force distribution on strip i at $\zeta < z_{i-1/i}$ and $\zeta > z_{i-1/i}$.

The new force terms are combined with existing FNV theory by replacing the time derivative terms in Equation (2.44) with F_i^{CFD} and adding the three dimensional contribution F_i^w for all n strips. The terms in the new 3D CFD-FNV load are as follows,

$$F_x = \sum_{i=1}^{n} F_i^{CFD} \Delta z_i + \sum_{i=1}^{n} F_i^w \Delta z_i + \int_{-h}^{\zeta} \left(a_{11} u \frac{\partial u}{\partial x} + 2 a_{11} w \frac{\partial u}{\partial z} \right) + F^{\psi} \tag{4.18}$$

where

$$F^{\psi} = \rho \pi a^2 \frac{4}{g} u^2 \frac{\partial u}{\partial t} \bigg|_{z=0} \tag{4.19}$$

4.2 Input

The wave kinematics input for the 3D CFD-FNV load model are computed using Stokes fifth order wave theory. The method in Section 2.1.5 by Skjelbreia and Hendrickson (1960) was implemented in MATLAB in order to obtain the time series for the relevant kinematics as a function of wave period T, wave steepness H/λ and water depth h. In order to estimate the fluid motion from the seabed and up to the incident free surface, the components are Taylor expanded for $h < z \leq \zeta$. Considering the wave kinematics components as a function f, this gives

$$\begin{aligned} f(z) = (f_1 + f_2 + f_3 + f_4 + f_5)\big|_{z=0} + z\left.\frac{\partial(f_1 + f_2 + f_3 + f_4)}{\partial z}\right|_{z=0} + ... \\ \frac{z^2}{2}\left.\frac{\partial^2(f_1 + f_2 + f_3)}{\partial z^2}\right|_{z=0} + \frac{z^3}{6}\left.\frac{\partial^3(f_1 + f_2)}{\partial z^3}\right|_{z=0} + \frac{z^4}{24}\left.\frac{\partial^4 f_1}{\partial z^4}\right|_{z=0} \end{aligned} \tag{4.20}$$

where f_i is the i-th order Stokes wave theory. The Taylor expanded horizontal velocity u for $ka = 0.127$ and $ka = 0.105$ are shown in red in Figure 4.6.

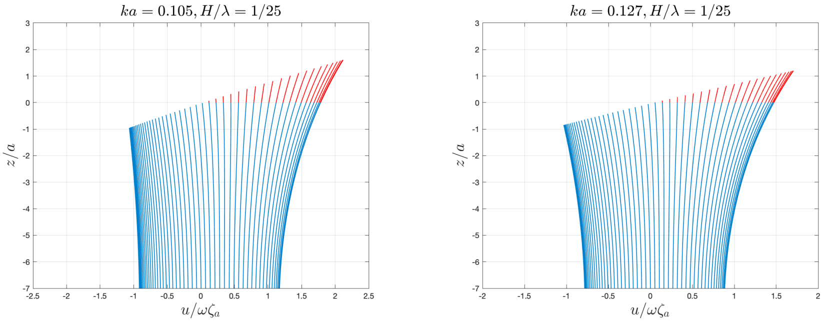

Figure 4.6: Horizontal velocity u from Stokes fifth order wave theory for $ka = 0.105$ and $ka = 0.127$ at wave steepness $H_1/\lambda = 1/25$ at $h/a = 7.83$ with time step $T/100$.

The time is discretized by dividing the time period into a constant number intervals. The time steps used under for the following test conditions are $T/100$.

4.3 Test conditions

Kristiansen and Faltinsen (2017) performed experiments of a single monopile in long and moderately steep waves in deep to intermediate depth wave conditions. The experiments were carried on in the medium-sized wave tank at the Marine Techonology Centre at NTNU. The full scale monopile diameter was $D = 6.9\ m$ at water depths $h = 27\ m$ and $h = 19\ m$, and tested at full scale wave periods at $T = 6\ s$ and $T = 16.5\ s$. The model tests were Froude scaled by 1:48, with a model monopile diameter of $D = 0.144\ m$ and radius $a = 0.072\ m$ at water depths $h = 0.5635\ m$ and $h = 0.3958\ m$. The test conditions used to evaluate the 3D CFD-FNV load model are chosen so that they match the test condition parameters using in the model tests at $h = 0.5635$. The wave steepness used in test conditions range from $H_1/\lambda = 1/100$ to $H_1/\lambda = 1/20$, whereas H_1 denotes the linear wave height from linear wave theory. The relevant test condition parameters are presented in Table 4.1, including model scale and full scale wave period T_M and T_F.

$h/a = 7.83$						
ka $[-]$	T_M $[s]$	T_F $[s]$	KC_1 $[-]$	KC_5 $[-]$	Ur $[-]$	$Re/10^3$ $[-]$
0.388	0.866	6.000	1.0	1.2	0.4	24.3
0.290	1.010	6.998	1.4	1.6	0.9	27.9
0.229	1.155	8.002	1.7	2.1	1.7	30.8
0.190	1.299	9.000	2.1	2.7	3.0	33.1
0.163	1.443	9.997	2.4	3.4	4.8	34.8
0.142	1.588	11.002	2.8	4.3	7.2	36.1
0.127	1.732	12.000	3.1	5.3	10.1	37.1
0.115	1.876	12.997	3.4	6.5	13.7	37.9
0.105	2.021	14.002	3.8	8.0	17.9	38.5
0.097	2.165	15.000	4.1	9.7	23.0	39.0
0.090	2.309	15.997	4.4	11.8	28.8	39.4

Table 4.1: Test condition parameters from model tests by Kristiansen and Faltinsen (2017). KC_1, KC_5, Ur and Re are given for wave steepness $H_1/\lambda = 1/25$.

KC_1 and KC_5 are the maximum KC number present in the wave condition according to linear and Stokes fifth order wave theory respectively. The maximum KC number refer to the maximum wave particle velocity at the wave crest. As seen in Table 4.1, $KC_5 > 6$ for longer waves at $ka > 0.127$ and higher for $H_1/\lambda = 1/25$. The limitations of the numerical model in this KC range should therefore be considered when evaluating the results at these ka values. It should also be noted that Ur for all test conditions presented in Table 4.1 are within the validity limit of $Ur < 40$ for Stokes fifth order wave theory as presented by Hedges (1995).

Chapter 5

Results and discussion

This chapter presents the results from the 3D CFD-FNV load model, along with discussion of the findings. First, the parameters used to set up the load model are discussed. Further, the 3D CFD-FNV model is evaluated by comparing the results to experimental data and theoretical predictions with focus on the third load harmonic. The contribution from the added three dimensional term is investigated closer in a separate section. Recommendations for further work are provided at the end of this chapter.

5.1 Set up

The 3D CFD-FNV load model was performed for the test conditions in Section 4.3. The monopile was discretized into 10 strips, resulting in two dimensional CFD simulations at 11 planes on the top and bottom of each strip for each wave condition. The strip thickness was stretched as described in Section 4.1, and the height of the monopile above the mean free surface was adjusted according to the test conditions as seen in Figure 5.1.

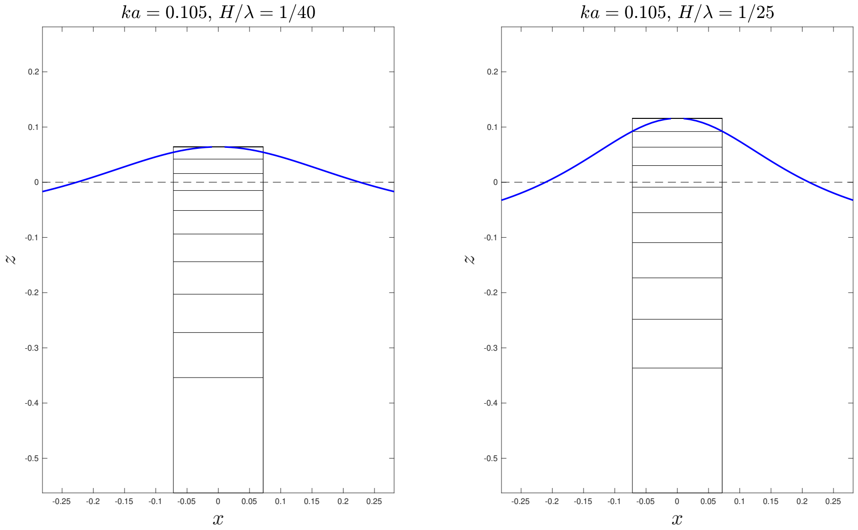

Figure 5.1: Discretization of monopile into 10 strips at for $ka = 0.105$ at wave steepness $H_1/\lambda = 1/40$ and $H_1/\lambda = 1/25$ at $h/a = 7.83$. The blue line represents the free surface ζ.

One probeline for each third grid cell along the cylinder surface was applied to measure the horizontal velocity in the plane, resulting in a total of 160 probelines distributed evenly around the cylinder circumference.

Due to the Eulerian discretization scheme of the monopile, the flow regime on the horizontal planes on top and bottom of the strips vary vertically. As seen in Figure 4.6, the magnitude of the horizontal velocity is higher close to the fifth order free surface. The strips located on top of the monopile near the free surface will therefore experience a higher velocity than the strips on near the seabed. Consequently, the maximum KC numbers on each strip increases. The maximum KC number for the horizontal planes according to Stokes fifth order theory denoted KC_5 are shown in Figure 5.2 for $ka = 0.105$ and $ka = 0.127$, and are determined by the maximum horizontal velocity at the vertical location of the plane.

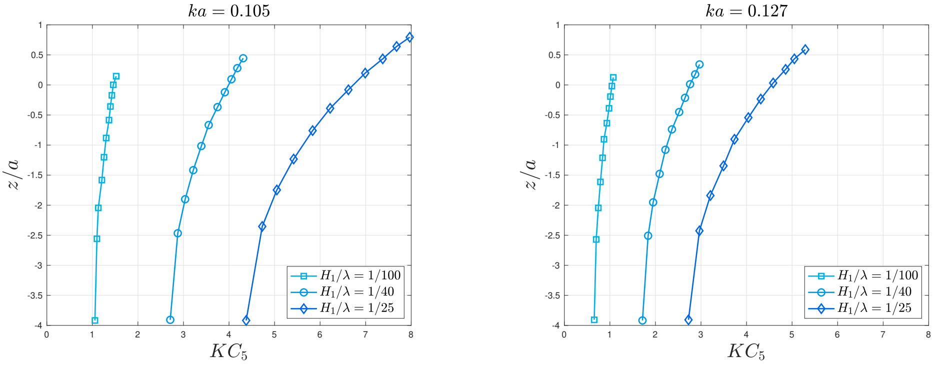

Figure 5.2: KC_5 at z-planes 0 to 11 for $ka = 0.105$ at wave steepness $H_1/\lambda = 1/40$ and $H_1/\lambda = 1/25$ at $h/a = 7.83$.

As seen in Figure 5.2, KC_5 increases as the waves get steeper and longer. KC_5 gets higher as the plane location is closer to the free surface, and develops faster for steeper waves. The lower planes experience a higher KC_5 magnitude for these wave conditions, indicating that flow separation is expected to occur at closer to the seabed as the wave steepness is increased. As discussed in Section 3.8 the numerical model is unreliable for $KC > 6$, which means that the accuracy of the results for longer with with low ka number and higher wave steepness at the top strips are uncertain.

5.2 Comparison of experimental results, the FNV method and the 3D CFD-FNV load model

The results from the 3D CFD-FNV load model for the test conditions in Table 4.1 are provided in Appendix A.2. The time series for the total and first three harmonics of horizontal force as predicted by the 3D CFD-FNV load model are plotted against the results from the FNV method. A MATLAB band-pass filtering script provided by supervisor is used to isolate the first, second and third harmonic loads. A notable difference between the two methods is seen in the predictions of the total horizontal force for longer and steeper waves. The force predictions by the 3D CFD-FNV load model is lower in the wave propagation direction, resulting in lower force amplitudes. The force in the opposite direction is however unaffected. This is due to an irregularity occurring after the the troughs in the predicted total horizontal force on the monopile that appears for longer and steeper waves for $ka > 0.127$. An example of this is shown in Figure 5.3.

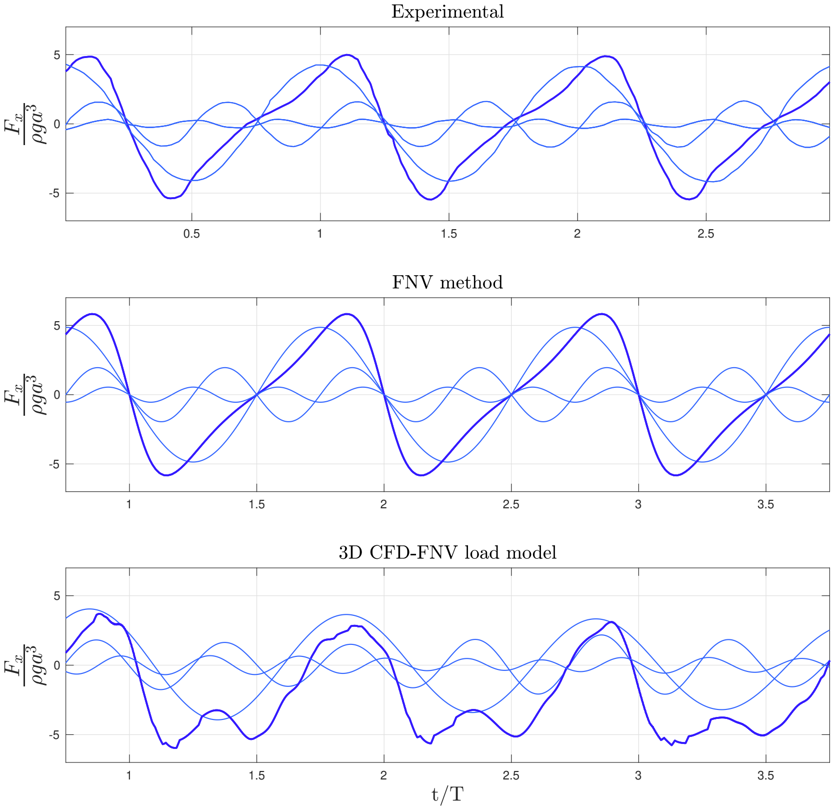

Figure 5.3: Example of time series of the total and first three harmonics of the horizontal force for $ka = 0.105$ and $H/\lambda = 1/25$ at water depth $h/a = 7.83$ from experimental results, FNV method and 3D CFD-FNV load model.

This first occurs for steeper waves at $ka > 0.127$. It appears as if the monopile experiences an additional force reducing the first load harmonic and occur as a peak at the force series troughs. Since this occurs at the troughs, an possible explanation for the irregular peaks could be the force at non-subermged strips being set to zero causing discontinuities in the force summations. These peaks are however not present for $ka < 0.127$.

$KC_5 > 6$ for steep waves at $ka > 0.127$, as mentioned in Section 5.1. As the numerical model is unreliable at KC number above 6, it is likely that the computed viscous force on the cylinder provided by the CFD pressure force is affected by weaknesses in the numerical model.

As seen in Figure 5.3, the 3D CFD-FNV load model overpredicts the third harmonic load. The third order incident potential is zero at infinite water, but accounts for a significant contribution to the third harmonic load at finite water (Kristiansen and Faltinsen, 2017). It can be seen that the theoretical third load harmonic is higher than the experimental as well, and in closer agreement to the results from the 3D CFD-FNV load model. The third load harmonic from the 3D CFD-FNV load model is somewhat out of phase with the experimental and theoretical third load harmonic.

The nondimensional horizontal force amplitude of the first three harmonics for $H_1/\lambda = 1/40$ and $H_1/\lambda = 1/25$ as predicted by the 3D CFD-FNV load model is plotted in Figure 5.4 against experimental and theoretical results. In order to assess the three dimensional term added to the load model in Equation (4.18), the predicted amplitude from the method without the three dimensional term in plotted as well. This is denoted as CFD-FNV in the figures.

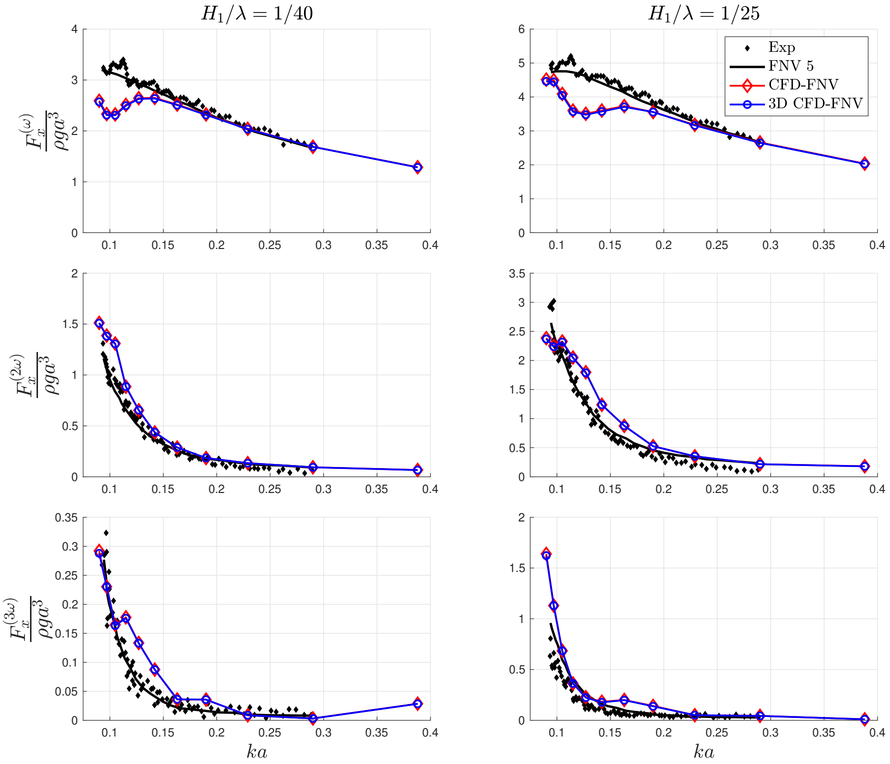

Figure 5.4: Horizontal force amplitude of the first three harmonics for $H_1/\lambda = 1/40$ and $H_1/\lambda = 1/25$ at water depth $h/a = 7.83$ from experimental results, FNV method, CFD-FNV load model and 3D CFD-FNV load model.

For wave steepness $H_1/\lambda = 1/40$ the 3D CFD-FNV load model agrees well with both experimental and theoretical results all three harmonics for $ka > 0.127$. For the shortest waves in this range the in-line inertia forces dominates, and the viscous forces predicted by the CFD simulations are small. At lower ka values for longer waves, the first harmonic is underpredicted by the method. The predicted second harmonic load is relatively well predicted, but somewhat higher for the longest waves. The third harmonic load is overpredicted for $0.229 < ka < 0.105$, whereas the method agrees remarkably well with experimental and theoretical results for the lowest ka values. The compliance for the third harmonic appears to occur approximately as the dip in the first harmonic occurs, and is likely due to the out of phase contribution from linear diffraction computed theoretically from FNV in the load model.

For the steeper wave condition $H_1/\lambda = 1/25$, a similar trend for the first harmonic load is observed. The amplitude is underpredicted earlier and the discrepancies are apparent at $ka = 0.190$. The second harmonic load is overpredicted by the 3D CFD-FNV load model for $0.229 < ka < 0.115$, whereas the predicted amplitude longest waves are lower than the theoretical and experimental results. As for the third harmonic, the 3D CFD-FNV load model overpredicts the amplitude for $0.229 < ka < 0.190$, similar as the case for the second harmonic load. The third harmonic load amplitude for the steepest waves at $ka > 0.105$ are significantly higher than the experimental results.

As seen in the figure for both $H_1/\lambda = 1/40$ and $H_1/\lambda = 1/25$, the three dimensional term in the 3D CFD-FNV load model does not contribute to the amplitude of either one the first three harmonics. The third harmonic load amplitude for the longest waves is a little bit lower for the 3D CFD-FNV compared to the CFD-FNV load model, but the difference is almost unnoticeable. This comparison of the load models show that the three dimensional contribution is negligible.

In order to assess how the wave steepness affects the nondimensional horizontal force amplitude, the 3D CFD-FNV load model is tested at constant ka values and wave steepness H_1/λ ranging from $1/100$ to $1/20$. The results are shown in Figure 5.5.

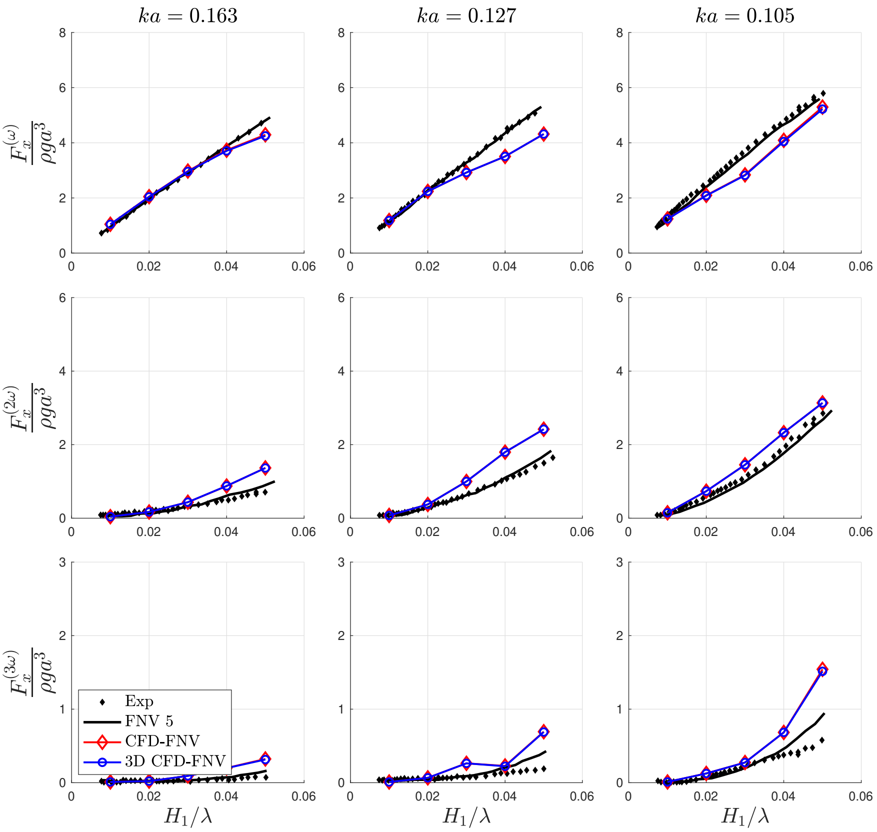

Figure 5.5: Horizontal force amplitude of the first three harmonics for $ka = 0.163$, $ka = 0.127$ and $ka = 0.105$ versus wave steepness H_1/λ at water depth $h/a = 7.83$ from experimental results, FNV method, CFD-FNV load model and 3D CFD-FNV load model.

The discrepancies in the first harmonic load amplitude occur for lower steepness as the waves get longer and ka decreases. This indicates that the underprediction of the force is related to KC. In order assess this relation, the values in Figure 5.4 and Figure 5.5 are plotted as a function of KC_5 in Figure 5.6 and Figure 5.7.

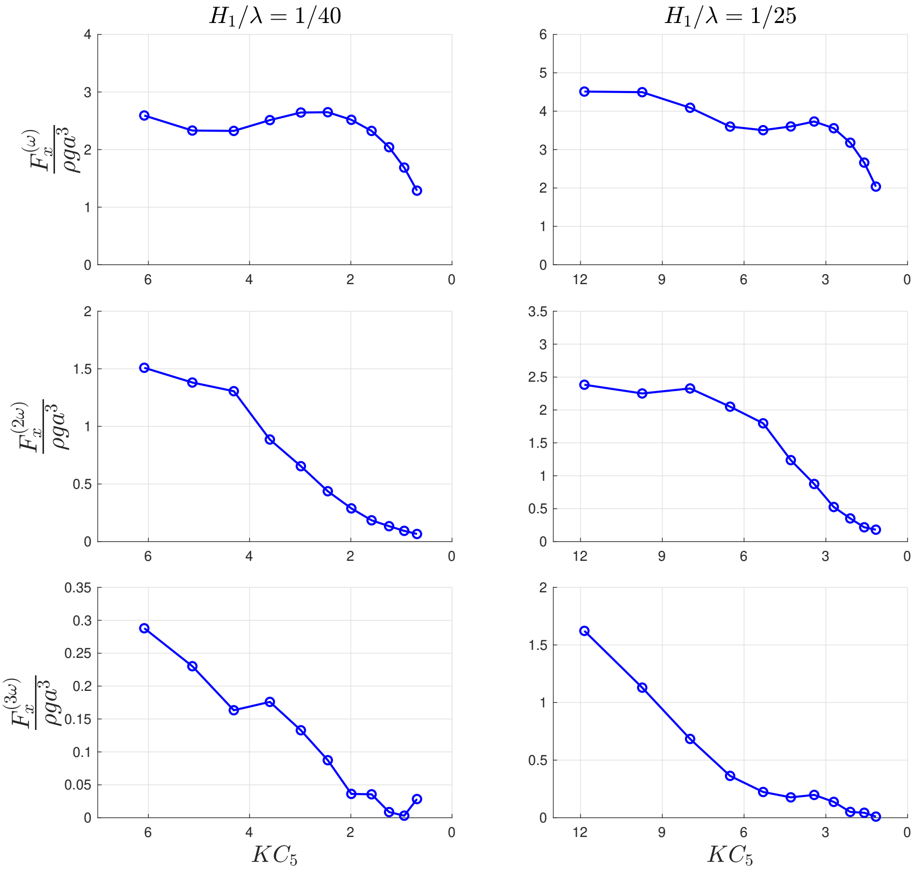

Figure 5.6: Horizontal force amplitude of the first three harmonics for $H_1/\lambda = 1/40$ and $H_1/\lambda = 1/25$ versus KC_5 at water depth $h/a = 7.83$ from 3D CFD-FNV load model.

For $H_1/\lambda = 1/40$ and $H_1/\lambda = 1/25$ the dip in first load harmonic load occur as early as $KC_5 \simeq 3-4$. The discrepancies in the first harmonic load correlate with an underprediction of the first harmonic for increased KC_5, and the results in Figure 5.6 show compliance in the KC_5 range where this occurs. The second and third harmonic force amplitude increases with KC_5, and the second harmonic force amplitude appears to increase with a lower gradient as $KC_5 > 8$.

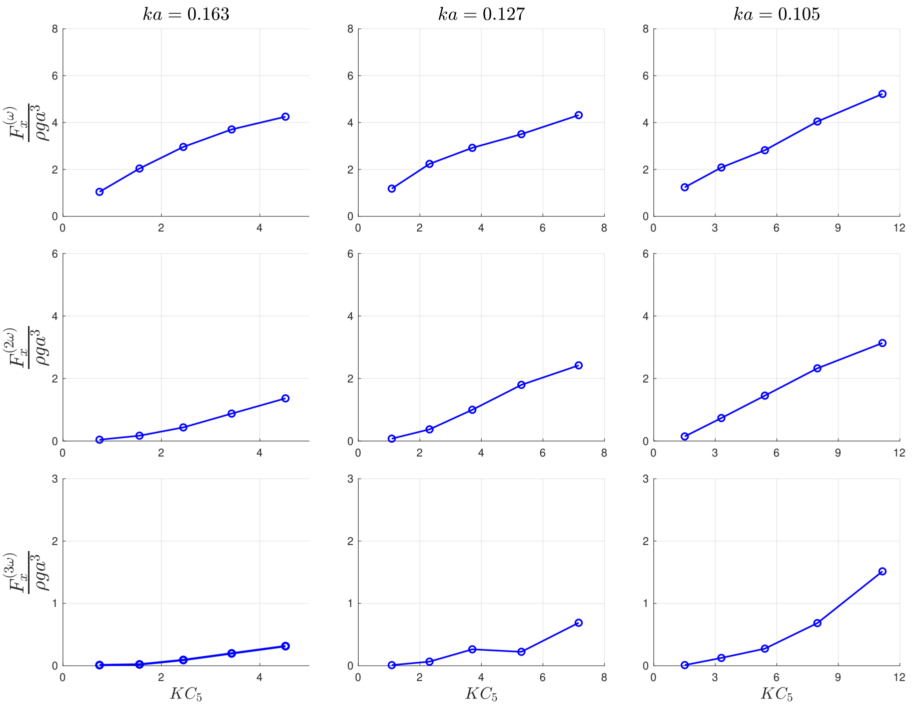

Figure 5.7: Horizontal force amplitude of the first three harmonics for $ka = 0.163$, $ka = 0.127$ and $ka = 0.105$ versus KC_5 at water depth $h/a = 7.83$ from 3D CFD-FNV load model.

The discrepancies seem occur around $KC_5 \simeq 4 - 5$ when plotting the force amplitude as a function of H_1/λ in Figure 5.7. It is also apparant that the gradient in the first harmonic for $ka = 0.163$ and $ka = 0.127$ decreases a at these KC_5 values. The results from these figures confirm that the discrepancies in the load model occur at a KC value about 4-5 and reoccur continuously for $KC > 6$.

The results from this section shows that numerical model used in the 3D CFD-FNV model is unfit to describe higher order wave loads for $KC > 6$. As the viscous forces become increasingly dominant, the discrepancies between the load model amplitude and experimental results increases. It is however evident that the three dimensional added term do not explain the discrepancies in the theoretical and experimental amplitude, as the predicted force with and without the three dimensional term are close to identical.

5.3 Contribution from three dimensional term in the third harmonic load

As discussed in Section 5.2, the three dimensional term does not contribute to the estimated force amplitude for the first three load harmonics. In this section, the contribution from three dimensional term in the 3D CFD-FNV load model will be assessed closer. Time series of the total and first three harmonics the force components for all test conditions from the 3D CFD-FNV load model are provided in Appendix B.2, where F^{CFD} is the first viscous term in Equation (4.18) from CFD, F^{w} the second three dimensional term and F^{FNV} the remaining two terms that are computed from existing FNV theory. The amplitude of the first three load harmonics of the contribution from the three dimensional term in the 3D CFD-FNV load model are plotted separately in Figure 5.8.

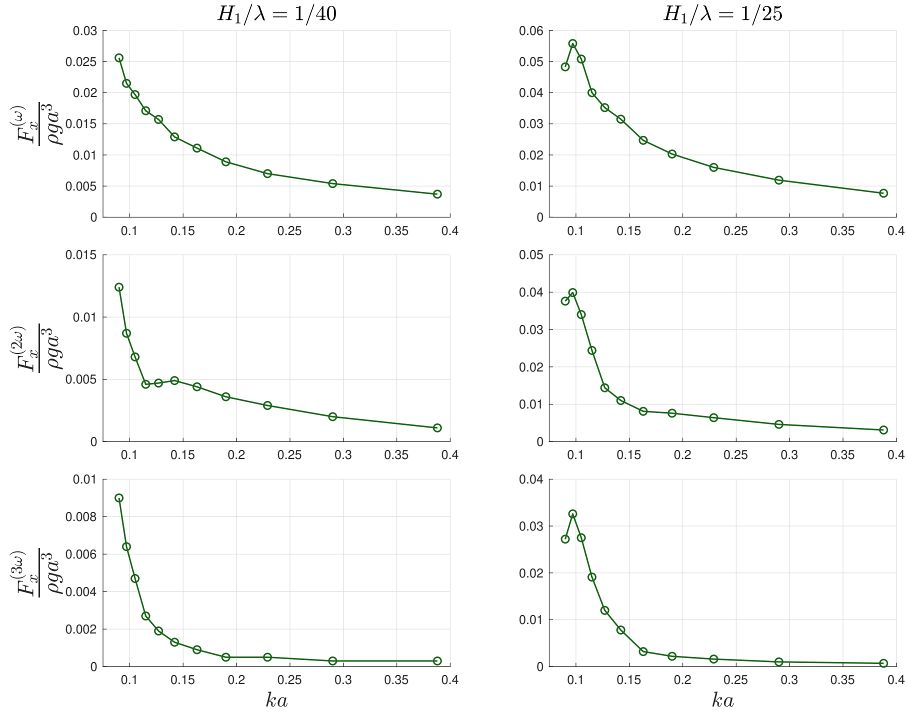

Figure 5.8: The first three harmonics of three dimensional force F^{w} component amplitude for $H_1/\lambda = 1/40$ and $H_1/\lambda = 1/25$ at water dpeth $h/a = 7.83$ from 3D CFD-FNV load model.

It is evident that the three dimensional force contribution increases for longer and steeper waves. The third harmonic force component amplitude increases significantly for both $H_1/\lambda = 1/40$ and $H_1/\lambda = 1/25$ as $ka > 0.163$. As observed by Kristiansen and Faltinsen (2017), locally high pressure caused upwelling at the rear end of the monopile caused a local steep wave propagating in the opposite direction of the incident waves. It is apparent that the three dimensional effects are increasingly significant as the waves get steeper and longer, though the amplitude is still small. Since the motivation for adding a three dimensional term to the CFD-FNV load model is to see how it contributes to the total third harmonic load for low ka numbers, the force components for $ka = 0.163$, $ka = 0.127$ and $ka = 0.105$ are examined closer in Figure 5.9. The flow regimes at these wave conditions are additionally visualized in Appendix B.1.

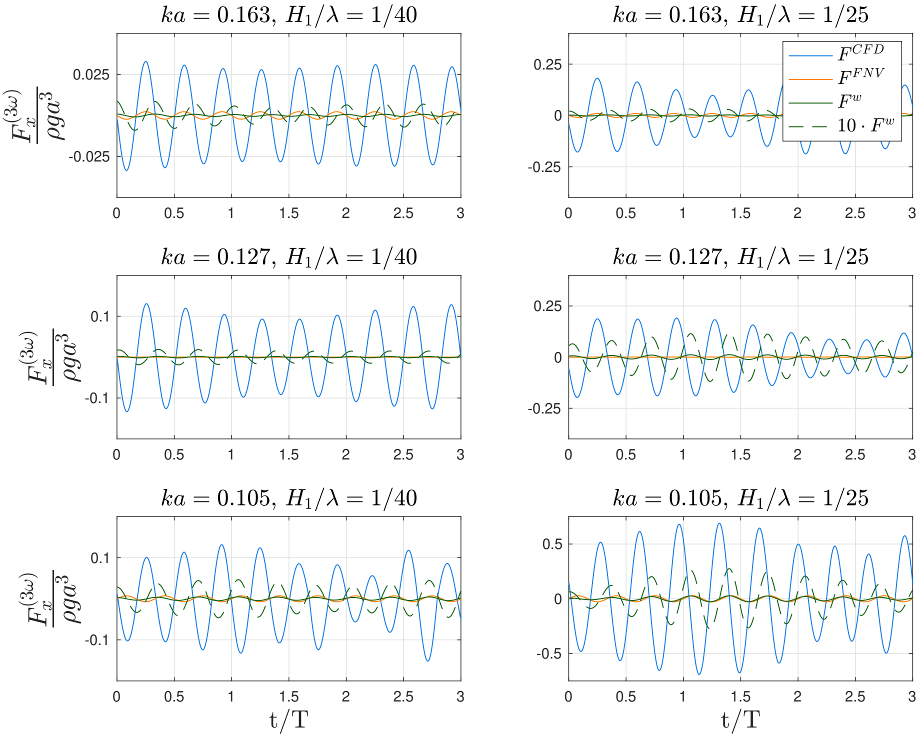

Figure 5.9: Time series of third harmonic of force components from 3D CFD-FNV method for $ka = 0.163$, $ka = 0.127$ and $ka = 0.105$ at water depth $h/a = 7.83$.

The time series in Figure 5.9 show that the contribution from the three dimensional force is small compared to the contribution from the CFD force. The CFD force account for the viscous effects in the flow. However, the third harmonic of the three dimensional force is of out of phase with the CFD force, which means that it does contribute to a small reduction of the total third harmonic load. The observed run-up in the experiments by Kristiansen and Faltinsen (2017) resulted in a local steep wave propagating in negative x-direction for the duration of $\frac{1}{4}T$ to $\frac{1}{3}T$, and it is possible that the out of phase three dimensional third harmonic force is related to this observation.

As the convergence studies and the prediction of the first harmonic load amplitude in Figure 5.4 show, the numerical model has trouble modelling flows at $KC > 6$, i.e steep waves at $ka > 0.127$. This may affect the assessment of the three dimensional term, as the third harmonic CFD force does not have a constant amplitude for low ka numbers. To eliminate this as a possible source of error, the three dimensional term is added to the theoretical FNV force in Equation (2.50). The results for $ka = 0.163$, $ka = 0.127$ and $ka = 0.105$ are given in Figure 5.10.

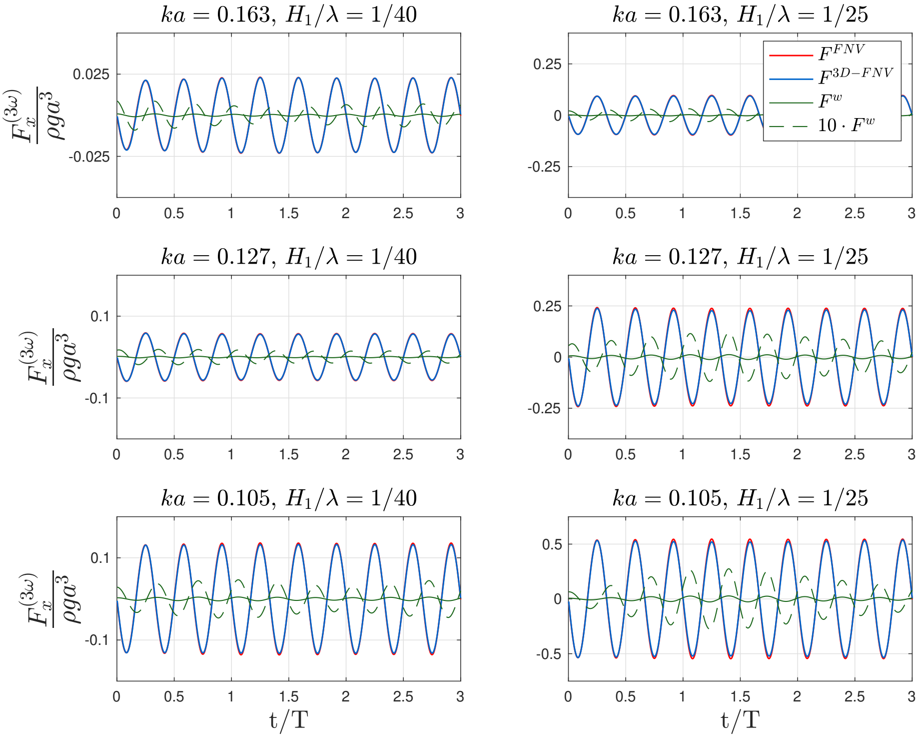

Figure 5.10: Time series of third harmonic of horizontal force from FNV method and three dimensional force component for $ka = 0.163$, $ka = 0.127$ and $ka = 0.105$ at water depth $h/a = 7.83$.

Here, F^{3D-FNV} accounts for the theoretical force with the added three dimensional term, and F^{FNV} is the theoretical force without the three dimensional term. As seen in Figure 5.9, the three dimensional force is out of phase with the theoretical FNV force as well. The amplitude of F^{3D-FNV} is somewhat lower than F^{FNV} for $ka = 0.127$ and $ka = 0.105$, and it appears that the three dimensional force term affects the amplitude at steeper waves. The contribution is though very small.

In order to assess the significance of the contribution from the three dimensional term, the amplitude of the three dimensional force component is divided by the total horizontal force. This is given in Figure 5.11.

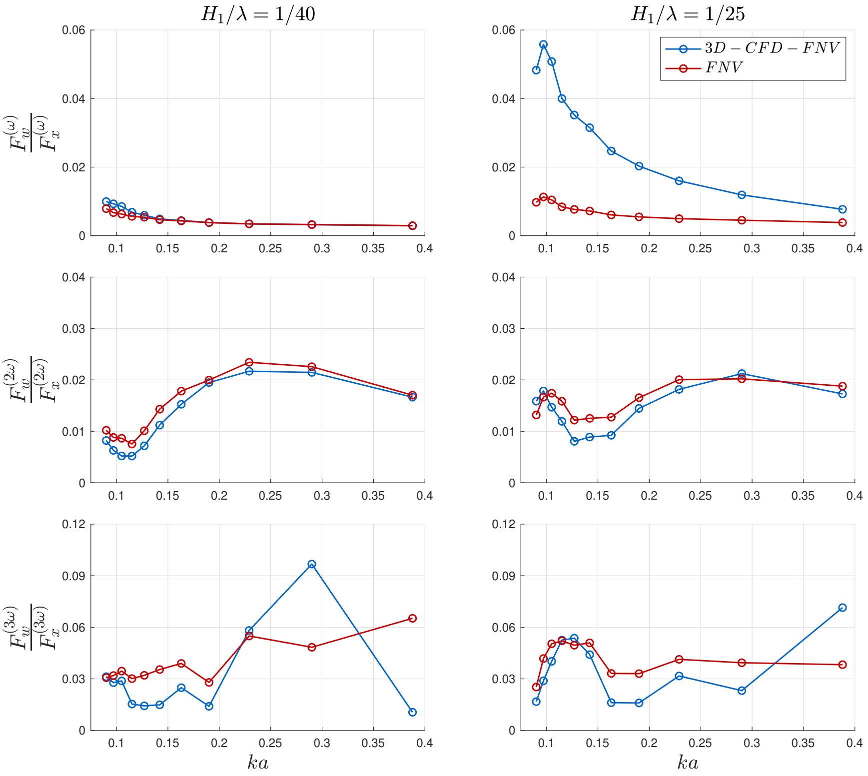

Figure 5.11: Fraction of the first three harmonics of three dimensional force F_w component amplitude to total horizontal force amplitude F_x for $H_1/\lambda = 1/40$ and $H_1/\lambda = 1/25$ at water depth $h/a = 7.83$ from 3D CFD-FNV load model. Legend entries $3D - CFD - FNV$ and FNV denotes the total horizontal force amplitude from 3D CFD-FNV and FNV method respectively.

The amplitude of first harmonic of the three dimensional force is relatively constant but somewhat increased for the longest waves. The contribution is higher compared to the 3D CFD-FNV amplitude since the first harmonic load is underpredicted by the numerical model. The amplitude of the second harmonic decreases gradually as the waves get longer but get higher for the longest waves. The amplitude of the third harmonic of the three dimensional force amplitude is largest relative to the the total horizontal force amplitude is for the longest waves at $H_1/\lambda = 1/25$. This is consistent with the theoretical force amplitude as well, and indicates that the three dimensional contribution is of some significance in this range. The highest $F_w^{(3\omega)}/F_x^{(3\omega)}$ ratio is approximately 5-6%, and as discussed in Section 5.2 the contribution does not affect the third harmonic force amplitude to the degree that it can explain the discrepancies between the experimental and theoretical results.

The results from this section indicate that the added slender body term in the 3D CFD-FNV model does not account for the observed discrepancies between theoretical and experimental results for long and steep waves. The slender body term accounting for three dimensional effects in vertical flow direction is out of phase with the dominant viscous forces from CFD simulations, indicating that three dimensional forces contribute to reducing the total horizontal force. The three dimensional forces are of highest significance for severe wave conditions at low ka number of high steepness, which means that the exclusion of three dimensional effects in existing generalized FNV theory could explain the discrepancies in these wave conditions.

5.4 Further work

Time series of the three dimensional force show that it is out of phase with the viscous force contribution, indicating that three dimensional effects reduce the amplitude of the total force. The three dimensional contribution of of highest significance for the most severe wave conditions with steeper and longer waves. As discussed above, the slender body terms added to the CFD-FNV load model do likely not account for the total three dimensional contribution. In order to examine the discrepancies between theory and experiments for longer and steeper waves in further work, it is recommended to consider other three dimensional effects on the monopile. The 3D CFD-FNV load model accounts for only two dimensional vortex shedding in the xy-plane, and it is possible that induced vortex shedding in the yz-plane contributes to the three dimensional force as well.

During the experiments by Kristiansen and Faltinsen (2017), the flow on the surface was attempted visualized using confetti as shown in Figure 5.12.

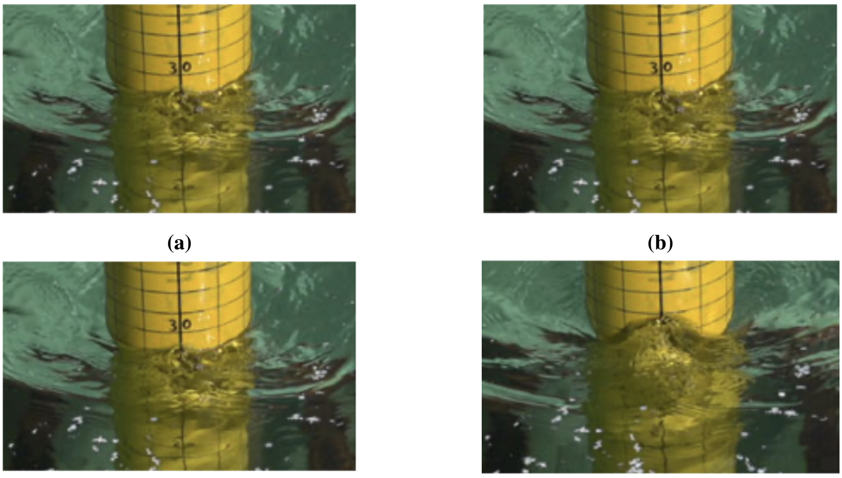

(a) **(b)**

(c) **(d)**

Figure 5.12: Snapshots from high speed video from experiments by Kristiansen and Faltinsen (2017) for $ka = 0.127$ and $H_1/\lambda = 1/25$ at water depth $h/a = 7.83$ illustrating local run-up at rear end of the cylinder. Time instants are approximately $T/120$ apart, where T is the ave period. *Pictures retrieved from Kristiansen and Faltinsen (2017)*

A local rear run-up extending a distance of same order as the monopile diameter was observed during the experiments. This is referred to as upwelling, and caused the confetti on the free surface to move away from the rear end of the monopile, without returning. Kristiansen and Faltinsen (2017) stated that it was clear that this occurred due to an upwelling from below, and that the cause for the upwelling was a high pressure forming under the free surface due to flow separation. It is therefore of interest to study the three dimensional vortex shedding perpendicular to the wave propagation direction, as the induced velocity by the vortices could possibly explain the fluid motion in the local rear run-up.

The use of CFD to simulate oscillating flow around circular object is a challenging. As seen in the convergence studies by the numerical model, the viscous forces are hard to predict accurately as the KC number increases. Comparisons with Sæter (2019) show that a turbulence model may be necessary in order to accurately model the near wall treatment of the flow. The use of three dimensional CFD simulations for similar test conditions will likely require high computational costs compared to present two dimensional CFD simulations. However, it may be necessary to convert to three dimensional flow modelling in order to accurately describe the fluid motion in z-direction.

The motivation for developing the 3D CFD-FNV load model was to find an efficient and accurate model for higher order wave loads. As discussed, the accuracy of the numerical model is uncertain for $KC > 6$, which means that the application range of the method is limited. The two dimensional CFD simulations in OpenFOAM are run at relatively low computational cost due to grid refinement and use of adjustable time step. Post processing of the results are however greatly time consuming due to the size of the data. Since the velocity data was sampled at 100 probes for 160 probelines at 11 planes for eight wave periods, the data used to integrate the three dimensional force was of significant size. In total, nearly 1 TB of storage was used to obtain the results from the 3D CFD-FNV load model. If the method was to be developed further, the possibility of reducing the number of probe locations should be considered in order to save time reading the probe velocity data from OpenFOAM.

Chapter 6

Conclusion

In this thesis a combined 3D CFD-FNV load model has been developed. Two dimensional CFD simulations in OpenFOAM have been performed based on strip theory, replacing the terms in existing FNV theory proportional to $\frac{\partial u}{\partial t}$. The remaining terms from FNV theory were computed analytically, and a slender body term accounting for three dimensional effects on the monopile was added. A comparison of the results from the 3D CFD-FNV load model with experimental results showed that the numerical model had difficulties representing flows at $KC > 5 - 6$, and underpredicts the total and first load harmonic as KC increased above this range. The three dimensional force contribution implemented in the 3D CFD-FNV load model was investigated, and results showed that the contribution was very small to negligible. The contribution was however observed to be out of phase and of highest contribution for longer and steeper waves, indicating that the discrepancies between theoretical and experimental results may be due to similar three dimensional effects. Further work should include a further investigation of the three dimensional effects for severe sea states, with focus on the local upwelling on the free surface on the rear end of the monopile. An implementation of the three dimensional vortex shedding in the yz-plane along with strip theory based CFD simulations and FNV theory has the potential of capturing the effects that are not adequately described by the 3D CFD-FNV load model.

Bibliography

Courant, R., Friedrichs, K., Lewy, H., 1928. On the partial difference equations of mathematical physics. Technical Report.

Dean, R.G., Dalrymple, R.A., 1991. Water wave mechanics for engineers and scientists. Advanced Series on Ocean Engineering - Volume 2, World Scientific Publishing Co Pte Ltd.

Faltinsen, O.M., 1990. Sea loads on ships and offshore structures. Cambridge Ocean Technology Series, Cambridge University Press.

Faltinsen, O.M., 1999. Ringing loads on a slender vertical cylinder of general cross-section. Journal of Engineering Mathematics 35, 199–217.

Faltinsen, O.M., Newman, J.N., Vinje, T., 1995. Nonlinear wave loads on a slender vertical cylinder. Journal of Fluid Mechanics 289, 179–198.

Fenton, J., 1985. A fifth order stokes theory for steady waves. Journal of waterways, port, coastal and ocean engineering 9, 3–25.

Fimland, D.H., 2018. Nonlinear Wave Loads on a Vertical Cylinder. Master's thesis. Norwegian University of Science and Technology, Department of Marine Technology.

Grue, J., Bjørnshol, G., Strand, Ø., 1994. Nonlinear wave loads which may generate ringing responses on offshore structures. 9th International Workshop on Water Waves and Floating Bodies, Kyushu, Japan Research Institute for Applied Mechanics, Kyushu University.

Hedges, T., 1995. Regions of validity of analytical wave theories. Proceedings of The Ice - Water Maritime and Energy 112, 111–114.

Hoegh-Guldberg, O., Jacob, D., Taylor, M., Bindi, M., Brown, S., Camilloni, I., Diedhiou, A., Djalante, R., Ebi, K., Engelbrecht, F., Guiot, J., Hijioka, Y., Mehrotra, S., Payne, A., Seneviratne, S., Thomas, A., Warren, R., Zhou, G., Tschakert, P., 2018. Impacts of 1.5°C global warming on natural and human systems. IPCC.

Hoekstra, A.Y., Wiedmann, T.O., 2014. Humanity's unsustainable environmental footprint. Science 344, 1114–1117.

IRENA, 2019a. Future of wind: Deployment, investment, technology, grid integration and socio-economic aspects (A Global Energy Transformation paper). Technical Report. Abu Dhabi. URL: `https://www.irena.org/publications/2019/Oct/Future-of-wind`.

IRENA, 2019b. Global energy transformation: A roadmap to 2050. Technical Report. Abu Dhabi. URL: `https://www.irena.org/publications/2019/Apr/Global-energy-transformation-A-roadmap-to-2050-2019Edition`.

IRENA, 2019c. Renewable capacity statistics 2019. Technical Report. Abu Dhabi. URL: `https://www.irena.org/publications/2019/Mar/Renewable-Capacity-Statistics-2019`.

Jefferys, E.R., Rainey, R.C.T., 1994. Slender body models of tlp and gbs 'ringing'. Proc. 7th International Conference on the Behaviour of Offshore Structures, MIT, Cambridge 2, 587–606.

Kallehave1, D., Byrne, B.W., Thilstedan, C.L., Mikkelsen, K.K., 2015. Optimization of monopiles for offshore wind turbines. Phil. Trans. R. Soc. A 373.

Kristiansen, T., Faltinsen, O.M., 2017. Higher harmonic wave loads on a vertical cylinder in finite water depth. J. Fluid Mech. 833, 773–805.

Liu, Y., Xue, M., Yue, D.K.P., 2001. Computations of fully nonlinear three-dimensional wave–wave and wave–body interactions. part 2. nonlinear waves and forces on a body. J. Fluid Mech 438, 41–66.

Mentzoni, F., Abrahamsen-Prsic, M., Kristiansen, T., 2018. Hydrodynamic coefficients of simplified subsea structures. Proceedings of the ASME 2018 37th International Conference on Ocean, Offshore and Arctic Engineering .

Morison, J.R., O'Brien, M.P., Johnson, J.W., Schaaf, S.A., 1950. The force exerted by surface waves on piles. Pet. Trans 189, 149–154.

Morthorst, P., Kitzing, L., 2016. Economics of building and operating offshore wind farms, in: Ng, C., Ran, L. (Eds.), Offshore Wind Farms. Woodhead Publishing, pp. 9 – 27.

Natvig, B.J., Teigen, P., 1993. Review of hydrodynamic challenges in tlp design. International Journal of Offshore and Polar Engineering 3(04).

Patel, M.H., 1989. Dynamics of Offshore Structures. Butterworth.

Paulsen, B.T., Bredmose, H., Bingham, H.B., Jacobsen, N.G., 2014. Forcing of a bottom-mounted circular cylinder by steep water waves at finite depth. J. Fluid Mech 755, 1–34.

Russel, J., Cohn, R., 2012. OpenFOAM. LENNEX Corp.

Sarpkaya, T., 1976. Vortex shedding and resistance in harmonic flow about smooth and rough circular cylinders at high Renyolds numbers. Technical Report. Monterey, California.

Skjelbreia, L., Hendrickson, J., 1960. Fifth order gravity wave theory. Proceedings 7th conference of coastal engineering , 184–196.

Stokes, G.G., 1847. On the theory of oscillatory waves. Camb. Trans. 8, 197–229.

Suja-Thauvin, L., Eliassen, L., Krokstad, J., 2014. The scalability of loads on large diameter monopile offshore wind support structures. International Wind Engineering Conference .

Sæter, T., 2019. Ringing Loads on Offshore Wind Turbine Monopiles. Master's thesis. Norwegian University of Science and Technology, Department of Marine Technology.

UNFCCC, 2015. Paris agreement URL: `https://unfccc.int/resource/docs/2015/cop21/eng/l09r01.pdf`. fCCC/CP/2015/L.9/Rev1. Retrieved 24.02.20.

Ursell, F., 1953. The long-wave paradox in the theory of gravity. Mathematical Proceedings of the Cambridge Philosophical Society 4, 685–694.

Williamson, C.H.K., 1985. Sinusoidal flow relative to circular cylinders. J. Fluid Mech. 155, 141–174.

WindEurope, 2019. Offshore Wind in Europe Key trends and statistics 2019. Technical Report. URL: `https://windeurope.org/about-wind/statistics/offshore/european-offshore-wind-industry-key-trends-statistics-2019/`. retrieved online 22.05.19.

Yen, W., Asako, Y., Che Sidik, N.A., Rui-Zher, G., 2017. Governing equations in computational fluid dynamics: Derivations and a recent review .

Çengel, Y.A., Cimbala, J.M., 2006. Fluid mechanics. 3rd ed., McGraw-Hill Education.

Appendix

Appendix A

A.1 Time series of the total and first three harmonics of the horizontal force on monopile from FNV theory, 3D CFD-FNV load model and CFD-FNV load model

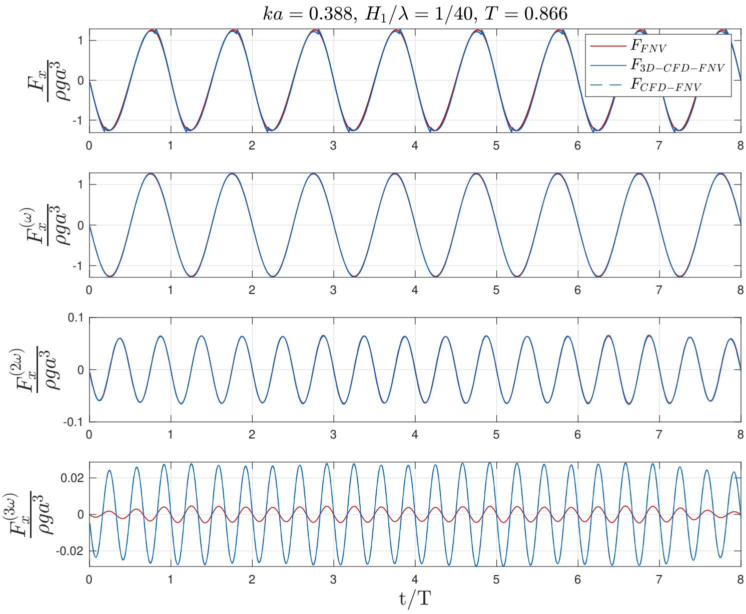

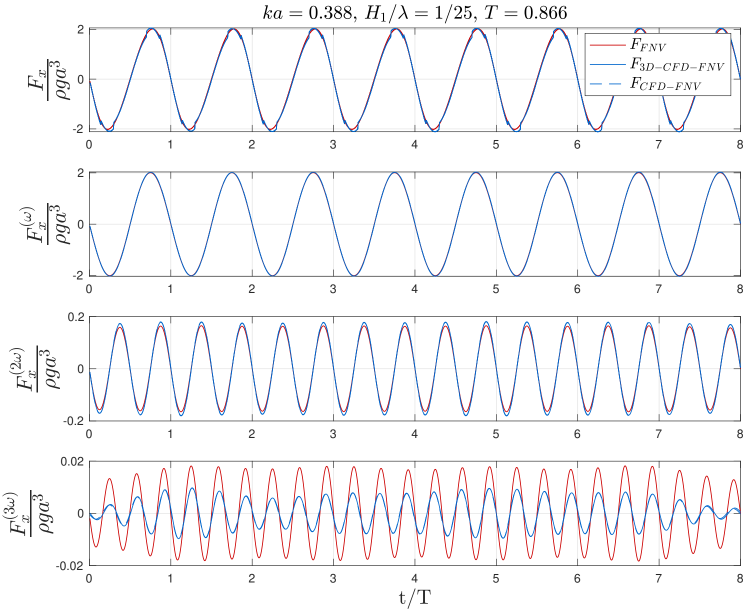
$ka = 0.388,\ H_1/\lambda = 1/25,\ T = 0.866$
$\frac{F_x}{\rho g a^3}$
$\frac{F_x^{(\omega)}}{\rho g a^3}$
$\frac{F_x^{(2\omega)}}{\rho g a^3}$
$\frac{F_x^{(3\omega)}}{\rho g a^3}$
F_{FNV}
$F_{3D-CFD-FNV}$
$F_{CFD-FNV}$
2
0
-2
0.2
-0.2
0.02
-0.02
0 1 2 3 4 5 6 7 8
t/T

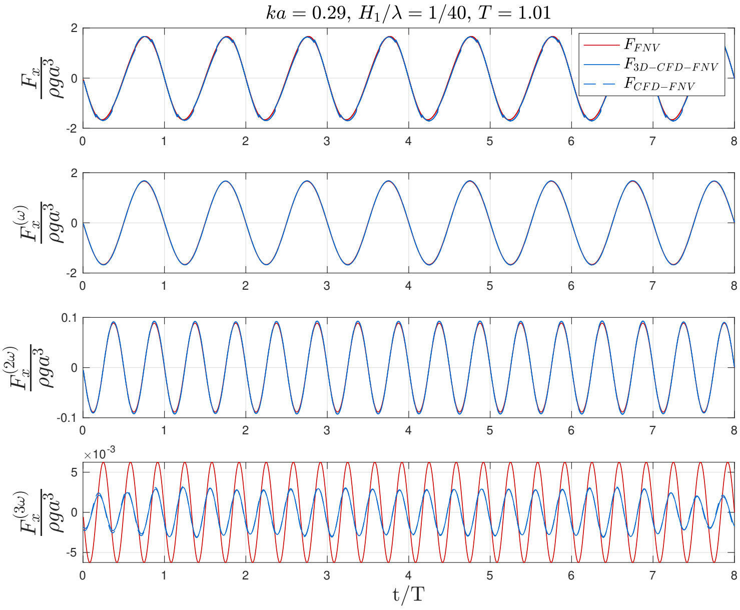
$ka = 0.29,\ H_1/\lambda = 1/40,\ T = 1.01$
$\frac{F_x}{\rho g a^3}$
$\frac{F_x^{(\omega)}}{\rho g a^3}$
$\frac{F_x^{(2\omega)}}{\rho g a^3}$
$\frac{F_x^{(3\omega)}}{\rho g a^3}$
F_{FNV}
$F_{3D-CFD-FNV}$
$F_{CFD-FNV}$
2
0
-2
0.1
-0.1
$\times 10^{-3}$
5
-5
0 1 2 3 4 5 6 7 8
t/T

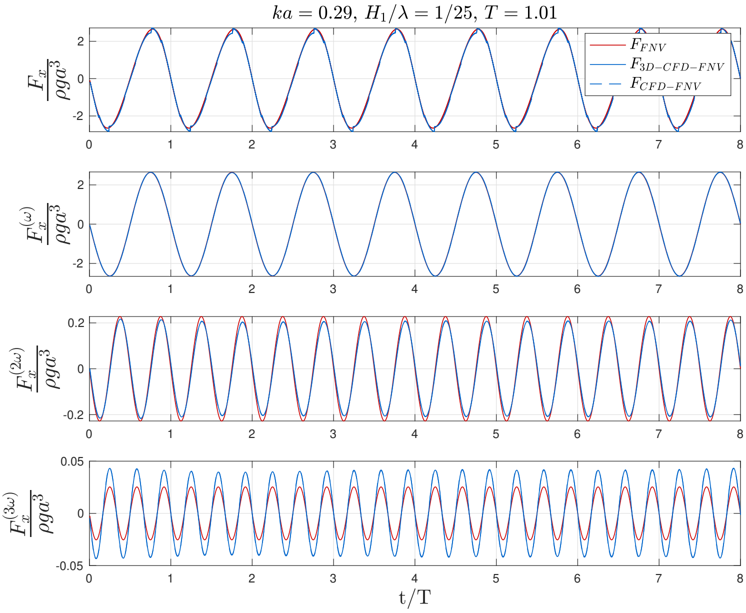
$ka = 0.29,\ H_1/\lambda = 1/25,\ T = 1.01$
$\frac{F_x}{\rho g a^3}$
$\frac{F_x^{(\omega)}}{\rho g a^3}$
$\frac{F_x^{(2\omega)}}{\rho g a^3}$
$\frac{F_x^{(3\omega)}}{\rho g a^3}$
F_{FNV}
$F_{3D-CFD-FNV}$
$F_{CFD-FNV}$
2
0
-2
0.2
-0.2
0.05
-0.05
0 1 2 3 4 5 6 7 8
t/T

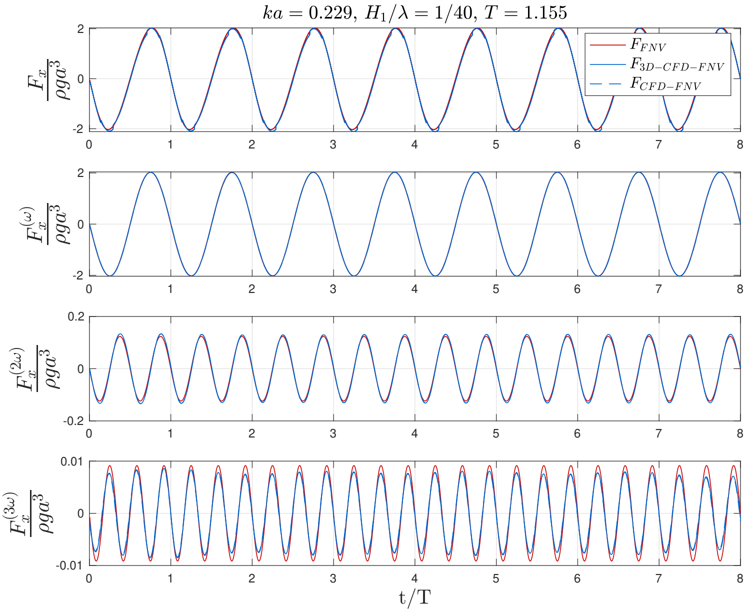
$ka = 0.229,\ H_1/\lambda = 1/40,\ T = 1.155$
$\frac{F_x}{\rho g a^3}$
$\frac{F_x^{(\omega)}}{\rho g a^3}$
$\frac{F_x^{(2\omega)}}{\rho g a^3}$
$\frac{F_x^{(3\omega)}}{\rho g a^3}$
F_{FNV}
$F_{3D-CFD-FNV}$
$F_{CFD-FNV}$
2
0
-2
0.2
-0.2
0.01
-0.01
0 1 2 3 4 5 6 7 8
t/T

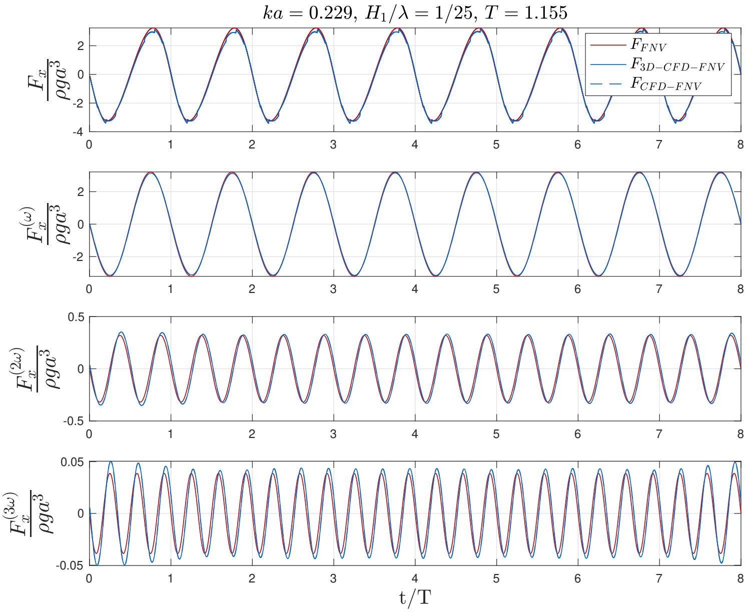
$ka = 0.229,\ H_1/\lambda = 1/25,\ T = 1.155$
$\frac{F_x}{\rho g a^3}$
$\frac{F_x^{(\omega)}}{\rho g a^3}$
$\frac{F_x^{(2\omega)}}{\rho g a^3}$
$\frac{F_x^{(3\omega)}}{\rho g a^3}$
F_{FNV}
$F_{3D-CFD-FNV}$
$F_{CFD-FNV}$
t/T
0
1
2
3
4
5
6
7
8
2
0
-2
-4
0.5
-0.5
0.05
-0.05

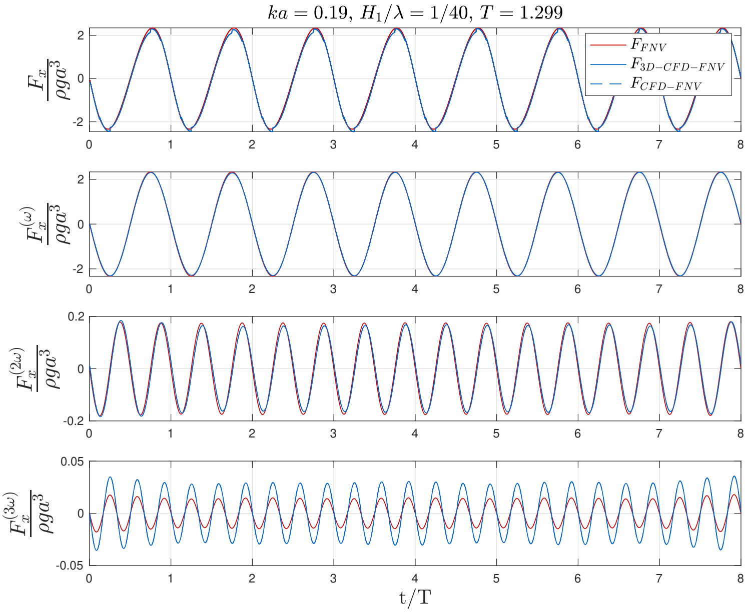
$ka = 0.19,\ H_1/\lambda = 1/40,\ T = 1.299$
$\frac{F_x}{\rho g a^3}$
$\frac{F_x^{(\omega)}}{\rho g a^3}$
$\frac{F_x^{(2\omega)}}{\rho g a^3}$
$\frac{F_x^{(3\omega)}}{\rho g a^3}$
F_{FNV}
$F_{3D-CFD-FNV}$
$F_{CFD-FNV}$
t/T
0
1
2
3
4
5
6
7
8
2
0
-2
0.2
-0.2
0.05
-0.05

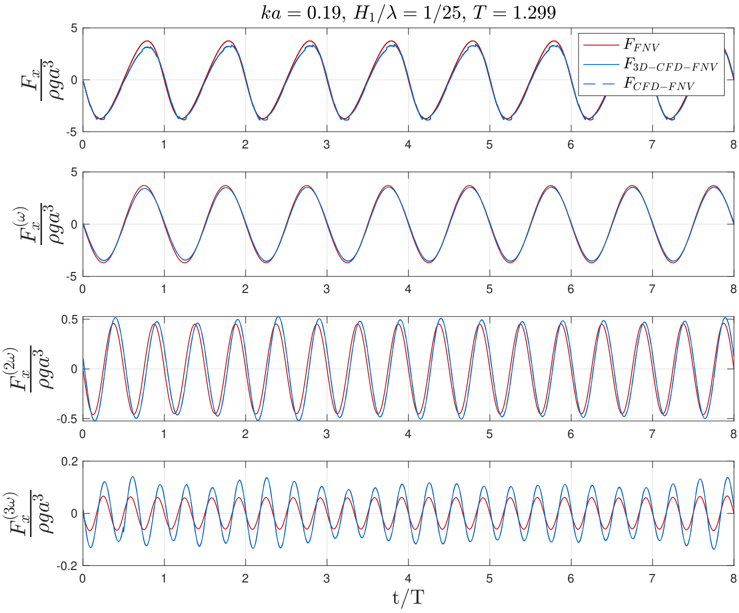
$ka = 0.19,\ H_1/\lambda = 1/25,\ T = 1.299$
F_{FNV}
$F_{3D-CFD-FNV}$
$F_{CFD-FNV}$
$\frac{F_x}{\rho g a^3}$
$\frac{F_x^{(\omega)}}{\rho g a^3}$
$\frac{F_x^{(2\omega)}}{\rho g a^3}$
$\frac{F_x^{(3\omega)}}{\rho g a^3}$
5
0
-5
0.5
-0.5
0.2
-0.2
0
1
2
3
4
5
6
7
8
t/T

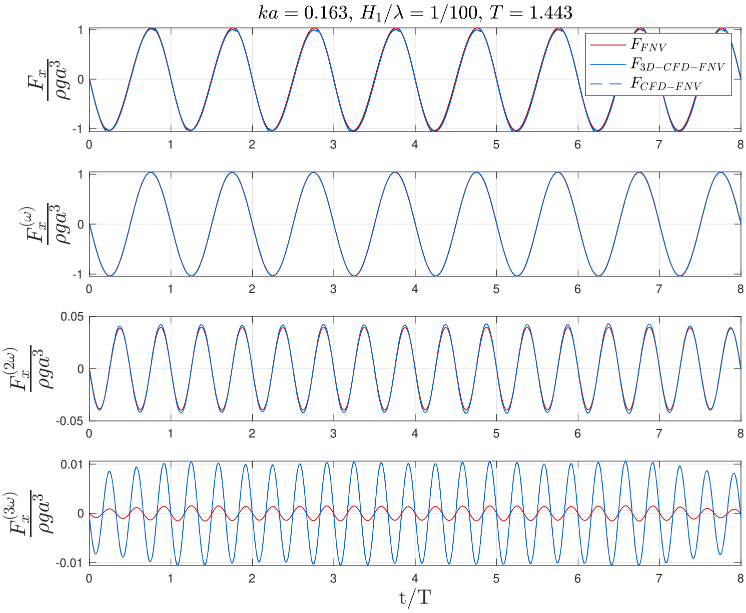
$ka = 0.163,\ H_1/\lambda = 1/100,\ T = 1.443$
F_{FNV}
$F_{3D-CFD-FNV}$
$F_{CFD-FNV}$
$\frac{F_x}{\rho g a^3}$
$\frac{F_x^{(\omega)}}{\rho g a^3}$
$\frac{F_x^{(2\omega)}}{\rho g a^3}$
$\frac{F_x^{(3\omega)}}{\rho g a^3}$
1
0
-1
0.05
-0.05
0.01
-0.01
0
1
2
3
4
5
6
7
8
t/T

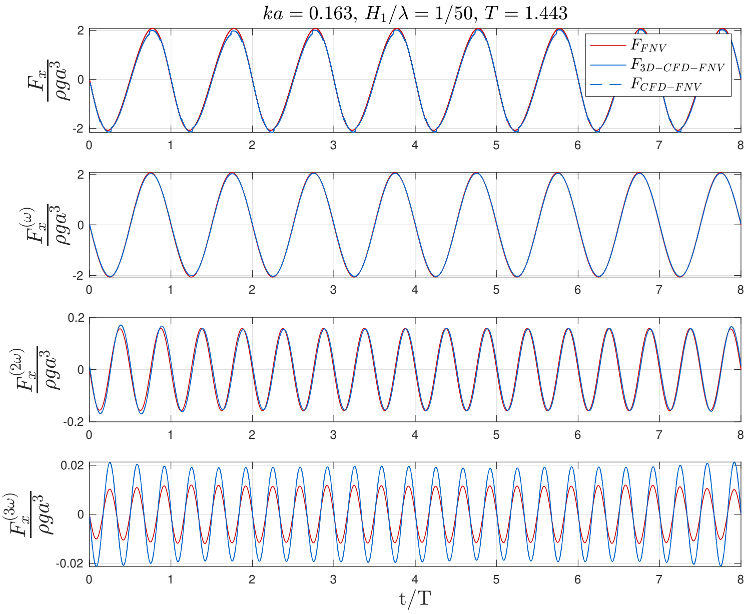
$ka = 0.163,\ H_1/\lambda = 1/50,\ T = 1.443$
$\frac{F_x}{\rho g a^3}$
$\frac{F_x^{(\omega)}}{\rho g a^3}$
$\frac{F_x^{(2\omega)}}{\rho g a^3}$
$\frac{F_x^{(3\omega)}}{\rho g a^3}$
F_{FNV}
$F_{3D-CFD-FNV}$
$F_{CFD-FNV}$
2
0
-2
0.2
-0.2
0.02
-0.02
0 1 2 3 4 5 6 7 8
t/T

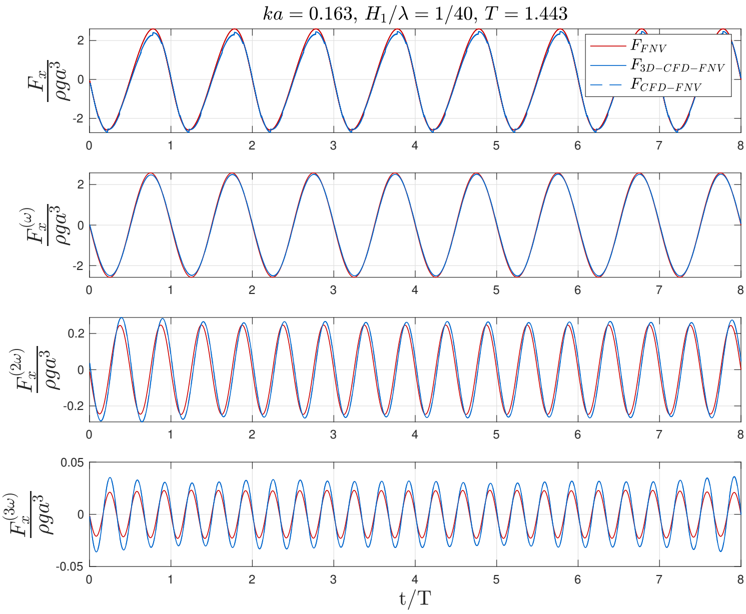
$ka = 0.163,\ H_1/\lambda = 1/40,\ T = 1.443$
$\frac{F_x}{\rho g a^3}$
$\frac{F_x^{(\omega)}}{\rho g a^3}$
$\frac{F_x^{(2\omega)}}{\rho g a^3}$
$\frac{F_x^{(3\omega)}}{\rho g a^3}$
F_{FNV}
$F_{3D-CFD-FNV}$
$F_{CFD-FNV}$
2
0
-2
0.2
-0.2
0.05
-0.05
0 1 2 3 4 5 6 7 8
t/T

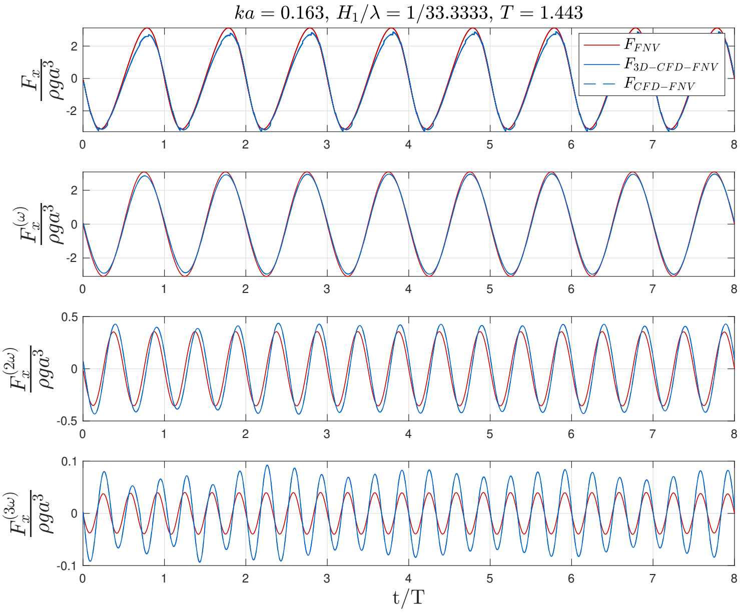
$ka = 0.163,\ H_1/\lambda = 1/33.3333,\ T = 1.443$
$\frac{F_x}{\rho g a^3}$
$\frac{F_x^{(\omega)}}{\rho g a^3}$
$\frac{F_x^{(2\omega)}}{\rho g a^3}$
$\frac{F_x^{(3\omega)}}{\rho g a^3}$
F_{FNV}
$F_{3D-CFD-FNV}$
$F_{CFD-FNV}$
t/T

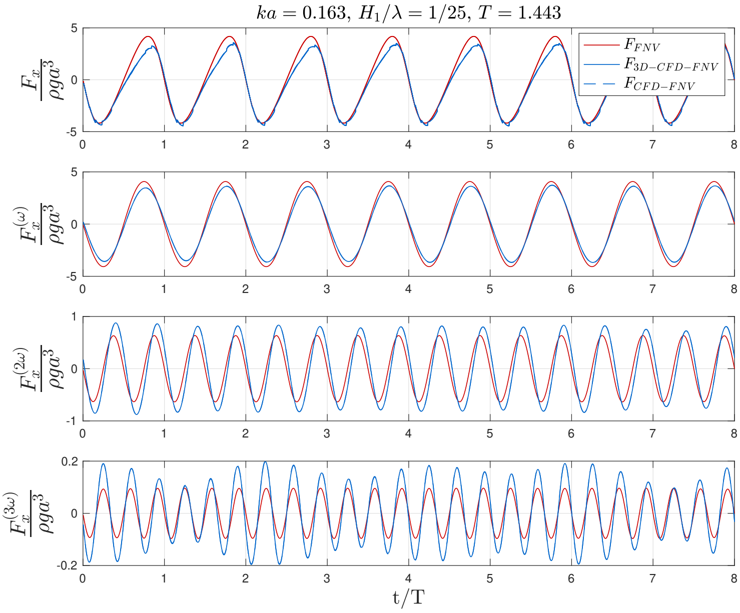
$ka = 0.163,\ H_1/\lambda = 1/25,\ T = 1.443$
$\frac{F_x}{\rho g a^3}$
$\frac{F_x^{(\omega)}}{\rho g a^3}$
$\frac{F_x^{(2\omega)}}{\rho g a^3}$
$\frac{F_x^{(3\omega)}}{\rho g a^3}$
F_{FNV}
$F_{3D-CFD-FNV}$
$F_{CFD-FNV}$
t/T

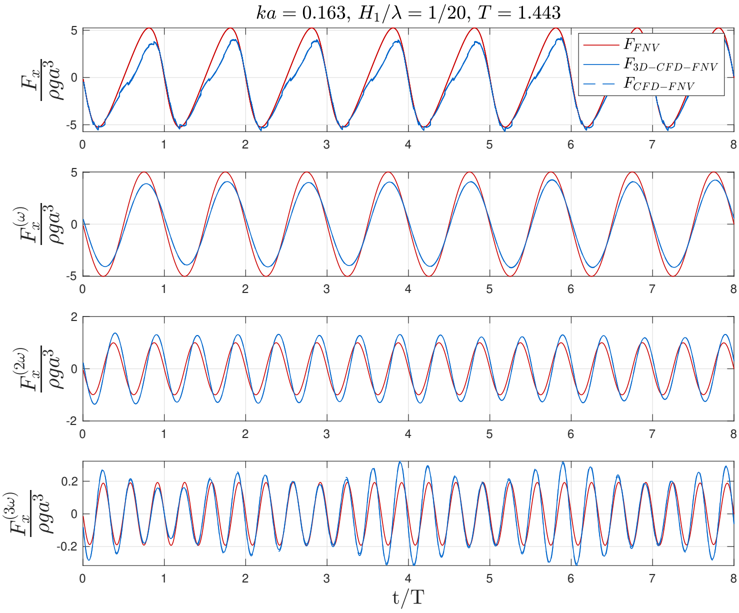
$ka = 0.163,\ H_1/\lambda = 1/20,\ T = 1.443$
$\frac{F_x}{\rho g a^3}$
$\frac{F_x^{(\omega)}}{\rho g a^3}$
$\frac{F_x^{(2\omega)}}{\rho g a^3}$
$\frac{F_x^{(3\omega)}}{\rho g a^3}$
F_{FNV}
$F_{3D-CFD-FNV}$
$F_{CFD-FNV}$
5
0
-5
2
-2
0.2
-0.2
0
1
2
3
4
5
6
7
8
t/T

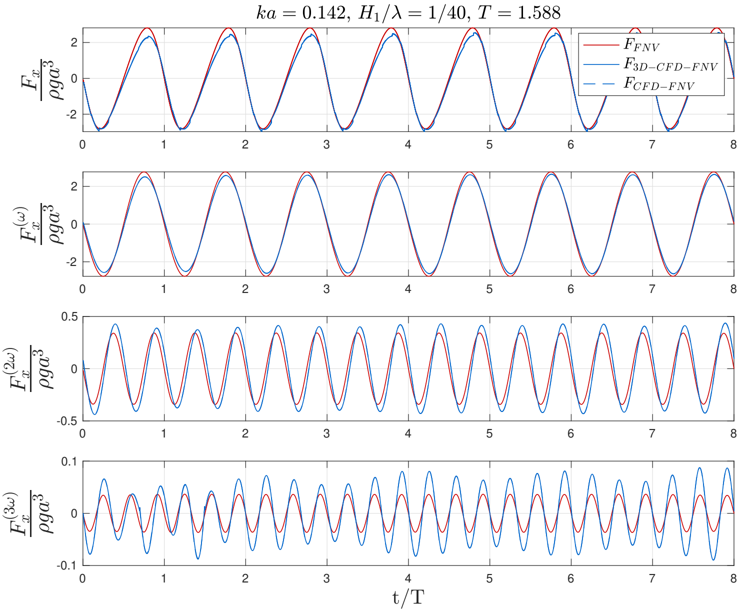
$ka = 0.142,\ H_1/\lambda = 1/40,\ T = 1.588$
$\frac{F_x}{\rho g a^3}$
$\frac{F_x^{(\omega)}}{\rho g a^3}$
$\frac{F_x^{(2\omega)}}{\rho g a^3}$
$\frac{F_x^{(3\omega)}}{\rho g a^3}$
F_{FNV}
$F_{3D-CFD-FNV}$
$F_{CFD-FNV}$
2
0
-2
0.5
-0.5
0.1
-0.1
0
1
2
3
4
5
6
7
8
t/T

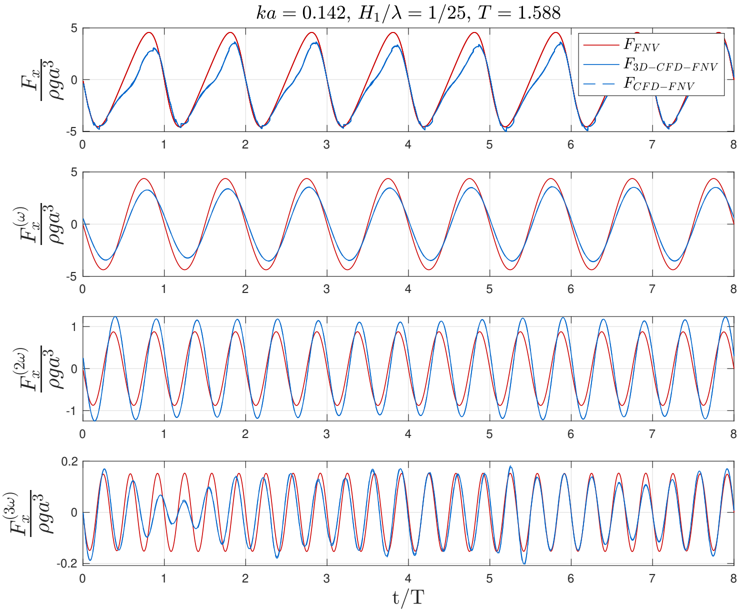
$ka = 0.142,\ H_1/\lambda = 1/25,\ T = 1.588$

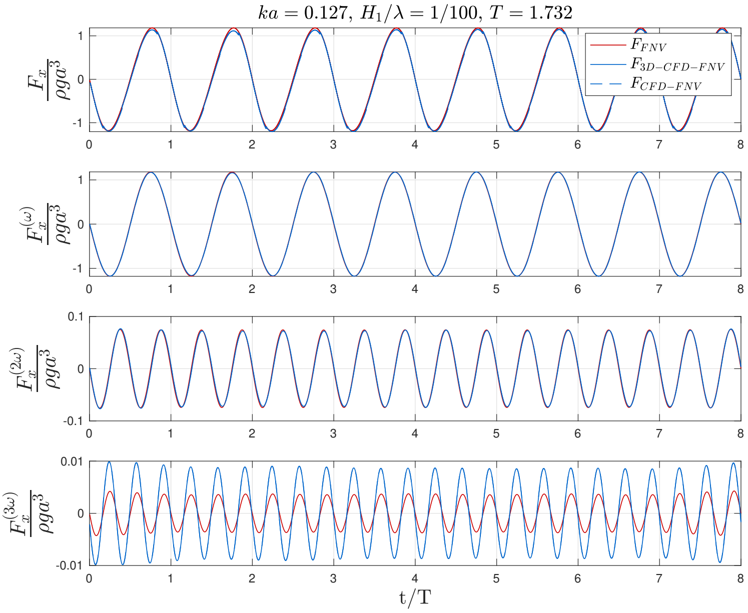
$ka = 0.127,\ H_1/\lambda = 1/100,\ T = 1.732$

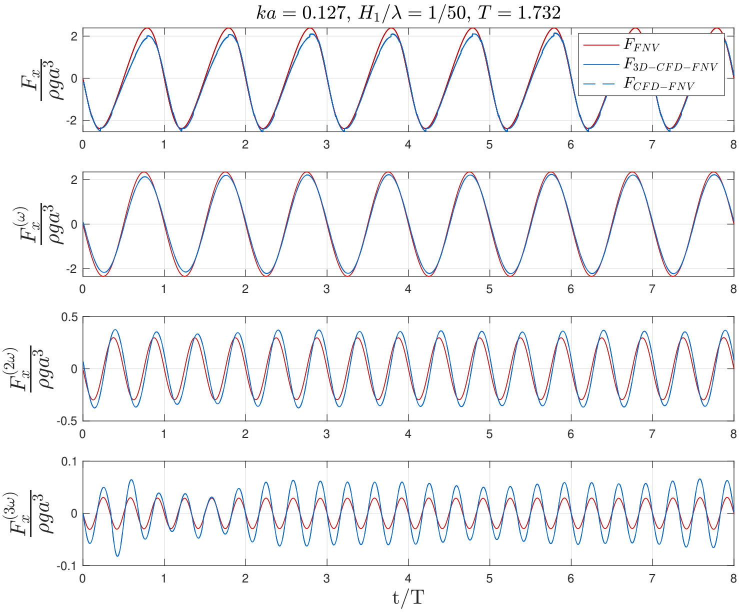
$ka = 0.127,\ H_1/\lambda = 1/50,\ T = 1.732$
$\frac{F_x}{\rho g a^3}$
$\frac{F_x^{(\omega)}}{\rho g a^3}$
$\frac{F_x^{(2\omega)}}{\rho g a^3}$
$\frac{F_x^{(3\omega)}}{\rho g a^3}$
F_{FNV}
$F_{3D-CFD-FNV}$
$F_{CFD-FNV}$
2
0
-2
0.5
-0.5
0.1
-0.1
0
1
2
3
4
5
6
7
8
t/T

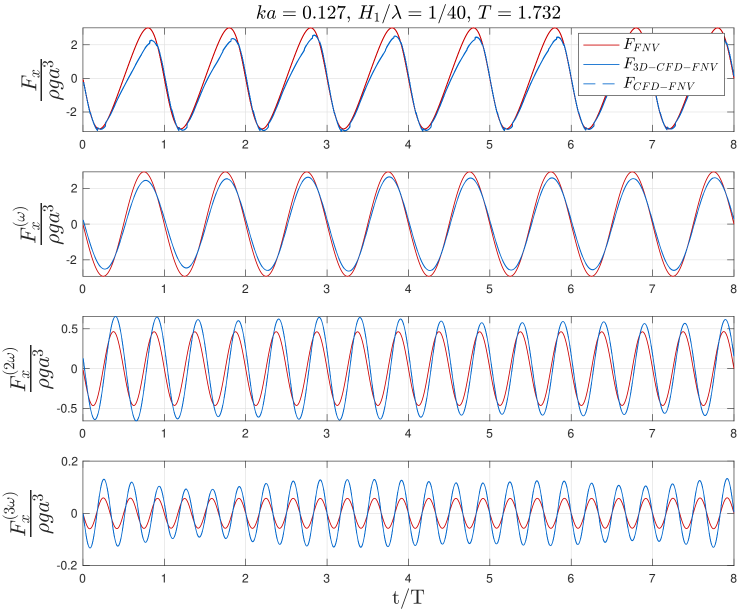
$ka = 0.127,\ H_1/\lambda = 1/40,\ T = 1.732$
$\frac{F_x}{\rho g a^3}$
$\frac{F_x^{(\omega)}}{\rho g a^3}$
$\frac{F_x^{(2\omega)}}{\rho g a^3}$
$\frac{F_x^{(3\omega)}}{\rho g a^3}$
F_{FNV}
$F_{3D-CFD-FNV}$
$F_{CFD-FNV}$
2
0
-2
0.5
-0.5
0.2
-0.2
0
1
2
3
4
5
6
7
8
t/T

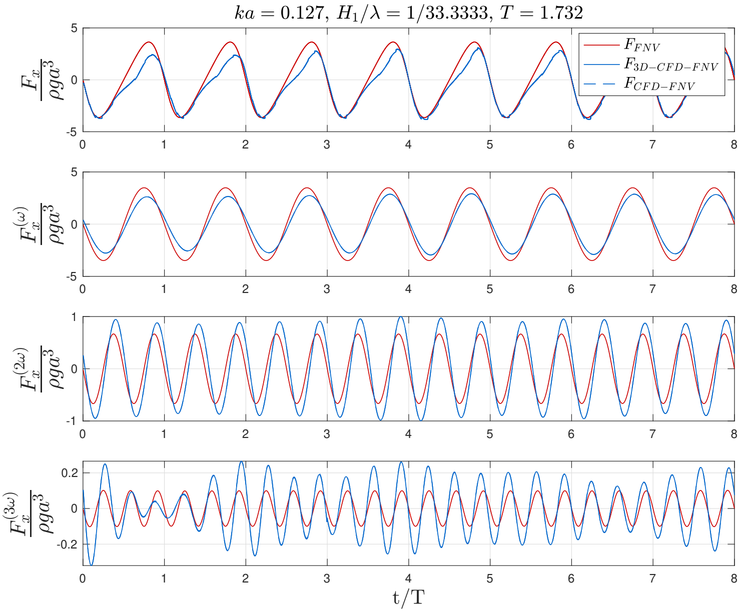
$ka = 0.127,\ H_1/\lambda = 1/33.3333,\ T = 1.732$
$\frac{F_x}{\rho g a^3}$
$\frac{F_x^{(\omega)}}{\rho g a^3}$
$\frac{F_x^{(2\omega)}}{\rho g a^3}$
$\frac{F_x^{(3\omega)}}{\rho g a^3}$
F_{FNV}
$F_{3D-CFD-FNV}$
$F_{CFD-FNV}$
5
0
-5
1
-1
0.2
-0.2
0
1
2
3
4
5
6
7
8
t/T

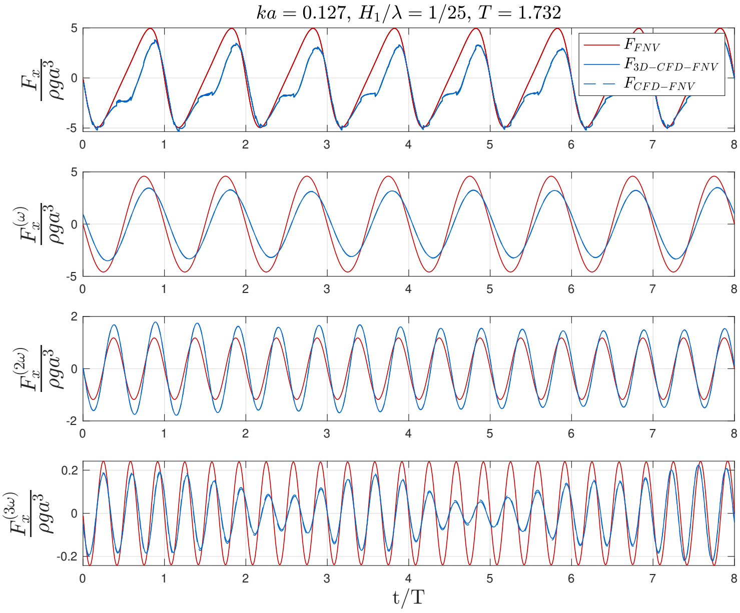
$ka = 0.127,\ H_1/\lambda = 1/25,\ T = 1.732$
$\frac{F_x}{\rho g a^3}$
$\frac{F_x^{(\omega)}}{\rho g a^3}$
$\frac{F_x^{(2\omega)}}{\rho g a^3}$
$\frac{F_x^{(3\omega)}}{\rho g a^3}$
F_{FNV}
$F_{3D-CFD-FNV}$
$F_{CFD-FNV}$
5
0
-5
2
-2
0.2
-0.2
0
1
2
3
4
5
6
7
8
t/T

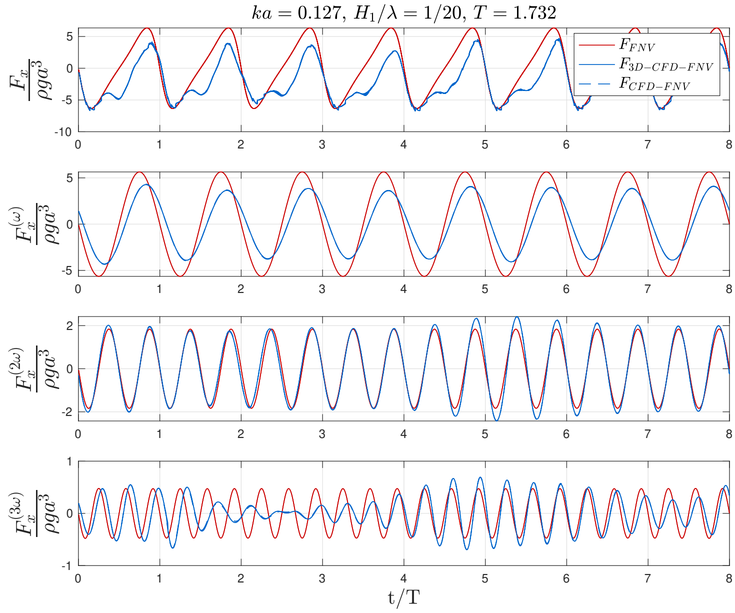

$ka = 0.127,\ H_1/\lambda = 1/20,\ T = 1.732$

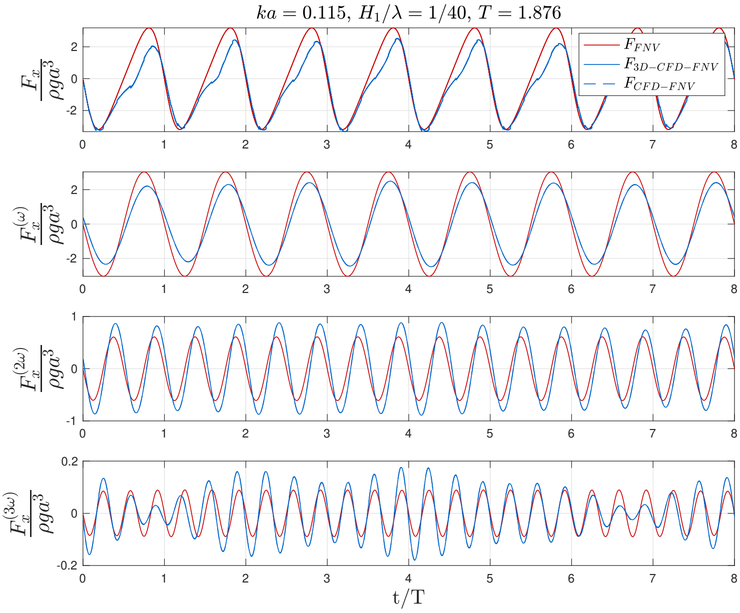

$ka = 0.115,\ H_1/\lambda = 1/40,\ T = 1.876$

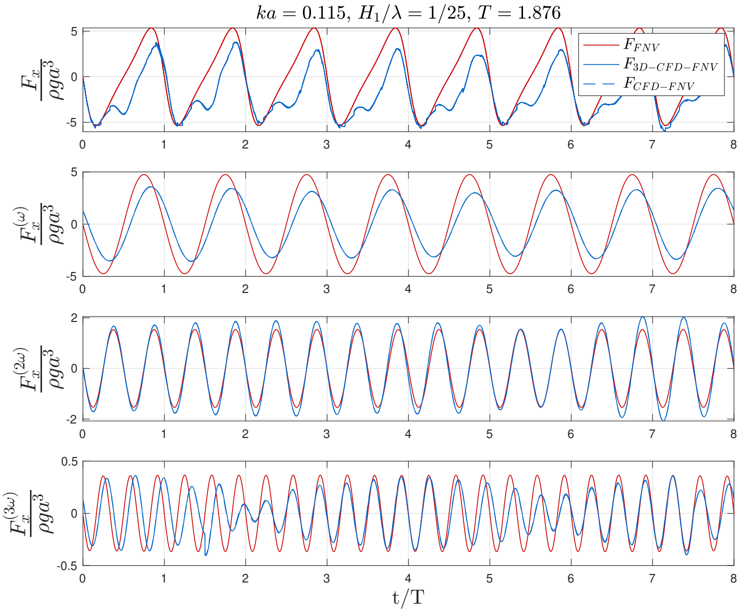

$ka = 0.115,\ H_1/\lambda = 1/25,\ T = 1.876$

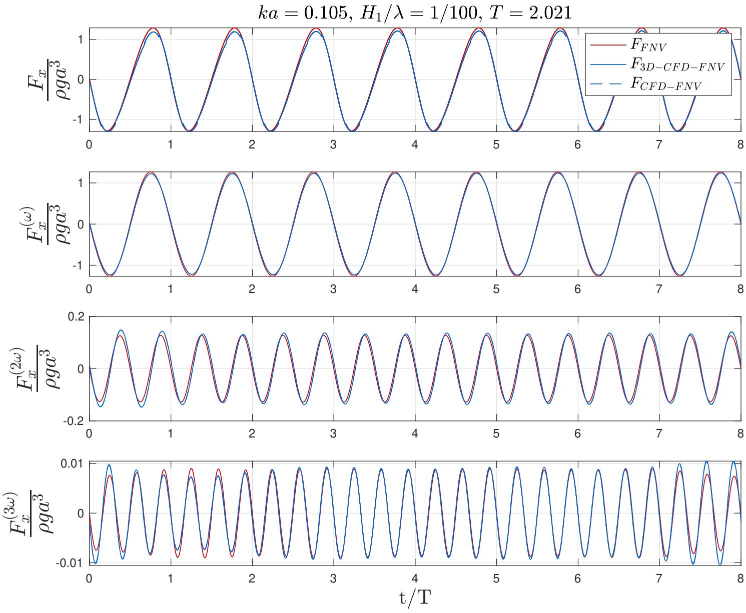

$ka = 0.105,\ H_1/\lambda = 1/100,\ T = 2.021$

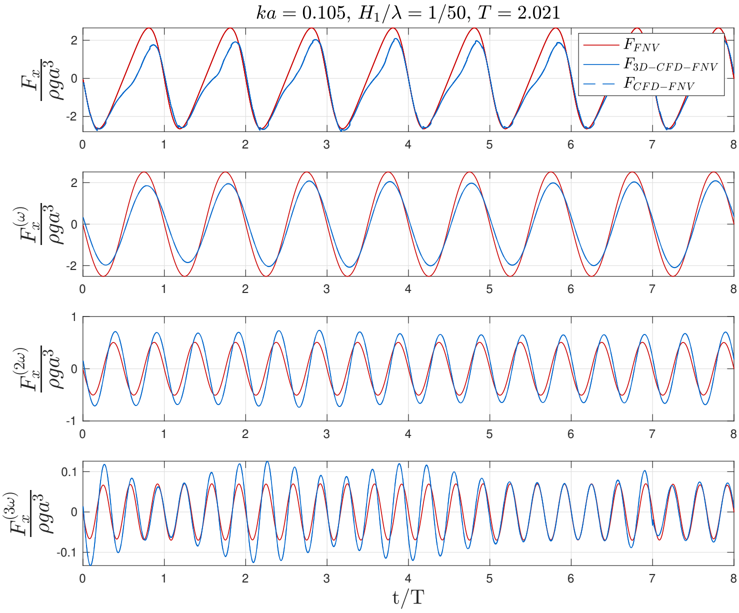
$ka = 0.105,\ H_1/\lambda = 1/50,\ T = 2.021$
F_{FNV}
$F_{3D-CFD-FNV}$
$F_{CFD-FNV}$
$\frac{F_x}{\rho g a^3}$
$\frac{F_x^{(\omega)}}{\rho g a^3}$
$\frac{F_x^{(2\omega)}}{\rho g a^3}$
$\frac{F_x^{(3\omega)}}{\rho g a^3}$
2
0
-2
1
0
-1
0.1
0
-0.1
0
1
2
3
4
5
6
7
8
t/T

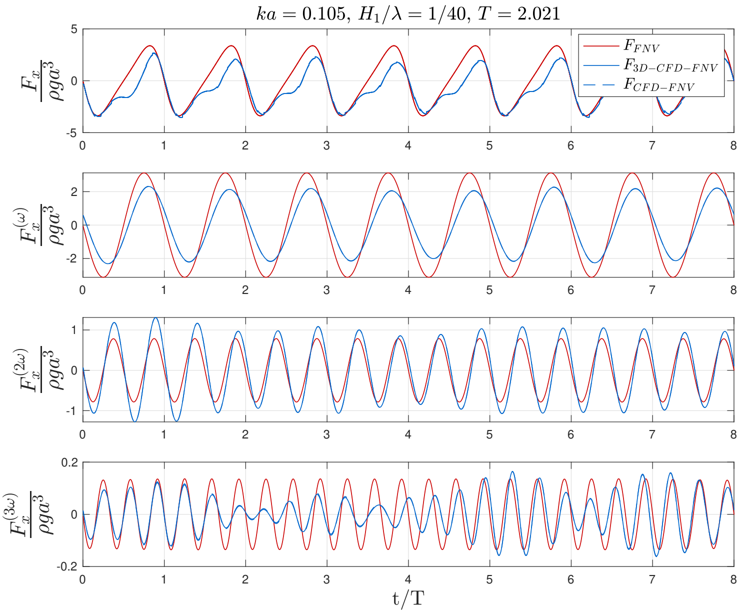
$ka = 0.105,\ H_1/\lambda = 1/40,\ T = 2.021$
F_{FNV}
$F_{3D-CFD-FNV}$
$F_{CFD-FNV}$
$\frac{F_x}{\rho g a^3}$
$\frac{F_x^{(\omega)}}{\rho g a^3}$
$\frac{F_x^{(2\omega)}}{\rho g a^3}$
$\frac{F_x^{(3\omega)}}{\rho g a^3}$
5
0
-5
2
0
-2
1
0
-1
0.2
0
-0.2
0
1
2
3
4
5
6
7
8
t/T

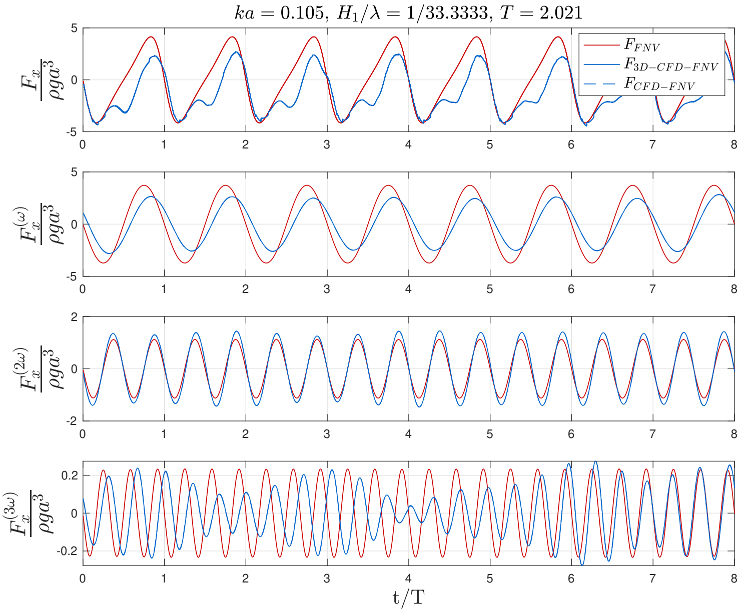
$ka = 0.105,\ H_1/\lambda = 1/33.3333,\ T = 2.021$
$\frac{F_x}{\rho g a^3}$
$\frac{F_x^{(\omega)}}{\rho g a^3}$
$\frac{F_x^{(2\omega)}}{\rho g a^3}$
$\frac{F_x^{(3\omega)}}{\rho g a^3}$
F_{FNV}
$F_{3D-CFD-FNV}$
$F_{CFD-FNV}$
5
0
-5
2
-2
0.2
-0.2
0
1
2
3
4
5
6
7
8
t/T

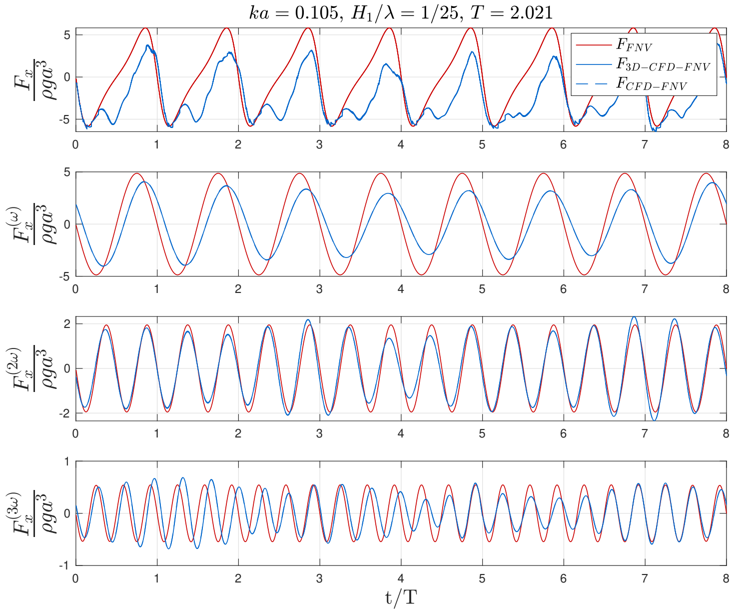
$ka = 0.105,\ H_1/\lambda = 1/25,\ T = 2.021$
$\frac{F_x}{\rho g a^3}$
$\frac{F_x^{(\omega)}}{\rho g a^3}$
$\frac{F_x^{(2\omega)}}{\rho g a^3}$
$\frac{F_x^{(3\omega)}}{\rho g a^3}$
F_{FNV}
$F_{3D-CFD-FNV}$
$F_{CFD-FNV}$
5
0
-5
2
-2
1
-1
0
1
2
3
4
5
6
7
8
t/T

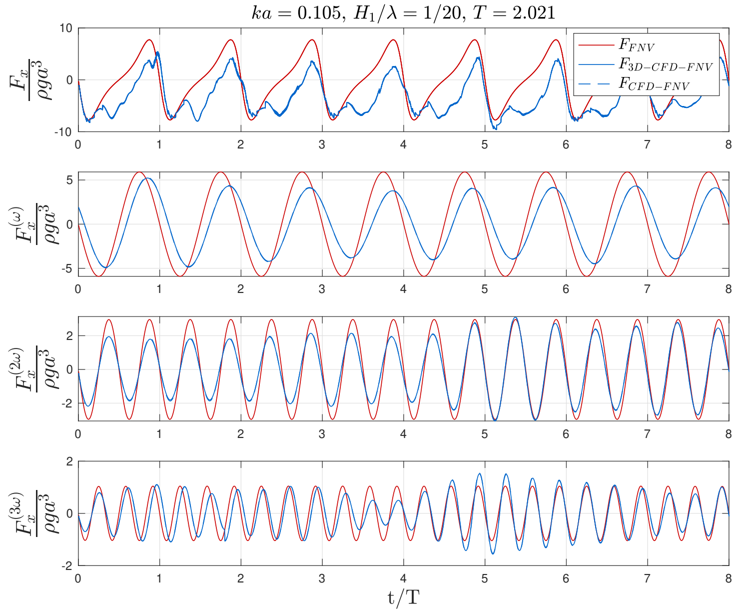
$ka = 0.105,\ H_1/\lambda = 1/20,\ T = 2.021$
$\frac{F_x}{\rho g a^3}$
$\frac{F_x^{(\omega)}}{\rho g a^3}$
$\frac{F_x^{(2\omega)}}{\rho g a^3}$
$\frac{F_x^{(3\omega)}}{\rho g a^3}$
F_{FNV}
$F_{3D-CFD-FNV}$
$F_{CFD-FNV}$
10
0
-10
5
-5
2
-2
0 1 2 3 4 5 6 7 8
t/T

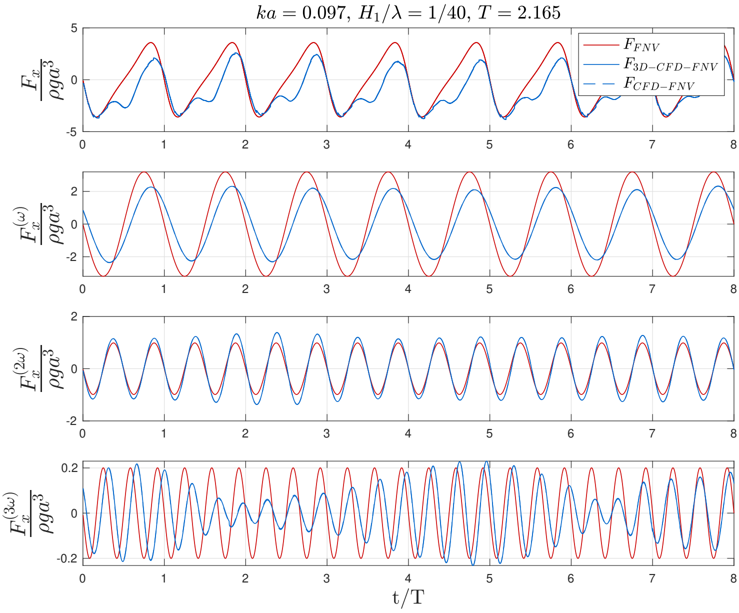
$ka = 0.097,\ H_1/\lambda = 1/40,\ T = 2.165$
$\frac{F_x}{\rho g a^3}$
$\frac{F_x^{(\omega)}}{\rho g a^3}$
$\frac{F_x^{(2\omega)}}{\rho g a^3}$
$\frac{F_x^{(3\omega)}}{\rho g a^3}$
F_{FNV}
$F_{3D-CFD-FNV}$
$F_{CFD-FNV}$
5
0
-5
2
-2
0.2
-0.2
0 1 2 3 4 5 6 7 8
t/T

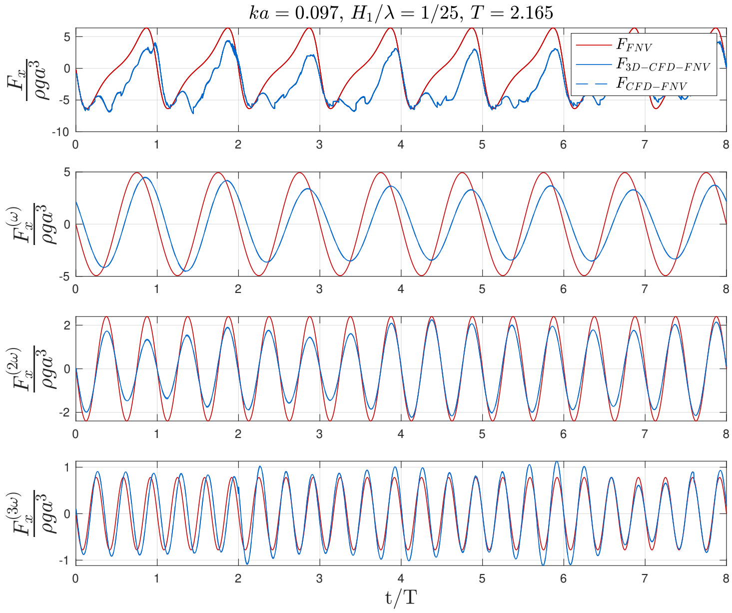
$ka = 0.097,\ H_1/\lambda = 1/25,\ T = 2.165$
$\frac{F_x}{\rho g a^3}$
$\frac{F_x^{(\omega)}}{\rho g a^3}$
$\frac{F_x^{(2\omega)}}{\rho g a^3}$
$\frac{F_x^{(3\omega)}}{\rho g a^3}$
F_{FNV}
$F_{3D-CFD-FNV}$
$F_{CFD-FNV}$
5
0
-5
-10
2
-2
1
-1
0 1 2 3 4 5 6 7 8
t/T

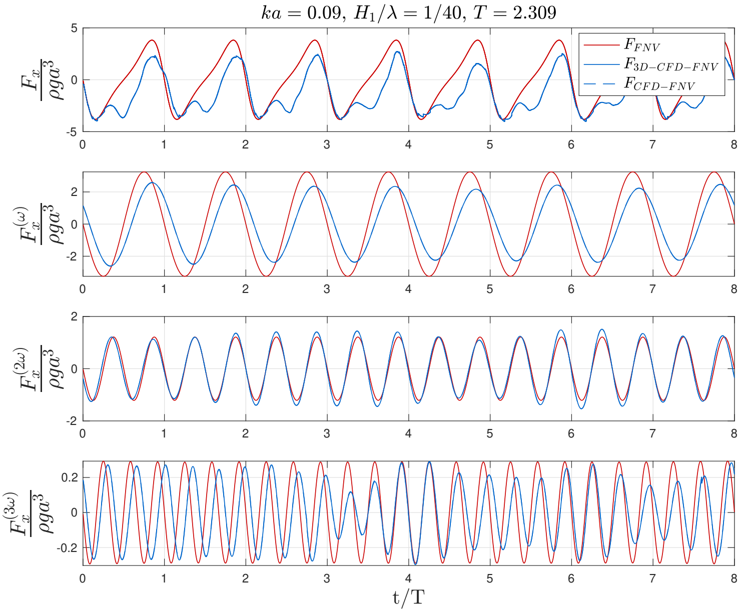
$ka = 0.09,\ H_1/\lambda = 1/40,\ T = 2.309$
$\frac{F_x}{\rho g a^3}$
$\frac{F_x^{(\omega)}}{\rho g a^3}$
$\frac{F_x^{(2\omega)}}{\rho g a^3}$
$\frac{F_x^{(3\omega)}}{\rho g a^3}$
F_{FNV}
$F_{3D-CFD-FNV}$
$F_{CFD-FNV}$
5
0
-5
2
-2
0.2
-0.2
0 1 2 3 4 5 6 7 8
t/T

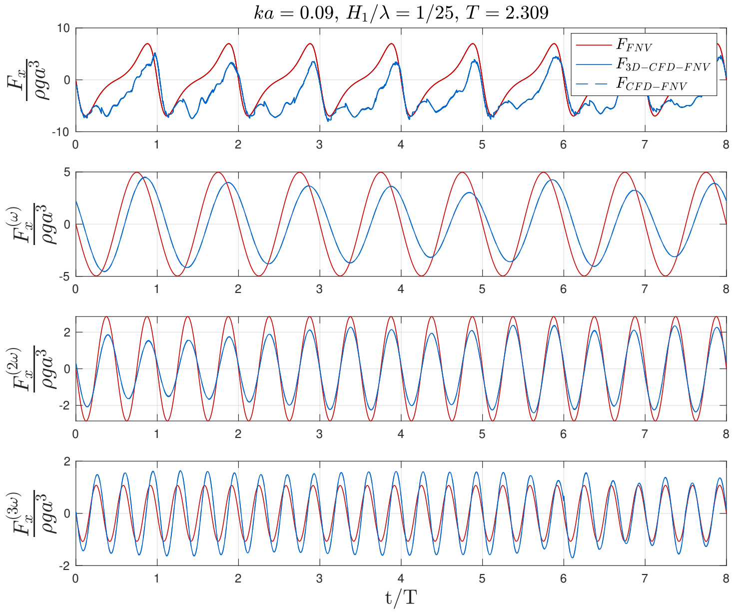
$ka = 0.09,\ H_1/\lambda = 1/25,\ T = 2.309$
$\frac{F_x}{\rho g a^3}$
F_{FNV}
$F_{3D-CFD-FNV}$
$F_{CFD-FNV}$
$\frac{F_x^{(\omega)}}{\rho g a^3}$
$\frac{F_x^{(2\omega)}}{\rho g a^3}$
$\frac{F_x^{(3\omega)}}{\rho g a^3}$
10
0
-10
5
-5
2
-2
0
1
2
3
4
5
6
7
8
t/T

A.2 Time series of the total and first three harmonics of the force components from 3D CFD-FNV load model

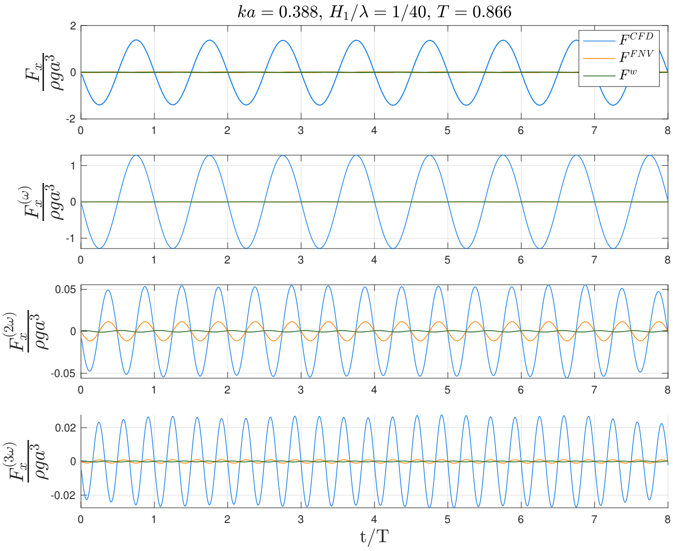

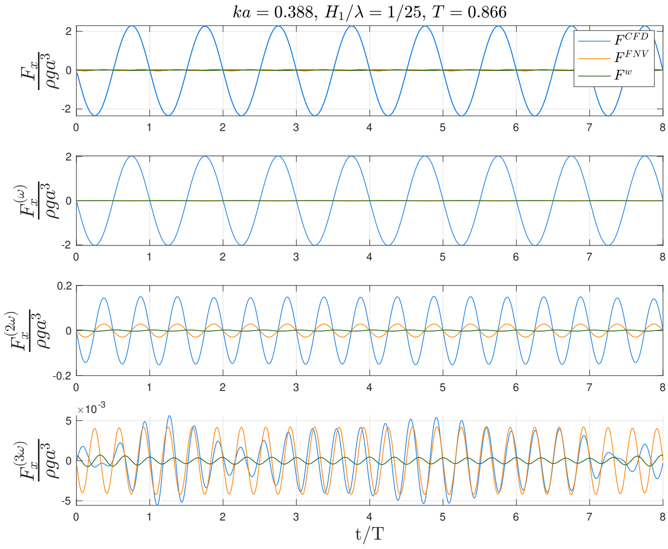

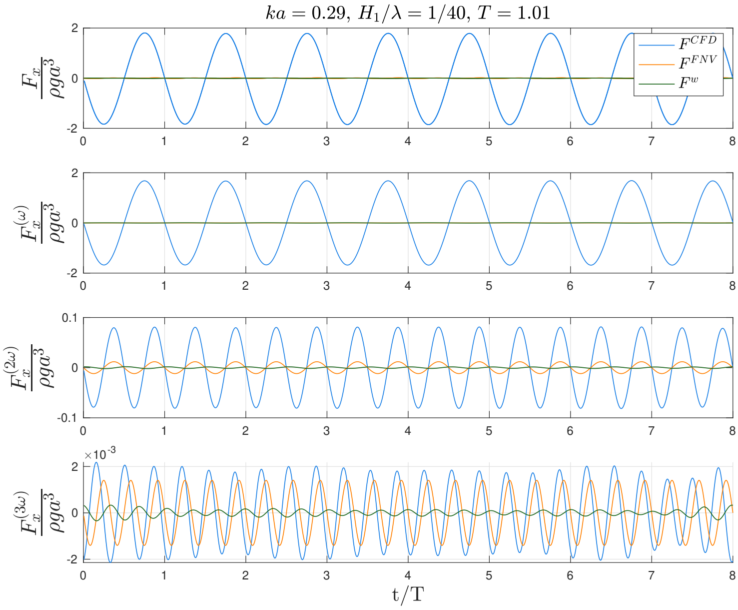
$ka = 0.29,\ H_1/\lambda = 1/40,\ T = 1.01$

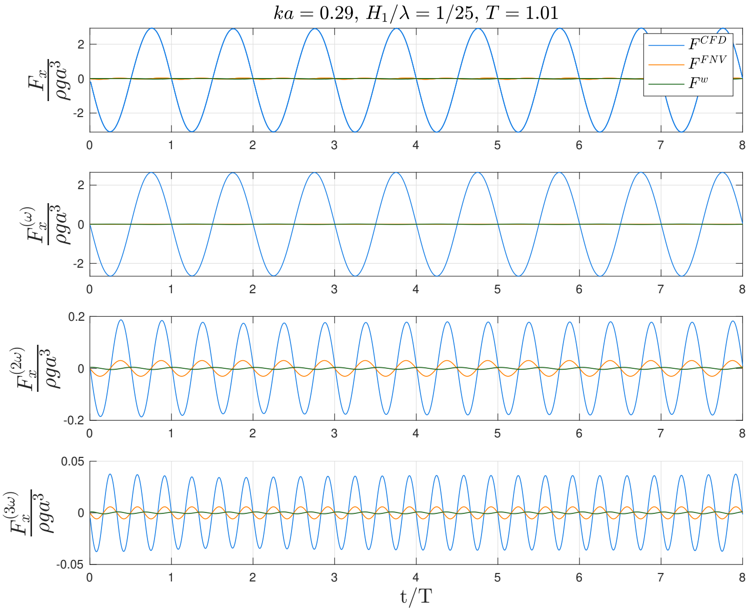
$ka = 0.29,\ H_1/\lambda = 1/25,\ T = 1.01$

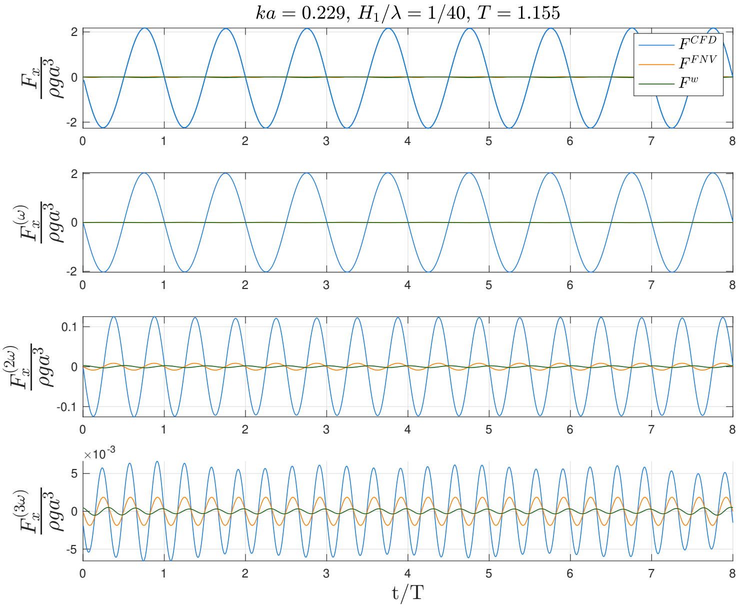
$ka = 0.229,\ H_1/\lambda = 1/40,\ T = 1.155$
$\frac{F_x}{\rho g a^3}$
$\frac{F_x^{(\omega)}}{\rho g a^3}$
$\frac{F_x^{(2\omega)}}{\rho g a^3}$
$\frac{F_x^{(3\omega)}}{\rho g a^3}$
$\times 10^{-3}$
F^{CFD}
F^{FNV}
F^{w}
t/T
0
1
2
3
4
5
6
7
8
2
0
-2
0.1
-0.1
5
-5

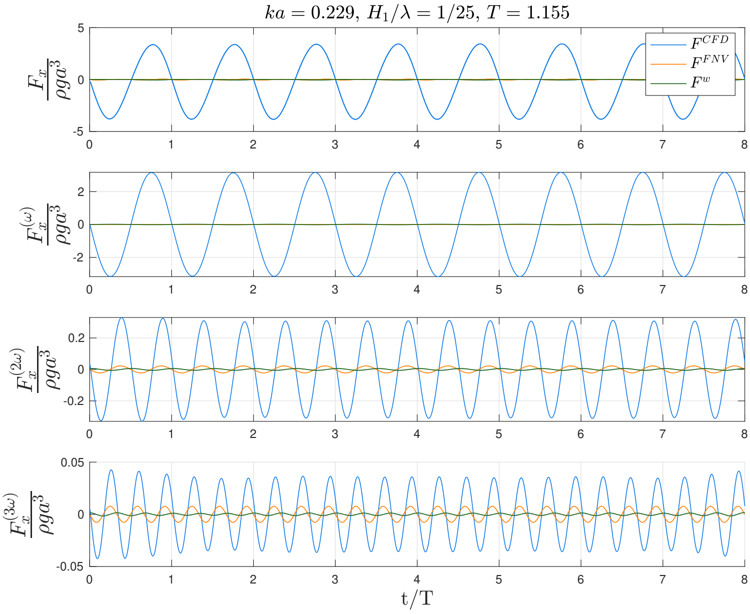
$ka = 0.229,\ H_1/\lambda = 1/25,\ T = 1.155$
$\frac{F_x}{\rho g a^3}$
$\frac{F_x^{(\omega)}}{\rho g a^3}$
$\frac{F_x^{(2\omega)}}{\rho g a^3}$
$\frac{F_x^{(3\omega)}}{\rho g a^3}$
F^{CFD}
F^{FNV}
F^{w}
t/T
0
1
2
3
4
5
6
7
8
5
-5
2
-2
0.2
-0.2
0.05
-0.05

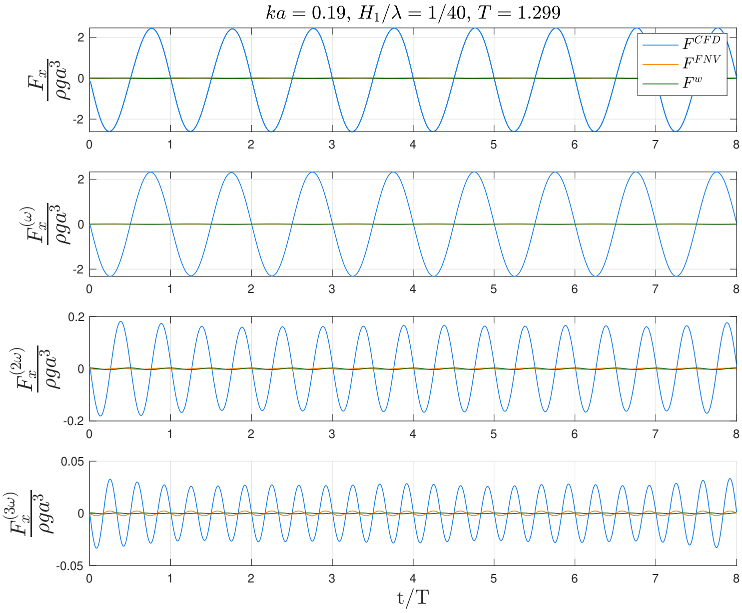

$ka = 0.19,\ H_1/\lambda = 1/40,\ T = 1.299$

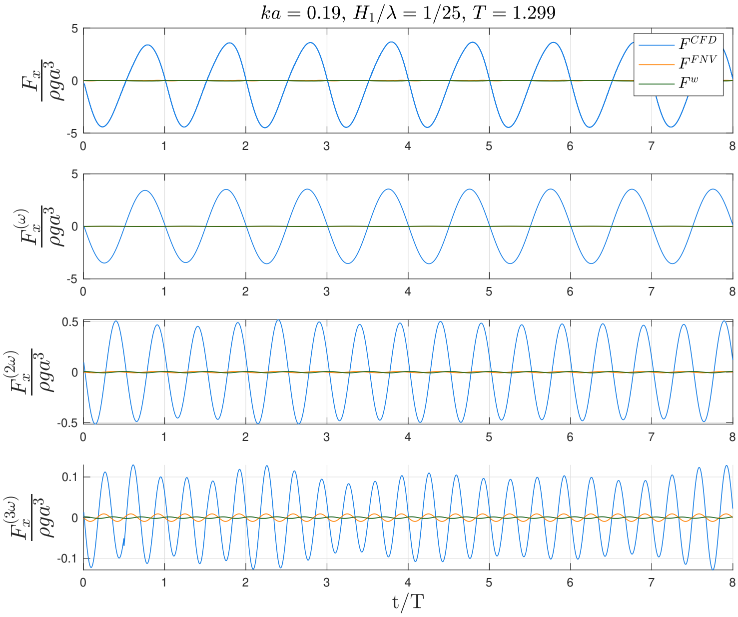

$ka = 0.19,\ H_1/\lambda = 1/25,\ T = 1.299$

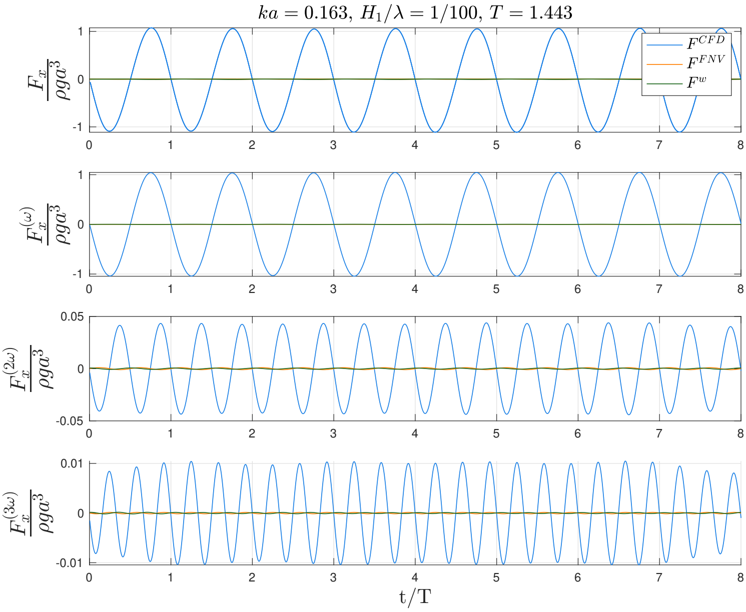
$ka = 0.163,\ H_1/\lambda = 1/100,\ T = 1.443$
$\frac{F_x}{\rho g a^3}$
$\frac{F_x^{(\omega)}}{\rho g a^3}$
$\frac{F_x^{(2\omega)}}{\rho g a^3}$
$\frac{F_x^{(3\omega)}}{\rho g a^3}$
F^{CFD}
F^{FNV}
F^{w}
1
0
-1
0.05
-0.05
0.01
-0.01
0
1
2
3
4
5
6
7
8
t/T

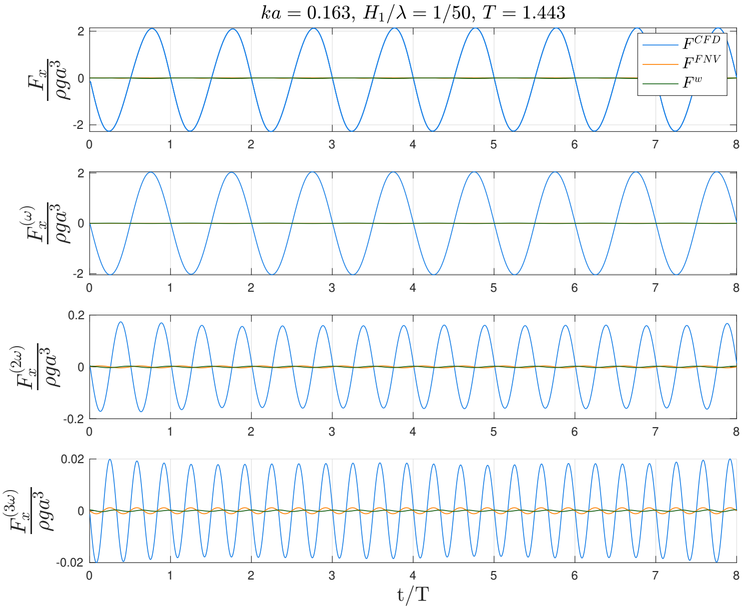
$ka = 0.163,\ H_1/\lambda = 1/50,\ T = 1.443$
$\frac{F_x}{\rho g a^3}$
$\frac{F_x^{(\omega)}}{\rho g a^3}$
$\frac{F_x^{(2\omega)}}{\rho g a^3}$
$\frac{F_x^{(3\omega)}}{\rho g a^3}$
F^{CFD}
F^{FNV}
F^{w}
2
0
-2
0.2
-0.2
0.02
-0.02
0
1
2
3
4
5
6
7
8
t/T

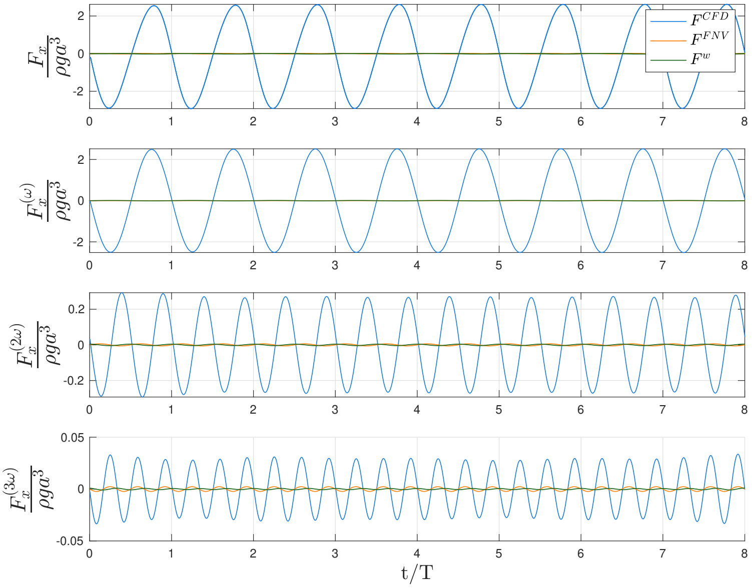

$ka = 0.163,\ H_1/\lambda = 1/40,\ T = 1.443$

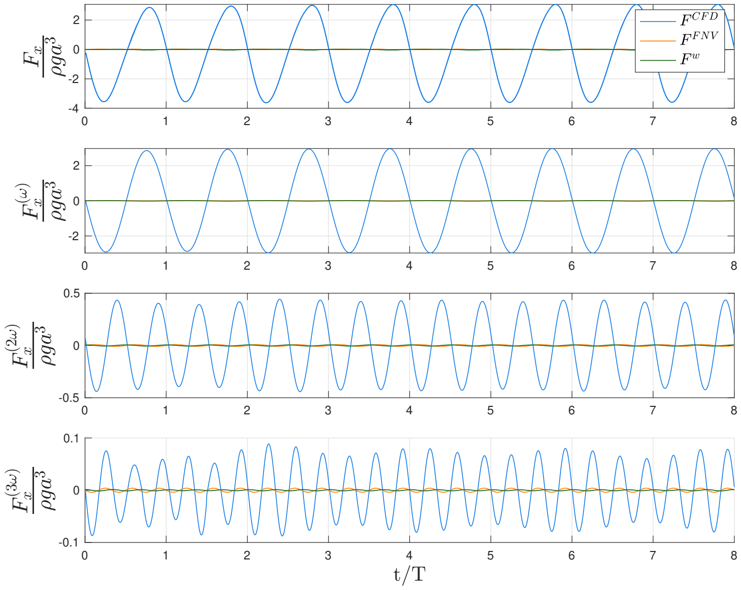

$ka = 0.163,\ H_1/\lambda = 1/33.3333,\ T = 1.443$

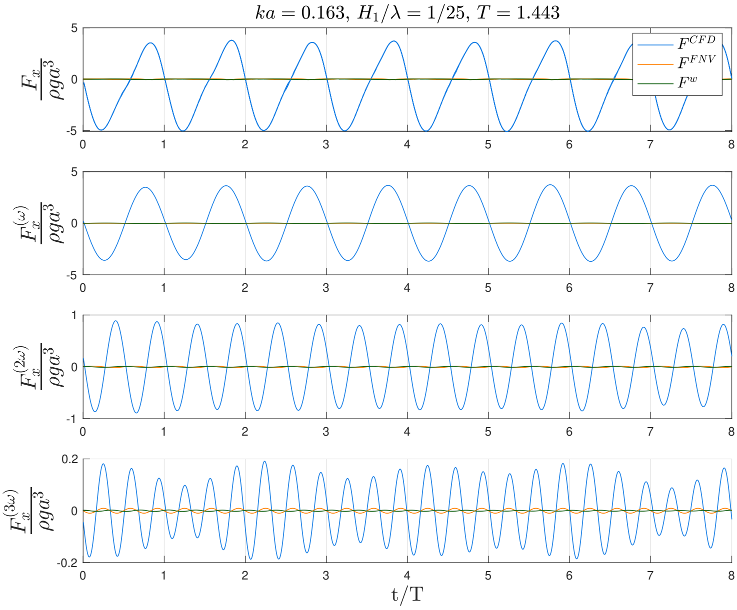

$ka = 0.163,\ H_1/\lambda = 1/25,\ T = 1.443$

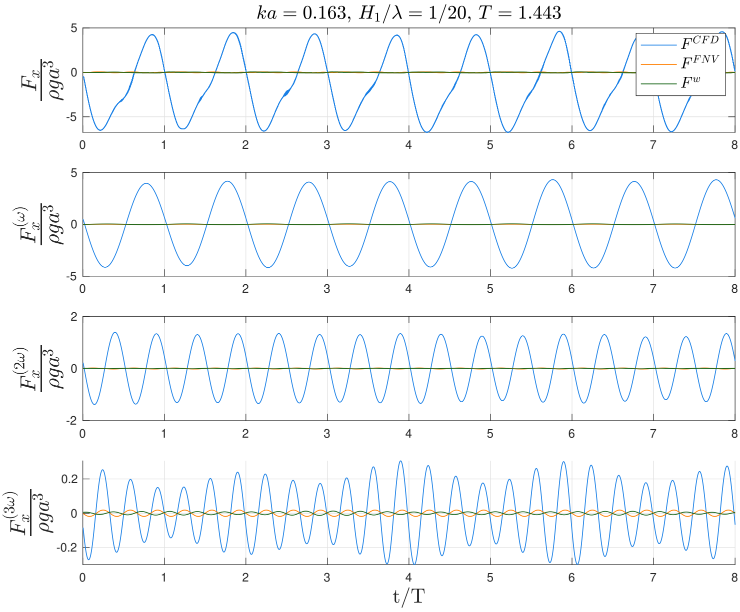

$ka = 0.163,\ H_1/\lambda = 1/20,\ T = 1.443$

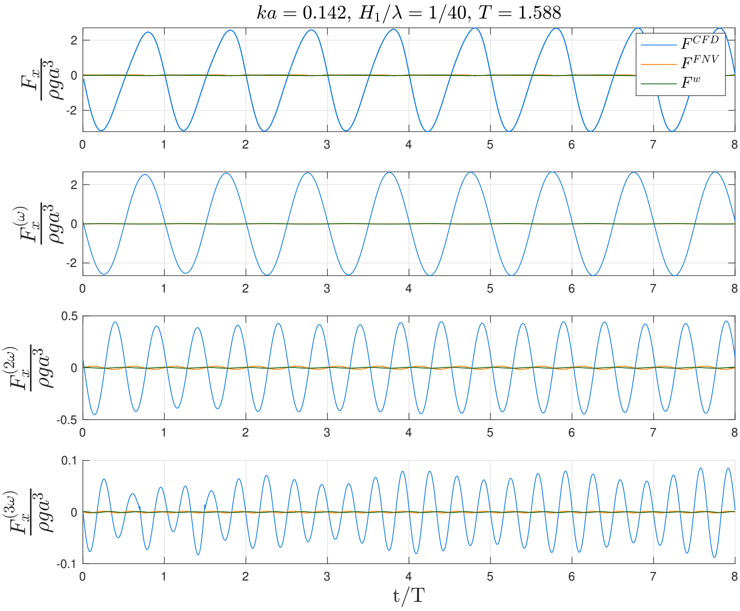
$ka = 0.142,\ H_1/\lambda = 1/40,\ T = 1.588$

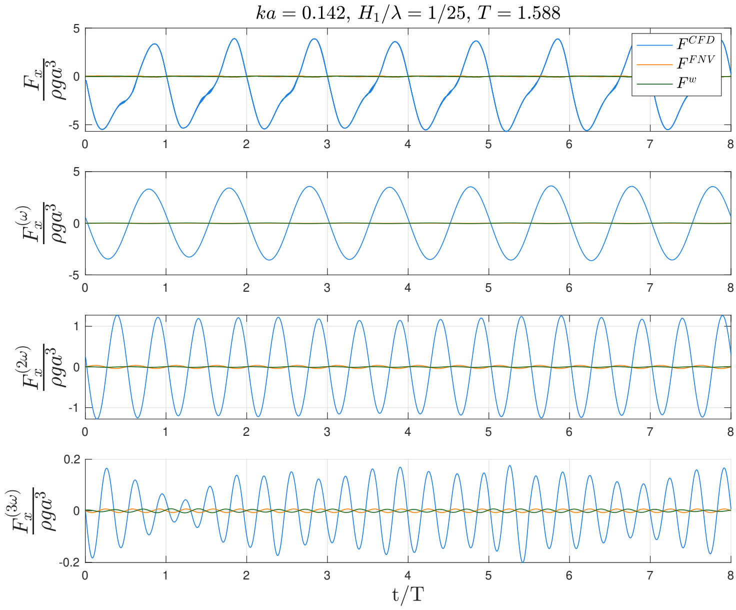
$ka = 0.142,\ H_1/\lambda = 1/25,\ T = 1.588$

$ka = 0.127,\ H_1/\lambda = 1/100,\ T = 1.732$

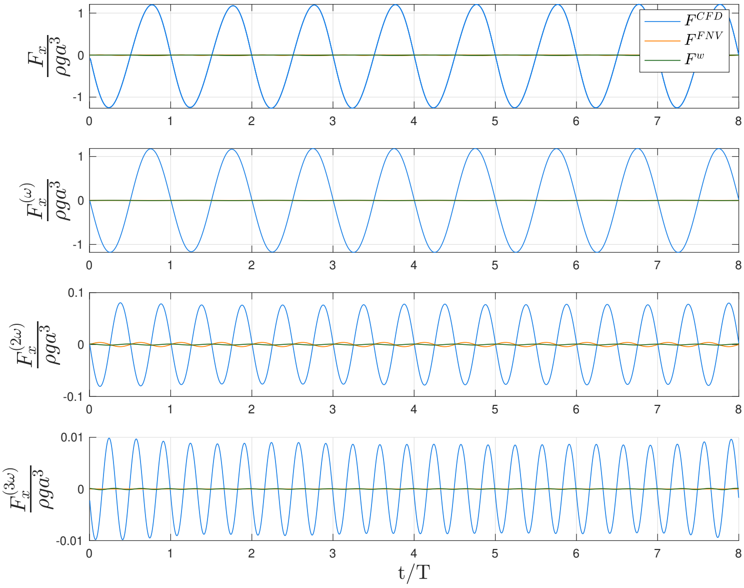

$ka = 0.127,\ H_1/\lambda = 1/50,\ T = 1.732$

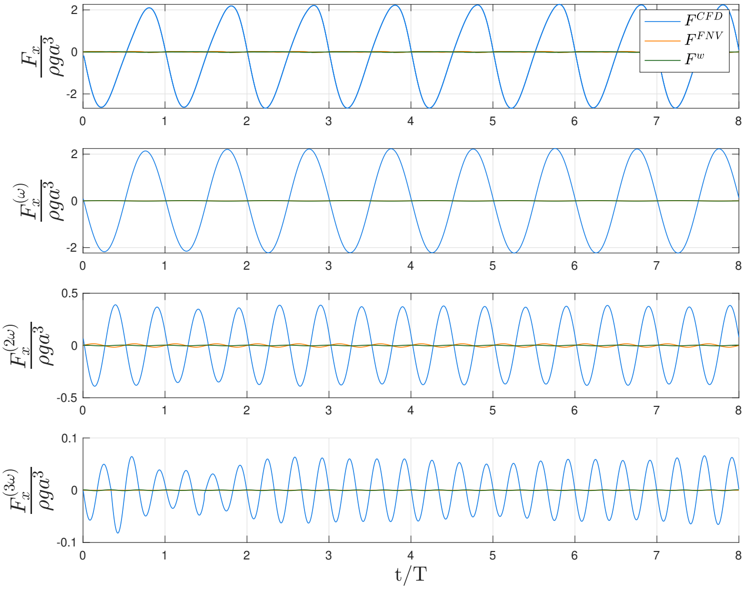

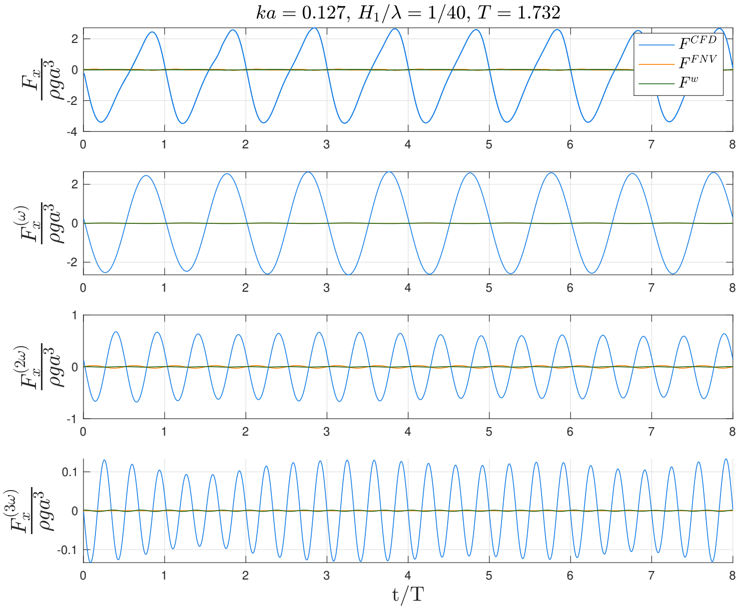

$ka = 0.127,\ H_1/\lambda = 1/40,\ T = 1.732$

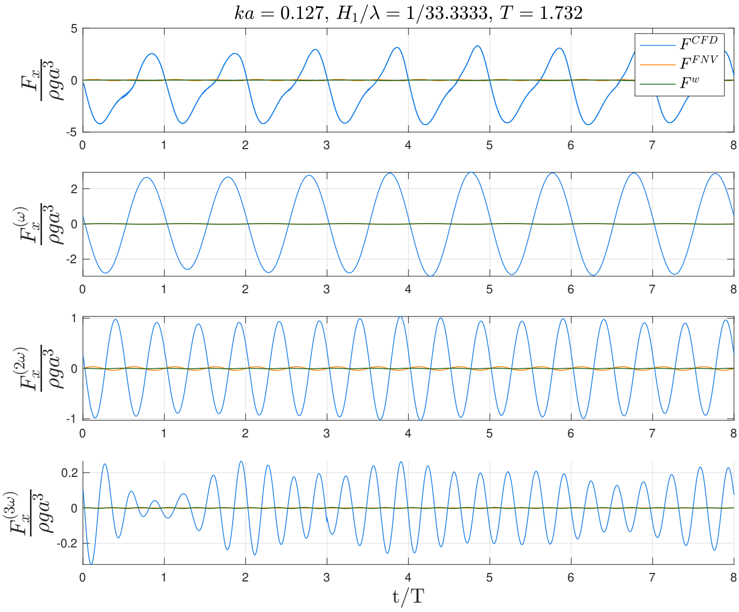

$ka = 0.127,\ H_1/\lambda = 1/33.3333,\ T = 1.732$

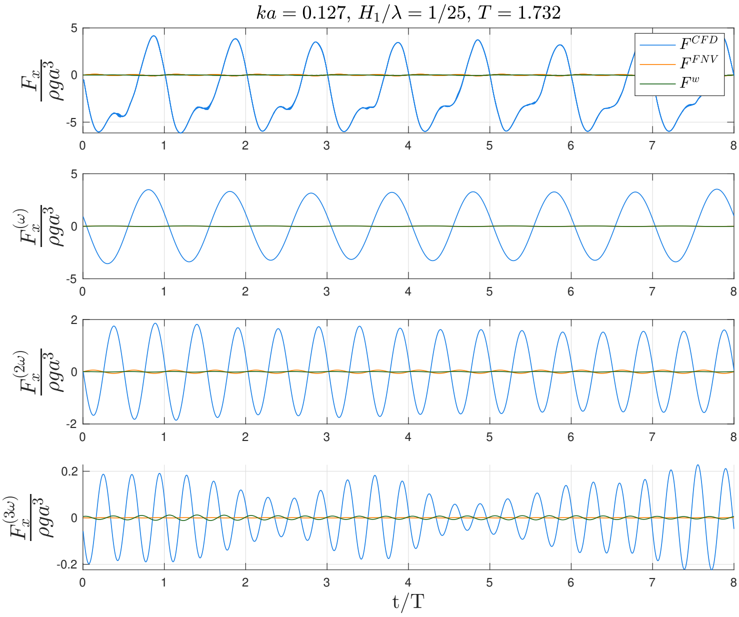
$ka = 0.127,\ H_1/\lambda = 1/25,\ T = 1.732$
$\frac{F_x}{\rho g a^3}$
$\frac{F_x^{(\omega)}}{\rho g a^3}$
$\frac{F_x^{(2\omega)}}{\rho g a^3}$
$\frac{F_x^{(3\omega)}}{\rho g a^3}$
F^{CFD}
F^{FNV}
F^{w}
5
0
-5
-2
2
0.2
-0.2
0
1
2
3
4
5
6
7
8
t/T

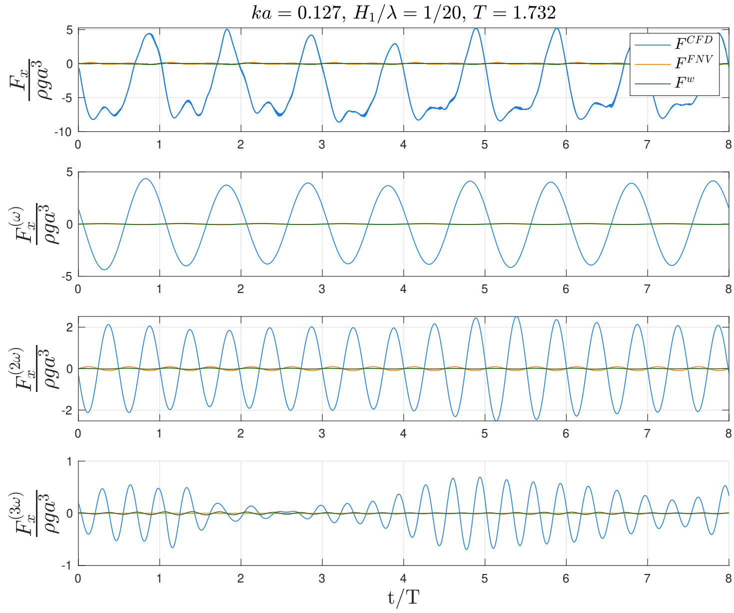
$ka = 0.127,\ H_1/\lambda = 1/20,\ T = 1.732$
$\frac{F_x}{\rho g a^3}$
$\frac{F_x^{(\omega)}}{\rho g a^3}$
$\frac{F_x^{(2\omega)}}{\rho g a^3}$
$\frac{F_x^{(3\omega)}}{\rho g a^3}$
F^{CFD}
F^{FNV}
F^{w}
5
0
-5
-10
2
-2
1
-1
0
1
2
3
4
5
6
7
8
t/T

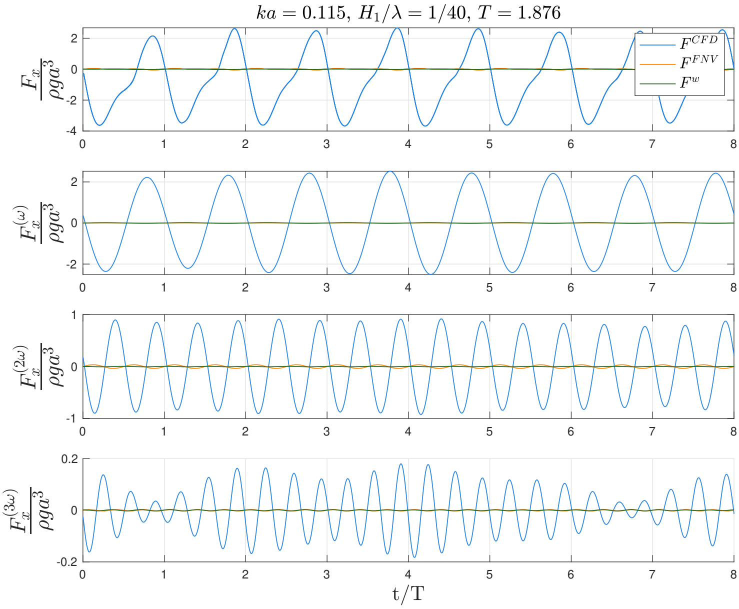
$ka = 0.115,\ H_1/\lambda = 1/40,\ T = 1.876$
$\frac{F_x}{\rho g a^3}$
$\frac{F_x^{(\omega)}}{\rho g a^3}$
$\frac{F_x^{(2\omega)}}{\rho g a^3}$
$\frac{F_x^{(3\omega)}}{\rho g a^3}$
F^{CFD}
F^{FNV}
F^{w}
2
0
-2
-4
1
-1
0.2
-0.2
0 1 2 3 4 5 6 7 8
t/T

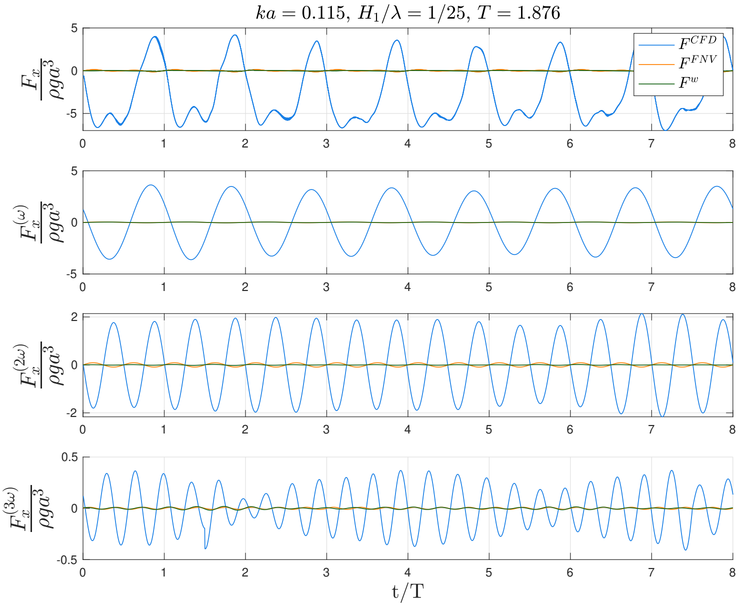
$ka = 0.115,\ H_1/\lambda = 1/25,\ T = 1.876$
$\frac{F_x}{\rho g a^3}$
$\frac{F_x^{(\omega)}}{\rho g a^3}$
$\frac{F_x^{(2\omega)}}{\rho g a^3}$
$\frac{F_x^{(3\omega)}}{\rho g a^3}$
F^{CFD}
F^{FNV}
F^{w}
5
0
-5
2
-2
0.5
-0.5
0 1 2 3 4 5 6 7 8
t/T

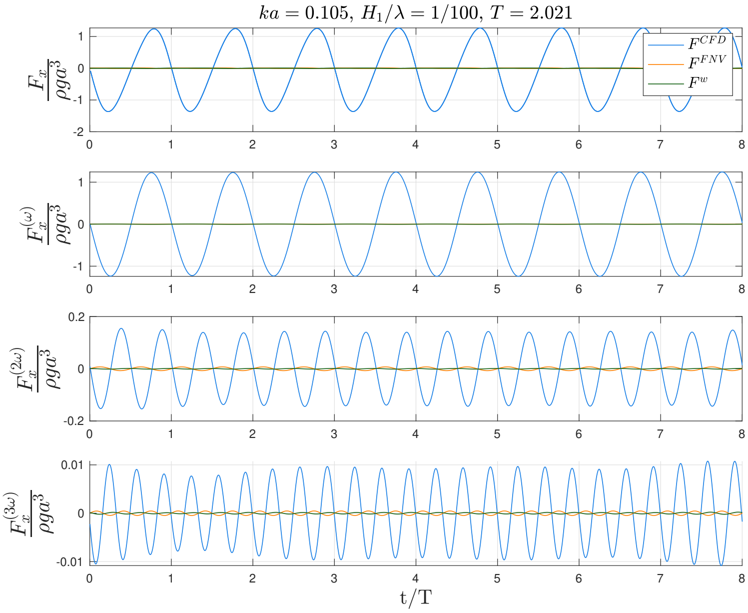

$ka = 0.105,\ H_1/\lambda = 1/100,\ T = 2.021$

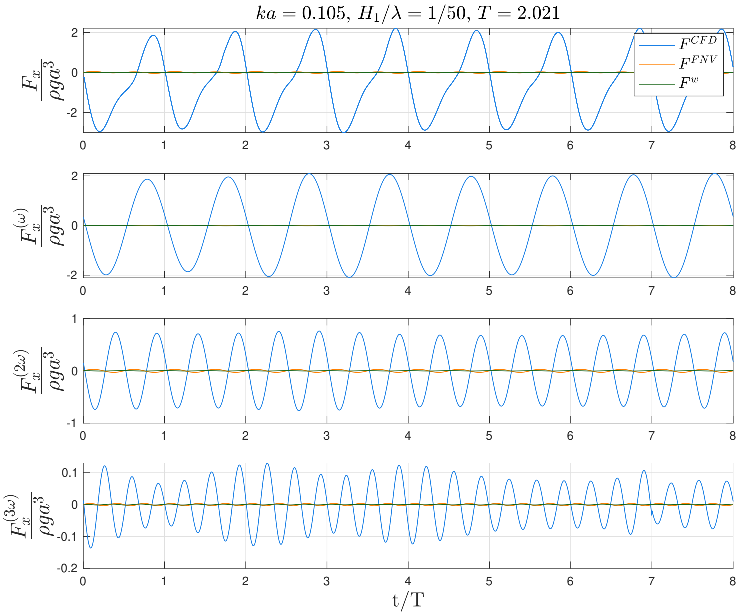

$ka = 0.105,\ H_1/\lambda = 1/50,\ T = 2.021$

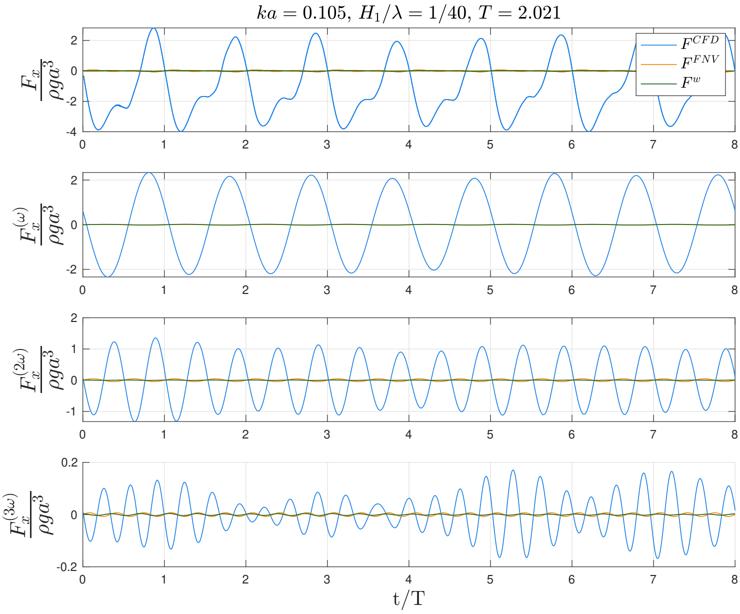
$ka = 0.105,\ H_1/\lambda = 1/40,\ T = 2.021$
F^{CFD}
F^{FNV}
F^{w}
$\frac{F_x}{\rho g a^3}$
$\frac{F_x^{(\omega)}}{\rho g a^3}$
$\frac{F_x^{(2\omega)}}{\rho g a^3}$
$\frac{F_x^{(3\omega)}}{\rho g a^3}$
2
0
-2
-4
1
-1
0.2
-0.2
0
1
2
3
4
5
6
7
8
t/T

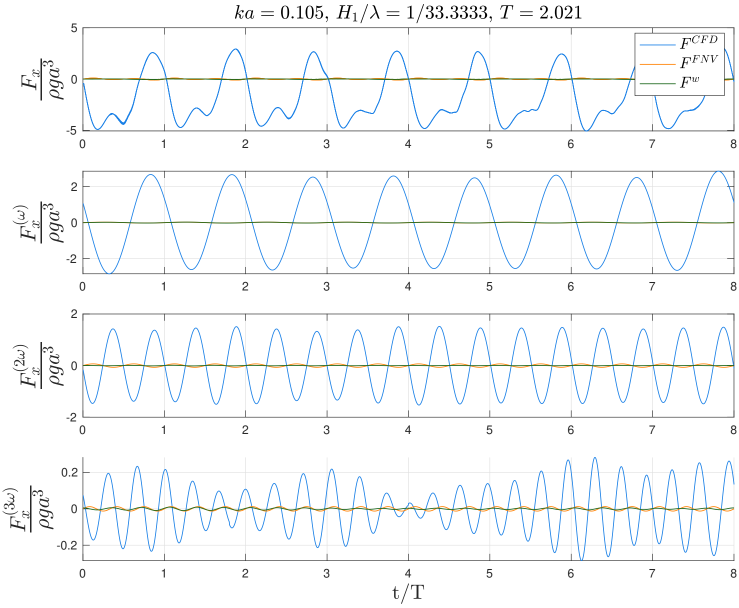
$ka = 0.105,\ H_1/\lambda = 1/33.3333,\ T = 2.021$
F^{CFD}
F^{FNV}
F^{w}
$\frac{F_x}{\rho g a^3}$
$\frac{F_x^{(\omega)}}{\rho g a^3}$
$\frac{F_x^{(2\omega)}}{\rho g a^3}$
$\frac{F_x^{(3\omega)}}{\rho g a^3}$
5
0
-5
2
-2
0.2
-0.2
0
1
2
3
4
5
6
7
8
t/T

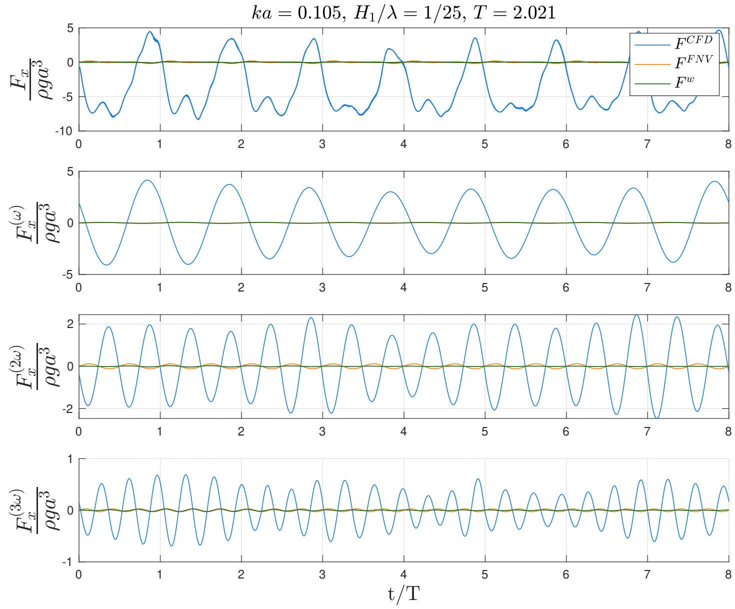

$ka = 0.105,\ H_1/\lambda = 1/25,\ T = 2.021$
$\frac{F_x}{\rho g a^3}$
$\frac{F_x^{(\omega)}}{\rho g a^3}$
$\frac{F_x^{(2\omega)}}{\rho g a^3}$
$\frac{F_x^{(3\omega)}}{\rho g a^3}$
F^{CFD}
F^{FNV}
F^{w}
5
0
-5
-10
2
-2
1
-1
0 1 2 3 4 5 6 7 8
t/T

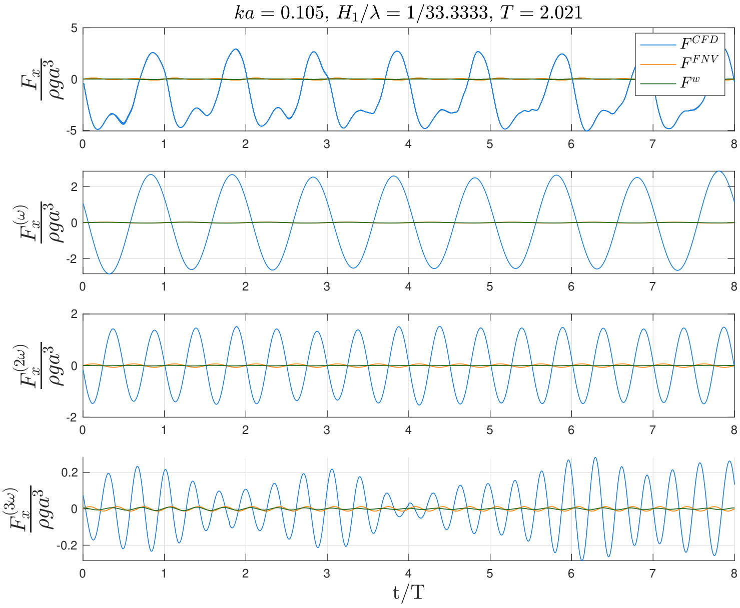

$ka = 0.105,\ H_1/\lambda = 1/33.3333,\ T = 2.021$
$\frac{F_x}{\rho g a^3}$
$\frac{F_x^{(\omega)}}{\rho g a^3}$
$\frac{F_x^{(2\omega)}}{\rho g a^3}$
$\frac{F_x^{(3\omega)}}{\rho g a^3}$
F^{CFD}
F^{FNV}
F^{w}
5
0
-5
2
-2
0.2
-0.2
0 1 2 3 4 5 6 7 8
t/T

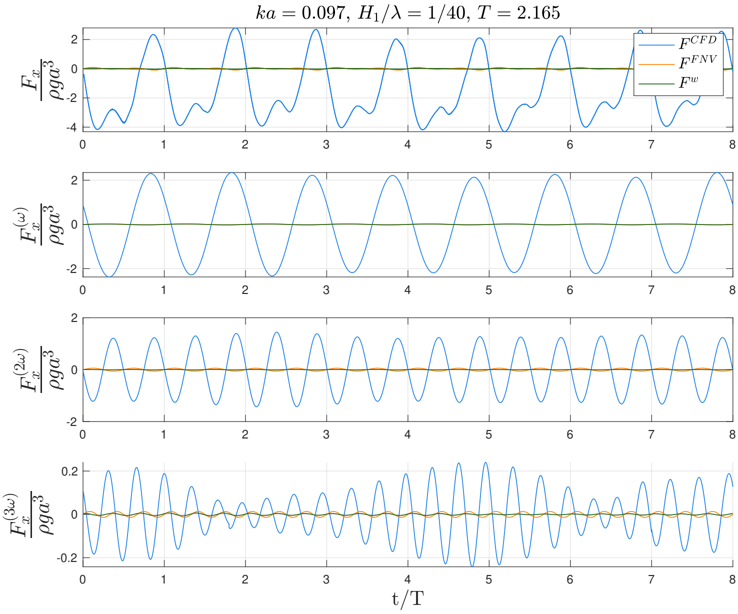

$ka = 0.097,\ H_1/\lambda = 1/40,\ T = 2.165$

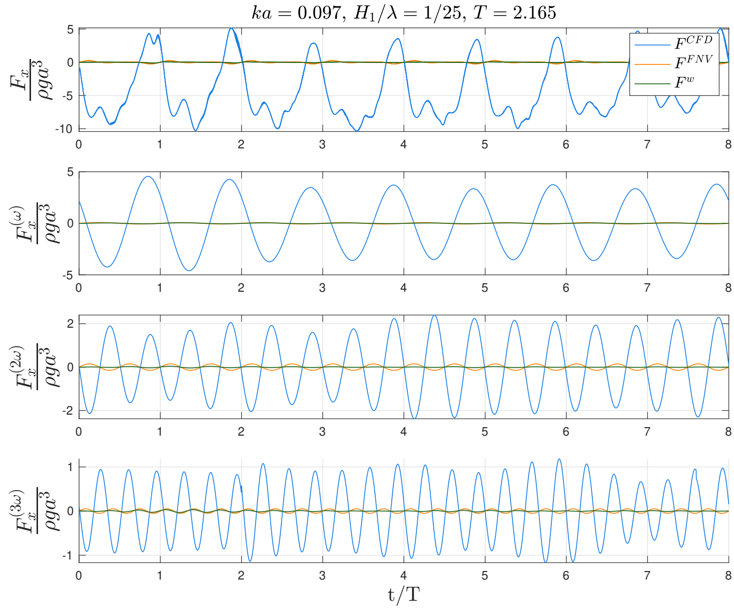

$ka = 0.097,\ H_1/\lambda = 1/25,\ T = 2.165$

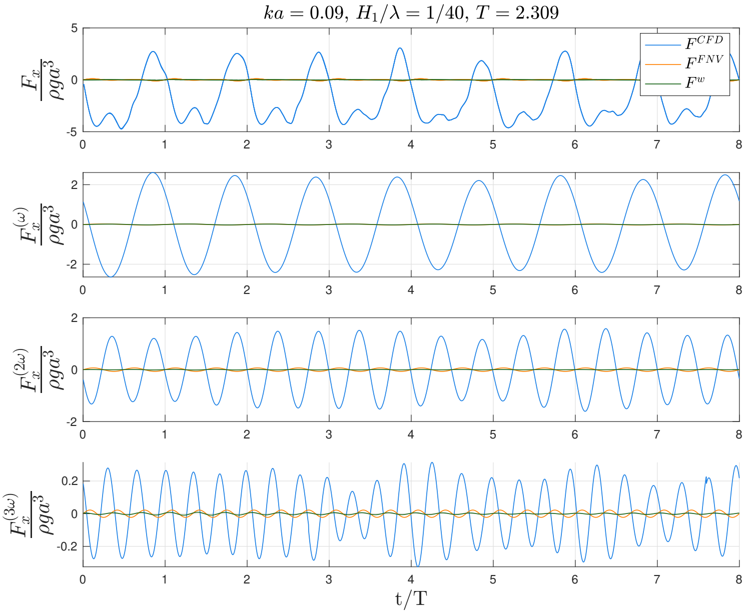
$ka = 0.09,\ H_1/\lambda = 1/40,\ T = 2.309$
$\frac{F_x}{\rho g a^3}$
$\frac{F_x^{(\omega)}}{\rho g a^3}$
$\frac{F_x^{(2\omega)}}{\rho g a^3}$
$\frac{F_x^{(3\omega)}}{\rho g a^3}$
F^{CFD}
F^{FNV}
F^{w}
5
0
-5
2
0
-2
2
0
-2
0.2
0
-0.2
0 1 2 3 4 5 6 7 8
t/T

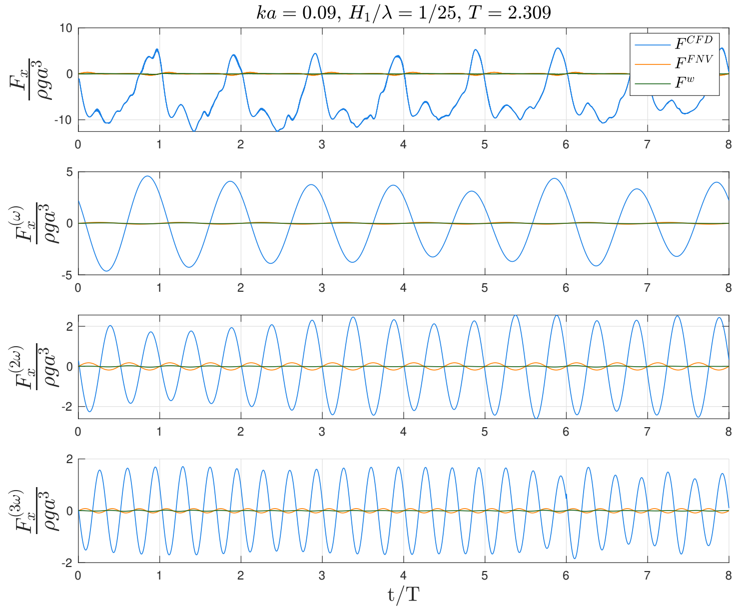
$ka = 0.09,\ H_1/\lambda = 1/25,\ T = 2.309$
$\frac{F_x}{\rho g a^3}$
$\frac{F_x^{(\omega)}}{\rho g a^3}$
$\frac{F_x^{(2\omega)}}{\rho g a^3}$
$\frac{F_x^{(3\omega)}}{\rho g a^3}$
F^{CFD}
F^{FNV}
F^{w}
10
0
-10
5
0
-5
2
0
-2
2
0
-2
0 1 2 3 4 5 6 7 8
t/T

Appendix B

B.1 Visualization of flow regimes around monopile

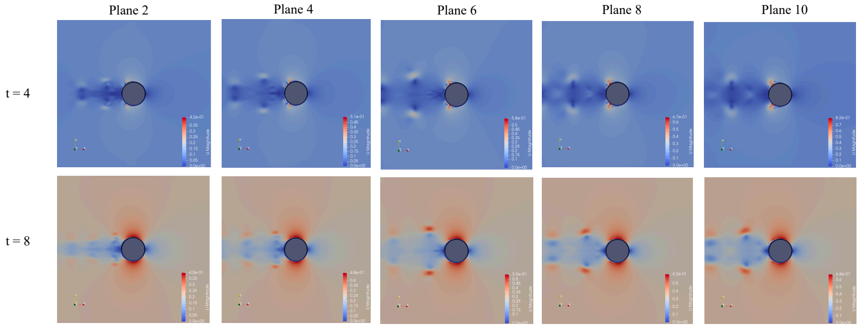

Figure B.1: Flow regime around monopile for $ka = 0.163$ and $H_1/\lambda = 1/40$.

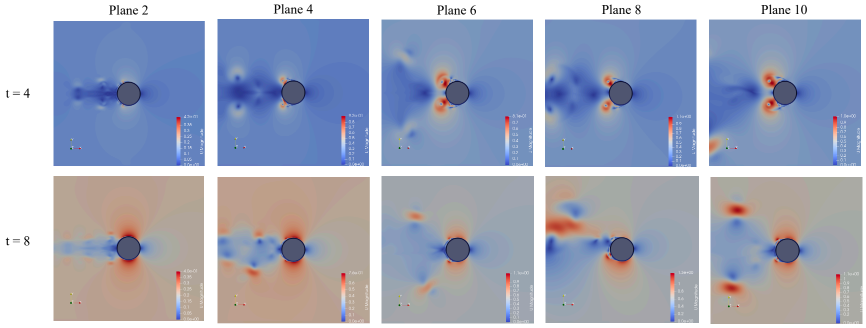

Figure B.2: Flow regime around monopile for $ka = 0.163$ and $H_1/\lambda = 1/25$.

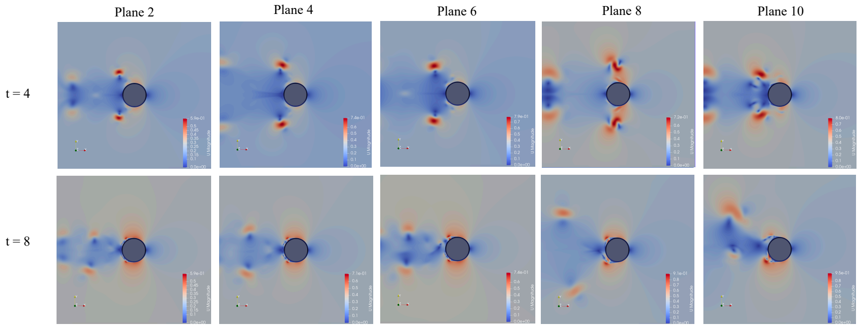

Figure B.3: Flow regime around monopile for $ka = 0.127$ and $H_1/\lambda = 1/40$.

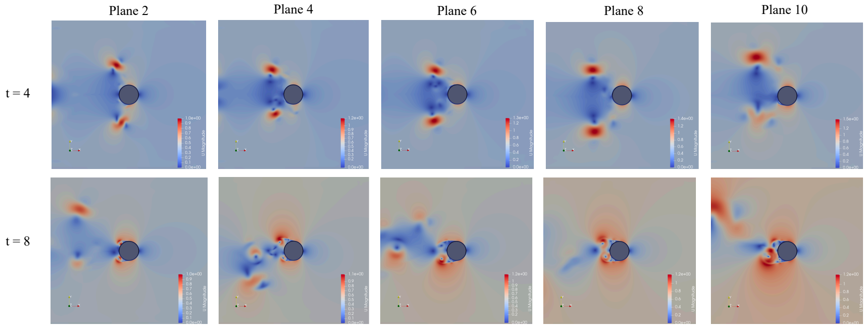

Figure B.4: Flow regime around monopile for $ka = 0.127$ and $H_1/\lambda = 1/25$.

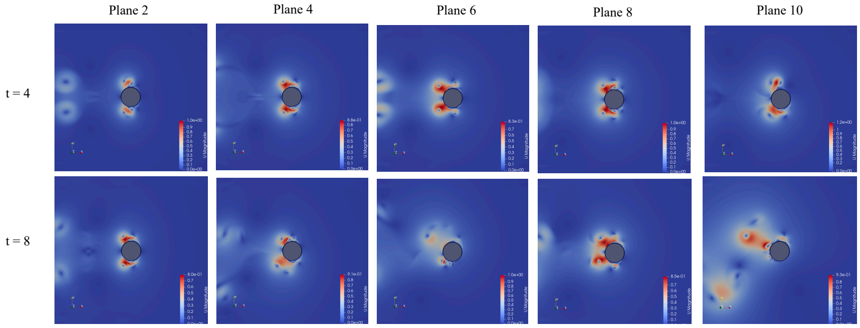

Figure B.5: Flow regime around monopile for $ka = 0.105$ and $H_1/\lambda = 1/40$.

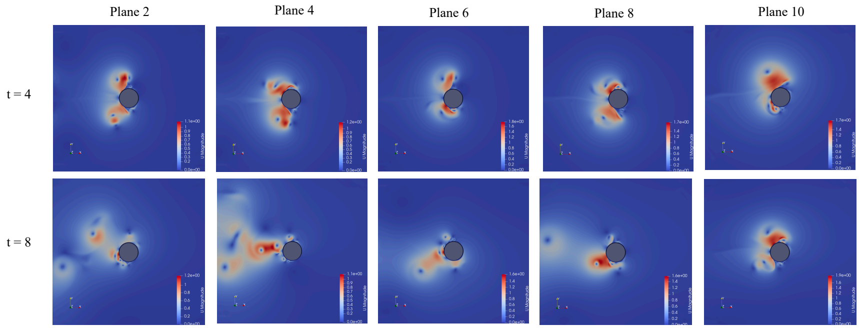

Figure B.6: Flow regime around monopile for $ka = 0.105$ and $H_1/\lambda = 1/25$.

NTNU

Kunnskap for en bedre verden